Automated Recognition of 3D CAD Model Objects in Dense Laser Range Point Clouds

by

Frédéric N. Bosché

A thesis
presented to the University of Waterloo
in fulfillment of the
thesis requirement for the degree of
Doctor of Philosophy
in
Civil Engineering

Waterloo, Ontario, Canada, 2008

I hereby declare that I am the sole author of this thesis. This is a true copy of the thesis, including any required final revisions, as accepted by my examiners.

I understand that my thesis may be made electronically available to the public.

Abstract

There is shift in the Architectural / Engineering / Construction and Facility Management (AEC&FM) industry toward performance-driven projects. Assuring good performance requires efficient and reliable performance control processes. However, the current state of the AEC&FM industry is that control processes are inefficient because they generally rely on manually intensive, inefficient, and often inaccurate data collection techniques.

Critical performance control processes include progress tracking and dimensional quality control. These particularly rely on the accurate and efficient collection of the as-built 3D status of project objects. However, currently available techniques for as-built 3D data collection are extremely inefficient, and provide partial and often inaccurate information. These limitations have a negative impact on the quality of decisions made by project managers and consequently on project success.

This thesis presents an innovative approach for Automated 3D Data Collection (A3dDC). This approach takes advantage of Laser Detection and Ranging (LADAR), 3D Computer-Aided-Design (CAD) modeling and registration technologies. The performance of this approach is investigated with a first set of experimental results obtained with real-life data. A second set of experiments then analyzes the feasibility of implementing, based on the developed approach, automated project performance control (APPC) applications such as automated project progress tracking and automated dimensional quality control. Finally, other applications are identified including planning for scanning and strategic scanning.

Acknowledgements

First of all, I would like to truly thank my supervisor, Dr. Carl T. Haas, for his dedicated supervision and mentoring, and honest friendship. I would also like to thank the members of my Ph.D. committee, as well as Dr. Vanheeghe who deserved to be part of it, for their help in my PhD research and thesis writing endeavors.

Then, I would like to thank all my family, starting with my parents, Nicole and Jean-Pierre, for their psychological and also financial support. All this would not have been possible without their support, that started almost thirty years ago. I thank my sister, Valérie, and brothers, Nicolas and Aurélien, for they have played a key role in the happy life that I have lived up to now. Also, I have had the chance to have the presence, support and wisdom of my grand-parents during all this time. I would like to thank them for this, in particular my grand-mother, Louise, to whom this thesis is dedicated.

Next, I would like to thank all my friends, from all over the world, who have never complained about my research worries and who know what it takes to be friends.

Final and nonetheless very special thanks go to Catherine.

Dedication

This thesis is dedicated to my grand-mother, Louise Bourhis, née Rouat.

Contents

List of Tables

List of Figures

Chapter 1

Introduction

1.1 Background And Motivation

The performance of the delivery process of Architectural/Engineering/Construction and Facility Management (AEC&FM) projects is measured in terms of construction safety, time, quality and cost. Assuring good performance requires efficient and reliable performance control processes. This is true for projects managed in a traditional manner, particularly for projects using the Lean Construction management approach [60, 87]. Control processes include [87]:

1. *A forward information flow* that drives the process behavior. In the AEC&FM industry, the forward information flow corresponds to the flow of information resulting from design, planning and management activities.

2. *A feedback information flow* for monitoring purposes. The feedback flow is typically used to adjust the forward information flow and management processes in order to meet the overall expected project performance. In the construction industry, for instance, the feedback flow results from construction monitoring activities.

The current state of the AEC&FM industry is that control processes are inefficient, mainly because they still rely heavily on manual, partial and often inaccurate data collection and processing [80, 85, 87, 102].

The lack of interoperability has been identified as one major reason for these inefficient control processes [35, 43]. To respond to this situation, research efforts are directed toward the development of database systems that aim at rationalizing, streamlining and relating the data pertaining to a given project in order to extract valuable information for efficient, and potentially automated, project control [39,

112, 113]. These systems are often referred to as Building Product Models or Building Information Models (BIMs) [24, 40]. In this thesis, they are referred to as Project Information Models (PIMs) in order to consider any AEC&FM project — not only buildings, but also infrastructure and industrial facilities.

Currently, PIMs can however only partially improve project process flows. While they could significantly impact forward process flows, they remain constrained by the inefficiency and unreliability of currently achieved performance feedback information flows [80, 85, 102]. Research efforts are thus also being conducted, driven by new technologies, with the aim of developing efficient and reliable Automated Data Collection (ADC) systems for efficient project performance control, and ultimately Automated Project Performance Control (APPC) [87].

Current efforts address the automated collection and processing of different data types, such as resource locations [9, 26, 100, 109] and material properties [36, 50, 79, 69, 116]. However, efficient, accurate and comprehensive project three-dimensional (3D) as-built status monitoring systems are only emerging. They are being based on broadly accepted and rapidly growing commercial *3D imaging* technologies, in particular terrestrial *LAser Detection And Ranging (LADAR)* technologies, also referred to as *laser scanning* or *range imaging* technologies. However, commercial systems either only allow data visualization [41, 68, 75, 110] or require time-consuming and skillful manual data analysis to segment the original data at the object level and perform measurements — even with current top-of-the-line point cloud management software such as Trimble® RealWorks®[119] or Leica® CloudWorx®[77]. The AEC&FM industry could thus better benefit from range imaging technologies if laser scanned data could be analyzed more efficiently and potentially automatically in order to be organized at the object level [30, 108].

1.2 Objectives

The overall objective is therefore to develop an accurate, robust, efficient and automated system for extracting from a site laser scan the as-built point cloud of each scanned project 3D object.

By conducting many scans during the entire construction, and later operation, of a project, and using such a system to extract from them as-built 3D information about the project 3D objects, a **Project 4D Information Model (P4dIM)**, storing the 3D as-built status of each project 3D element over time, could be automatically built. This model, which can be seen as a portion of the entire PIM, would then support multiple APPC applications identified earlier such as automated 3D progress tracking, automated dimensional QA/QC and automated structural health monitoring.

Sub-objectives are focused on the object recognition method that is developed here as well as the applications of the method that are explored:

3D Object Recognition Method:

- Develop an approach for accurate, efficient, robust and as automated as possible recognition of project 3D objects in site laser scans.
- Analyze the performance of the developed approach with real-life data, and conclude with respect to its limitations and identify aspects in which it could be improved.

Applications:

- Demonstrate how the developed 3D object recognition approach enables the automated construction of a P4dIM.
- Investigate the possibility and analyze the performance of using a P4dIM constructed with the developed approach to support APPC applications such as automated 3D project progress tracking and automated dimensional QA/QC.

In summary, the hypothesis that this thesis is testing is that a method exists by which particular 3D objects may be reliably recognized in 3D construction images.

1.3 Scope

The scope of this thesis is on industrial construction sites with expansion to other sectors of construction to follow in subsequent research. It is focused on developing a basic approach for object recognition in 3D construction images and only begins to explore the potential applications.

1.4 Methodology

The new method presented in this thesis was based on an iterative process of literature review, algorithm and software development, laboratory experimentation, and eventually full scale field deployment and experimentation. This explains the distribution of the literature review and references to related work throughout the thesis document.

1.5 Structure of the Thesis

This thesis presents the results of the research that has been conducted toward achieving these objectives.

Chapter 2 first presents the context of construction project management objectives and their relationship to emerging automated data acquisition paradigms. Performance metrics and objectives are established for 3D object recognition systems within this context. 3D range imaging technologies and their potential impact on industry practices are presented. The limitations of current systems for 3D image processing in the AEC&FM industry lead to the review of existing approaches for automated 3D object recognition. 3D CAD modeling and registration technologies available to the AEC&FM industry are then introduced resulting in the reformulation of the classic 3D object recognition problem in this specific context. The expected performance of existing automated 3D object recognition solutions to this new problem is finally reviewed.

Chapter 3 presents a novel approach for 3D object recognition in 3D images that is developed specifically for taking better advantage of the 3D modeling and registration technologies available in the AEC&FM industry context.

Chapter 4 presents experimental results demonstrating the performance of the proposed approach in terms of accuracy, efficiency, robustness and level of automation.

Finally, Chapter 5 presents experimental results that demonstrate how the developed approach can be used to automatically construct a P4dIM enabling multiple APPC applications, in particular automated construction 3D progress control and automated dimensional QA/QC. Two other interesting applications are also presented including: planning for scanning and strategic scanning.

Chapter 6 summarizes the contribution of this research. The limitations of the developed approach and of its use for constructing of P4dIMs are reviewed, and areas of future research suggested.

Chapter 2

Literature Review

This chapter presents literature related to the context of developing a new approach to 3D object recognition in construction 3D images. The context of construction project management objectives and their relationship to emerging control and automated data acquisition paradigms is presented (Sections 2.1 and 2.2). The emerging 3D imaging industry and its relationship to the industrial construction sector is described (Section 2.3). Performance metrics and qualitative objectives for a new automated 3D object recognition method within this context are established (Section 2.4). The general object recognition problem is explored with the intent of identifying an existing solution to the problem in our context (Section 2.5). Specificities of the AEC&FM industry context, namely the prevalence of 3D design models and the existence of 3D positioning technologies, are then explored leading to a reformulation of the classic 3D object recognition problem reflecting the opportunities provided by these technologies within the scope of this research (Section 2.6). Finally, the performance of the existing automated 3D object recognition techniques within this new framework is reviewed, and opportunities for better-performing solutions are identified (Section 2.7).

2.1 Performance-driven Projects and Control Processes in the AEC&FM industry

The performance of the delivery process of Architectural/Engineering/Construction and Facility Management (AEC&FM) projects is measured in terms of construction safety, time, quality and cost. Assuring good performance requires efficient and reliable performance *control processes* (see Figure 2.1). This is true for projects managed in a traditional manner, particularly for projects using the Lean Construction management approach [60, 87]. Control processes include [87]:

1. *A forward information flow* that drives the process behavior. In the AEC&FM industry, the forward information flow corresponds to the flow of information resulting from design, planning and management activities.

2. *A feedback information flow* for monitoring purposes. The feedback flow is typically used to adjust the forward information flow and management processes in order to meet the overall expected project performance. In the construction industry, for instance, the feedback flow results from construction monitoring activities.

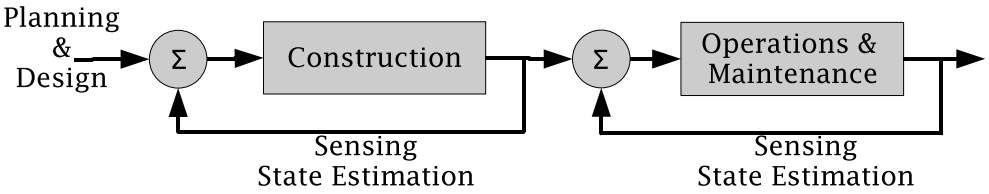

Figure 2.1: Illustration of control processes in the AEC&FM industry.

2.2 Feedback 3D Information Flows

Progress tracking and *dimensional quality assessment and quality control (QA/QC)* are two of the most important feedback information collection activities performed on construction projects. Decision making performance, and consequently project success, undeniably depend on accurate and efficient progress tracking [10, 50, 85] and dimensional QA/QC [8, 30, 50, 51].

Dimensional QA/QC relies entirely on the collection of information about the as-built 3D shape and pose of project 3D elements. Progress tracking requires collecting information about the as-built construction status of project elements, in particular 3D elements [30]. For 3D elements, the as-built construction status — *i.e.* not-built, partially built or entirely built — can actually be deduced from information about their as-built 3D shapes and poses. As a result, **the accurate and efficient tracking of the as-built 3D shape and pose of project 3D objects over time would enable not only more efficient dimensional QA/QC, but also progress tracking [30], and in fact other critical AEC&FM life cycle monitoring applications such as displacement analysis for structural health monitoring [29, 91]**.

However, current AEC&FM systems for tracking the as-built 3D shape and pose of project 3D objects only provide partial information, and this information

is also often inaccurate. Not only do they provide incomplete and unreliable information, but they also rely on manually intensive and inefficient data collection [84, 97, 100, 102]. As an example, current tools available for 3D shape and pose measurement include measurement tapes, levels or, sometimes, total stations. Furthermore, it is estimated in [30] that, only a decade ago, *"approximately 2% of all construction work had to be devoted to manually intensive quality control and tracking of work package completion"*, and very little improvements have been noticed since [102]. As a result, it can be concluded that, on a typical construction project, significant amounts of labor, time and money are spent on collecting incomplete and unreliable 3D information. This is particularly unacceptable when considering that the construction industry has no margin for wasting money. Construction contractors claim an average small net profit of 2% to 5% [115, 65], and, correspondingly, the construction industry typically presents higher business failure rates than other industries. For instance, in 2007, $1,095$ of the roughly $260,000$ firms in the Canadian construction industry filed bankruptcy, representing 16% of all business bankruptcies in Canada that year [111].

In conclusion, **the AEC&FM industry could greatly benefit from systems enabling more accurate, efficient and comprehensive collection of information about the 3D shape and pose of project 3D objects [8, 30]**.

2.3 Leveraging New Reality-Capture Sensors

New reality-capture sensors can be leveraged for more efficient, accurate and comprehensive project as-built 3D status monitoring [8, 52, 71, 85]. They include: global positioning technologies (*e.g.* Global Navigation Satellite Systems (GNSSs)), Radio Frequency IDentification (RFID) systems, digital cameras, and laser scanners, also referred to *LAser Detection And Ranging (LADAR)*.

GNSS and RFID technologies are being investigated to track 3D information, typically resource locations [26, 28, 78, 95, 109, 124]. They are however clearly unadapted to the sensing of accurate 3D shape and pose information for the intended applications.

Digital cameras are used to record project as-built status and research is being conducted to develop algorithms for automated recognition of project 3D objects in digital pictures [21, 22]. However, performance results reported to date relate to highly structured and relatively small experimental data sets, and are focused on only large objects or surfaces. Even under these conditions, recall rates are low. Under the realistic field conditions considered in this thesis the recall rates would be even lower and of no practical utility. In the work reported by Kim and Kano in [68], which uses the author's approach of using 3D CAD perspective as *a*

priori information [19], results improve but are still handicapped by the limitations presented by 2D image data. Overall, research efforts which attempt to leverage digital cameras for 3D object recognition face the inherent difficulty of extracting 3D information from 2D images.

2.3.1 Laser Scanning

In contrast, *laser scanners* enable the remote acquisition of very accurate and comprehensive project 3D as-built information in the form of *dense range point clouds*, also referred to as *range images*, or simply *laser scans*.

Laser scanners used in the AEC&FM industry are based on two different technologies: *time-of-flight* (also referred to as *pulsed*) or *phase-based* technology [63]. With both technologies, each range point is acquired in the equipment's spherical coordinate frame by using a laser mounted on a pan-and-tilt unit. The pan-and-tilt unit provides the spherical angular coordinates of the point. The range is however calculated using different principles. Time-of-flight scanners send a laser pulse in a narrow beam toward the object and deduce the range by calculating the time taken by the pulse to be reflected off the target and back to the scanner. Phase-based scanners measure phase shift in a continuously emitted and returned sinusoidal wave, the distance to the measured surface being calculated based on the magnitude of the phase shift [63]. While phase-based and pulsed laser scanners typically achieve similar point measurement accuracies (1.5 mm to 15 mm depending on the range), they differ in scanning speed and maximum scanning range. Pulsed scanners can typically acquire points at distances of up to a kilometer, while phase-based scanners are currently limited to a maximum distance of 50 meters. However, phase-based scanners present scanning speeds of up to $500,000$ points per second, while pulsed scanners currently achieve speeds of a maximum of $10,000$ points per second [63].

Whatever the range measurement principle, **laser scanning is arguably the technology that is currently the best adapted for accurately and efficiently sensing the 3D status of projects [7, 31, 44] for application to progress tracking and dimensional quality control**.

In fact, as illustrated in Figure 2.2, the terrestrial laser scanning hardware, software and services market has experienced an exponential growth in revenues in the last decade, with the AEC&FM industry as one of its major customers. This indicates that owners and contractors clearly see the potential of using this technology for reliably and comprehensively sensing the 3D as-built status of construction projects.

Despite this industry-wide agreement that laser scanners can have a significant

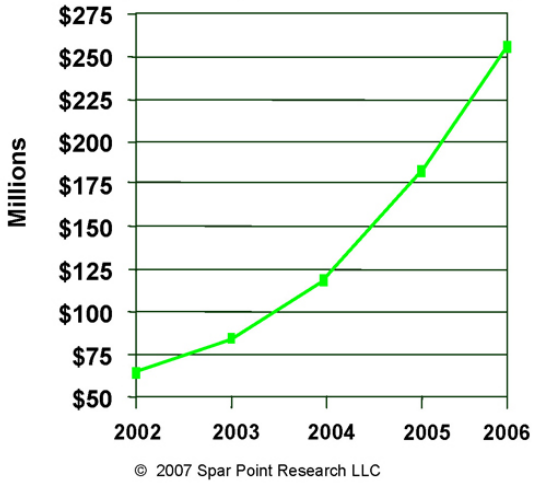

Figure 2.2: Total terrestrial laser scanning market (hardware, software and services) [53] (with permission from Spar Point Research LLC).

impact on the industry's practices in project 3D as-built status sensing, it is noticed that laser scans are currently used only to (1) extract a few dimensions, or (2) capture existing 3D conditions for designing new additional structures. Most of the 3D information contained in laser scans is discarded, and laser scans are not used to their full potential. A reason for this situation is that, as described in Section 2.2, it is necessary, in order to efficiently support control processes such as 3D progress tracking and dimensional QA/QC, that 3D as-built data be organized (segmented) **at the object level**. However, **no significant advances have yet been reported in the accurate and efficient extraction from site laser scans of as-built 3D information accurately organized at the object level**. Commercial systems either only allow data visualization [41, 68, 75, 110] or require time-consuming and skillful manual data analysis to segment the original data at the object level and perform measurements — even by using current top-of-the-line point cloud management software such as Trimble® RealWorks®[119] or Leica® CloudWorx®[77].

2.4 Performance Expectations for 3D Object Recognition in Construction

Since a reliable, automated 3D object recognition system in construction does not currently exist, the literature has no directly adoptable metrics. In fact, for such a system, no performance target or expectations in terms of accuracy, robustness, efficiency and level of automation have ever been estimated and reported. The

author attempts here to estimate, mostly qualitatively, such performance expectations. These are used in the rest of this thesis for assessing the performance of automated 3D object recognition systems within the investigated context.

Accuracy: Accuracy refers to the performance of the system to correctly extract from a given scan all the as-built point clouds corresponding to project 3D objects, and to correctly assign each extracted range point to the right object. Such performance can be measured using fundamental recall rate, specificity rate, *etc.* While perfect recall rates could be expected, the recognition of the as-built point cloud of certain project 3D objects could also be considered more critical than of other ones. For instance, when considering a scan of a steel structure, it can be argued that it is more critical, both for dimensional quality control and progress tracking, to be able to correctly extract the as-built point clouds of all beams and columns than of panel braces. In the investigated context, it is thus difficult to quantitatively set targets for performance measures such as recall rate, and a qualitative analysis of object recognition results may be preferred. Nonetheless, these fundamental measures are used in this thesis with the goal of setting benchmarks that can be used for comparison with future research results.

Robustness: Robustness refers to the performance of the system to correctly extract 3D objects' point clouds in laser scans with different levels of clutter and, more critically, occlusions. This is very important since, as is shown in Figure 2.3, objects are often scanned with partial and sometimes significant occlusion. In the investigated context, an object recognition system should be able to recognize objects with high levels of occlusions.

Note that occlusions can be categorized in two types: (1) *internal occlusions* are due due to other project 3D objects (*e.g.* columns and walls); and (2) *external occlusions* are due to non-project objects (*e.g.* equipment and temporarily stored materials). A good system should be robust with both types of occlusions.

Efficiency: Efficiency refers to the speed of the 3D object recognition system. Such a system is intended to support many applications such as progress tracking and dimensional QA/QC that provide key information to design-making processes. Thus, having real-time project 3D status information would be preferable. However, as discussed previously, currently available systems for progress control provide information on a daily basis at best, and, as is reported by Navon and Sacks [87], construction managers do not (yet) seem to have a strong desire for information updates at a higher frequency than daily. Since the time needed to conduct a site laser scan is in the order of

minutes (at most one hour), it can be concluded that it would be appropriate if a system for extracting from a scan all the clouds corresponding to project 3D objects took no more than a few hours.

Level of automation: Having a fully automated system is preferable since it would not be subject to human error and would probably be more efficient. However, as described in Section 2.2, current approaches for recording the 3D as-built information are manually intensive. Therefore, a system with some level of automation, and consequently less manually intensive than current approaches, while providing information at least as accurate would be an improvement.

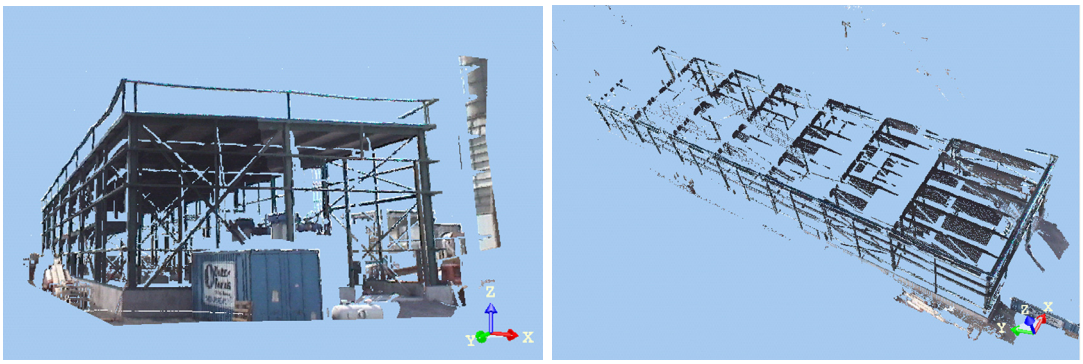

Figure 2.3: A typical construction laser scan of a scene with clutter, occlusions, similarly shaped objects, symmetrical objects, and non search objects.

It should be emphasized that no approach based on 2D images to date comes close to these performance objectives [21, 22]. This is why the industry is adopting 3D imaging as a basis for field applications. This thesis is the first effort to extract object 3D status information automatically from construction range images and thus it will establish a benchmark for performance that subsequent work will improve on.

In the next section, classic approaches for 3D object recognition from the robotics and machine vision literature are summarized though not extensively reviewed.

2.5 Automated 3D Object Recognition in Range Images

The problem of automatically recognizing construction projects' 3D objects in site sensed 3D data is a *model-based 3D object recognition* problem. Model-based 3D

object recognition problems are a sub-set of *pattern matching* problems [13].

The literature on model-based 3D object recognition is extensive. Solutions are designed based on the constraints characterizing the problem in its specific context. In the specific problem investigated here, it can be assumed at this point that: (1) search objects may have any arbitrary shape; (2) they can be viewed from any location, meaning that their pose in the sensed data is *a priori* unknown; (3) the relative pose of two objects in the sensed data is also *a priori* unknown; and (4) they can be partially or fully occluded.

Object recognition systems rely on the choice of *data representations* into which the sensed data and the search object models can be obtained (possibly after conversion) and from which both data can be described using similar *features* (or *descriptors*) [13]. The choice of the data representation determines the recognition strategy and thus has a significant impact on the efficiency and robustness of the recognition system. An adequate representation is unambiguous, unique, not sensitive, and convenient to use [13]. However, the performance required by the application generally lead to the choice of representations that compromise some of these characteristics for the benefit of others. In the case of the problem investigated here, a data representation should be unambiguous and unique, because this would ensure that each object can only be represented in one distinctive way [27]. The choice of a data representation must be accompanied by robust techniques for extracting compatible features from both object models and input range image.

Model-based object recognition systems that can be found in the literature use data representations with different levels of complexity. 3D data representations that have been used in the literature include parametric forms, algebraic implicit surfaces, superquadrics, generalized cylinders and polygonal meshes [13]. Polygonal meshes are very popular for at least three reasons: (1) meshes can faithfully approximate objects with complex shapes (*e.g.* free-forms) to any desired accuracy (given sufficient storage space); (2) 3D points, such as range points, can easily be triangulated into meshes; and (3) a variety of techniques exists for generating polygonal mesh approximations from other 3D data respresentations such as implicit surfaces [89] or parametric surfaces [73]. Triangles are the most commonly used polygons in polygonal meshes.

In the case of the problem investigated here, search objects are construction project 3D objects. The specificity of construction project 3D objects is that they are often designed in 3D using Computer-Aided Design (CAD) modeling software, and the object 3D models are generally parametric forms. 3D design is now particularly standard in industrial projects which are the specific type of projects identified within the scope of this research. Parametric forms could thus be used as the search object data representation for the object recognition problem inves-

tigated here. However, as noted by Besl [42], parametric forms are more generally used for their completeness which makes them useful as a source of an initial object specification, from which other representations can be generated, in particular polygonal meshes that can be more easily used in object recognition applications. Additionally, in the case of the problem investigated here, as-built construction 3D objects often have deformed parametric shapes which can be considered as *arbitrary shapes*, more commonly referred to *free-forms*.

Significant research efforts are conducted in the field of *surface matching* for solving *free-form 3D object recognition* problems. An excellent survey of free-form object representation and recognition techniques can be found in [27]. Data features that have been investigated include spherical representations [55], generalized cones [88], deformable quadratics [94], global surface curvatures [118] (although these are admittedly impractical), and different local (point) surface or shape descriptors such as local curvatures [18, 38], polyhedral meshes [93, 96], surface patches [114, 12], point signatures [32], spin images [64], harmonic shape images [126], and more recently 3D tensors [81].

Several of these techniques, typically those based on global shape representation [94, 118], cannot be used for object recognition in complex scenes with occlusions. Additionally, techniques based on spherical representations require the modeled objects to have a topology similar to the one of the sphere [55]. However, construction objects often have topologies that are different from the one of the sphere.

Among the other techniques, only a few report performances in complex scenes, in particular scenes with occlusions. Those that claim and demonstrate such robustness all use the polygonal (triangular) mesh as the data representation of both the sensed data and the search object models. Additionally, they are all based on local surface or shape descriptors. They include the spin image approach [64], the harmonic shape image approach [126], and the 3D-tensor approach [81]. These three techniques are described below.

Johnson and Hebert [64] propose a recognition algorithm based on the *spin image*, a 2D surface feature describing the local surface around each mesh point. A spin image is more exactly a 2D histogram in which each bin accumulates neighboring mesh points having similar parameters with respect to the investigated mesh point. For each neighboring point, these parameters are the radial coordinate and the elevation coordinate in the cylindrical coordinate system defined by the oriented mesh point of interest. Recognition is then performed by matching sensed data spin images with the spin images of all search objects. This technique shows strengths including robustness with occlusions. In experiments presented in [64], objects up to 68% occluded were systematically recognized. However, it remains limited in three ways: (1) the recognition performance is sensitive to the resolution

(bin size) and sampling (size of the spin image) of spin images; (2) spin images have a low discriminating capability because they map a 3D surface to a 2D histogram, which may lead to ambiguous matches; and (3) although a technique is presented in [64] for accelerating the matching process, matching is done one-to-one so that the recognition time grows rapidly with the sizes of the model library and of the sensed data. Then, Zhang and Herbert [126] present a technique that uses another local (point) surface descriptor, the *harmonic shape image*. A harmonic shape image is constructed by mapping a local 3D surface patch with disc topology to a 2D domain. Then, the shape information of the surface (curvature) is encoded into the 2D image. Harmonic shape images conserve surface continuity information, while spin images do not, so that they should be more discriminative. Additionally, while the calculation of harmonic shape images requires the estimation of the size of each image, it does not require the estimation of any bin size. The recognition process is then similar to the one use in the spin image approach [64]. The results reported on the performance of this technique with respect to occlusions are limited. In particular, the expected improved performance compared to the spin image approach is not demonstrated. Additionally, similarly to the spin image approach, this technique has two main limitations: (1) harmonic shape images have a limited discriminating capability because they map a 3D surface to a 2D image; and (2) matching is done one-to-one so that the recognition time of this technique grows rapidly with the sizes of the model library and of the sensed data.

Finally, Mian et al. [82, 81] have recently presented a technique based on another local shape descriptor: the *3D tensor*. A 3D tensor is calculated as follows. A pair of mesh vertices sufficiently far from each other and with sufficiently different orientations is randomly selected. Then a 3D grid is intersected with the meshed data. The pose of the grid is calculated based on the paired vertices and their normals. Each tensor element is then calculated as the surface area of intersection of the mesh with each bin of the grid. The sizes of the grid and of its bins are automatically calculated. They respectively determine the degree of locality of the representation and the level of granularity at which the surface is represented. The recognition is performed by simultaneously matching all the tensors from the sensed data with tensors from the 3D models. Once an object is identified, its sensed range points are segmented from the original data and the process is repeated until no more objects are recognized in the scene. The main advantage of this technique is that 3D tensors are local 3D descriptors, so that they are more discriminative than spin images or harmonic shape images. Experiments were performed and an overall recognition rate of 95% is achieved, and the approach can effectively handle up to 82% occlusion. Experimental comparison with the spin image approach also reveal that this approach is superior in terms of both accuracy, efficiency and robustness. However, similarly to the previous ones, this technique has one main limitation:

the recognition time of this technique grows rapidly with the sizes of the model library and the sensed data.

Besl [42] reviewed the difficulties in matching free-form objects in range data using local features (point, curve, and surface features). In particular, as seen with the three techniques above, the computational complexity of such matching procedures can quickly become prohibitive. For example, brute-force matching of 3D point sets was shown to have exponential computational complexity. Because of this, all the works using local features have developed techniques to reduce the amount of computation required in their feature matching step. For example, Johnson and Hebert [64] use Principal Component Analysis (PCA) to more rapidly identify positive spin image matches. Similarly, Mian et Al. [81] use a 4D hash table. Nonetheless, these techniques remain limited in the case of large model libraries and range images.

The result of this review of 3D object recognition techniques is that techniques based on local shape descriptors are expected to perform better in the context of the problem investigated here. Furthermore, the recent work by Mian et al. [81] seems to demonstrate the best performance with such problems.

However, the problem investigated here presents two additional conditions that, with the current assumptions, none of the above techniques can overcome:

- Construction models generally contain many objects that have the same shape and typically the same orientation (*e.g.* columns, beams), so that they cannot be unambiguously recognized, by the methods described above.
- Many construction 3D objects present symmetries so that their pose cannot be determined unambiguously.

In the next section, some sources of *a priori* information available within the AEC&FM context are however presented that can be leveraged to remove those constraints.

2.6 A Priori Information Available in the AEC&FM Context

Within the context of the AEC&FM industry, two sources of a priori information can be leveraged, that are typically not available in other contexts: project 3D CAD models and 3D registration technologies.

2.6.1 3D CAD Modeling

In recent decades, the increase in computing power has enabled the development of 3D design with 3D CAD engines. In 3D CAD design, the construction project (*e.g.* building, infrastructure), and consequently all the 3D objects it is constituted of (*e.g.* beams, columns), are modeled entirely in 3D. A project 3D CAD model thus constitutes a list, or database, of CAD representations of all the 3D objects which can be used by the techniques presented in the previous section for automatically recognizing project 3D objects in construction range images.

Furthermore, it has been shown that, despite the use of different methods for improving the efficiency of their matching steps, the efficiency of effective techniques such as the three ones identified at the end of Section 2.5 remains poor. The reason is that recognition is based on matching hundreds of data features one-on-one, and is due to the third of the project assumptions presented in page 12: the relative pose of two objects in the sensed data is also *a priori* unknown. However, one important characteristics of project 3D CAD models is that they provide a *spatially organized*, or *3D-organized*, list of CAD representations of the project 3D objects. In a 3D CAD model, the relative pose of each pair of objects has a meaning, and this relative pose is expected to be the same as in reality once the project is built. Thus, within the context of the problem investigated here, the third assumption of the general object recognition problem can be reversed. This implies that, as soon as one 3D object is fully recognized (shape and pose) in a site laser scan, then it is known where all the other project 3D objects are to be recognized. This characteristic could be leveraged by techniques such as the three ones identified at the end in Section 2.5 to significantly reduce the complexity of their feature matching process.

Furthermore, it can be noted that, from a given 3D view point, occlusions of project objects due to other project objects, referred to as *internal occlusions*, are expected to be the same in reality and in the 3D model. This is another interesting characteristic, because, despite some demonstrated robustness, the recognition rate of the techniques presented at the end of the previous section generally rapidly decrease passed a certain level of occlusions. Even the 3D tensor -based technique [81] performs well with occlusions only to a certain level ($\approx 80\%$). However, it can be noted that the data descriptors used by the techniques above are object-centered, so that they cannot describe internal occlusions and consequently take them into account in the matching strategy.

In conclusion, by using AEC&FM project 3D CAD models, the problem investigated here can be significantly simplified. In particular, by using project 3D CAD models with recognition techniques such as the 3D tensor -based one proposed by Mian et a. [81], the complexity of their matching step can be significantly reduced. The recognition (shape and pose) of a single object would enable targeting the

recognition of all the remaining objects. However, these techniques would not be able to take advantage of another interesting characteristic of 3D CAD models, namely that, from a given view point, the project 3D CAD model and the range image are expected to present the same internal occlusions.

2.6.2 3D Registration

Project 3D models are generally geo-referenced or at least project-referenced. Field data, such as laser scans, can also be geo-referenced or project-referenced by using some 3D registration techniques that are available specifically within the AEC&FM context.

Registering the project 3D CAD model and range image in a common coordinate frame would enable further reducing the complexity of the investigated problem. Indeed, if the 3D CAD model and range image are registered in a common coordinate system, then they are aligned in 3D, and, consequently, the second of the project assumptions presented in page 12 can be reversed: it can now be assumed that the pose of all project 3D objects in the sensed data is *a priori* known. So, compared to using the 3D CAD model only, combining both 3D CAD model and registration information, it is known *a priori* where all project 3D objects are to be recognized (searched) in the range image. In this context, the efficiency of techniques such as the three ones described at the end of section 2.5 could be further improved.

Techniques for 3D registration of sensed 3D data are generally categorized in two groups based on the positioning tracking system they use [106]:

Dead Reckoning (DR) positioning uses angular and linear accelerometers to track changes in motion. Using the motion sensed information, the current pose of the object on which the sensing system is installed is deduced from its previous pose in time.

One main limitation of these systems is that they can only provide positions in a local object-centered coordinate frame. In order to provide positions in a global non-object centered coordinate system, in our case a geo-referenced or project-referenced coordinate system, it is necessary that the initial pose be known in that coordinate system, which can only be achieved by using a global positioning technique. Additionally, the accuracy of dead reckoning systems rapidly decreases over time.

Global positioning uses natural or man-made landmarks, the position of which is known in the global coordinate frame of interest. Using different machine

vision techniques, the current position with respect to these landmarks, and consequently the global position, can be calculated.

The advantage of this technique is that the global position is known at any time with an accuracy that is independent from the previous measurement. The limitation of this technique is that landmarks must be available any time that the position must be estimated, which may require the knowledge of a large amount of landmarks.

In practice, particularly in automated or assisted navigation applications, these two registration techniques are often implemented complementarily since their advantages are complementary [106].

In the research conducted here, it is expected that scans be performed in a static manner. As a result, it is not possible to use DR positioning techniques to geo-reference or project-reference them. Thus, only global positioning techniques can be used. In the AEC&FM context, two types of global positioning systems are available:

Global Navigation Satellite Systems (GNSSs) enable the positioning (registration) of 3D data into the geocentric coordinate system. Currently existing GNSSs include the NAVSTAR system (often referred to *the* Global Positioning System (GPS)), the GLONASS system, and soon the Galileo and other systems [57]. GNSSs achieve different levels of accuracies depending on the system itself and whether differential GPS (DGPS) and/or post-processing techniques are applied. In the case of Real-Time Kinematic (RTK) GPS, a DGPS technique, positioning accuracies can be as high as: ± 1 *cm* for horizontal location and ± 2 *cm* for vertical location. Higher accuracies may even be achieved by combining additional post-processing techniques [25, 99, 92].

In the AEC&FM industry, GNSS technologies are already investigated to track the pose of important resources for applications as diverse as productivity tracking, supply chain management [95] and lay-down yard management [26].

Benchmark-based registration: The AEC&FM industry uses local reference points, referred to as *benchmarks* or *facility tie points*, as means to perform project registration in surveying activities. Benchmarks are defined on-site (at least three are necessary), and define a project 3D coordinate frame. The project 3D CAD model is then designed (*e.g.* project 3D model) with reference to this coordinate frame. When acquiring site 3D data, like laser scans, the obtained data is referenced in the equipment's coordinate frame. However, by sensing the location of at least three benchmarks in the coordinate

frame of the equipment, the sensed data can be registered in the project coordinate frame. This registration approach enables sub-centimeter registration accuracy.

While both GPS or benchmark-based registration could theoretically be used to register site laser scans in project coordinate systems, the benchmark-based technique is preferred for three reasons:

1. Since benchmarks are already present on site for surveying activities, registering laser scans by using these benchmarks would enable an accurate registration without the need for additional infrastructure. In the case of GPS-based registration, in order to obtain the same level of registration accuracy, a GPS receiver unit would have to be exactly installed on the scanner (note that some laser scanner providers now start designing laser scanners with embedded GPS receivers), a base station would have to be installed for achieving DGPS accuracies, and post-processing techniques would probably also have to be implemented.

2. Using at least three benchmarks a laser scan can be fully registered (the location and orientation of the scanner are known). In contrast, using a single GPS signal, a laser scan cannot be fully registered. Indeed, a single GPS signal (even with DGPS) enables the estimation of the location of an object but not of its orientation. As a result, in GPS-based registration, complete pose estimation would require either (1) mounting multiple GPS receivers (at least three) on the scanner, (2) or using heading, pitch and roll sensors. In both cases, however, the accuracy in the estimation of the scan's orientation would be less accurate than in benchmark-based registration.

3. Finally, since the construction of the project is performed using the site benchmarks as reference points, it seems most appropriate, when having in mind quality control applications, that the registration of site laser scans be performed using these same benchmarks.

2.7 Conclusion on Using Existing 3D Object Recognition Techniques

By using the project 3D CAD model as a 3D-organized list of the search 3D objects and benchmark-based registration for registering the 3D CAD model and the investigated laser scan in a common coordinate frame, the problem of recognizing project 3D objects in site laser scans can be significantly simplified. To reflect these

simplifications, it is reformulated as **developing an approach for accurate, efficient, robust and as automated as possible recognition of project 3D CAD model objects in site laser scans, where the project 3D CAD model and the scans are registered in a common project 3D coordinate frame**.

With this new problem, one significant constraint of the object recognition problem addressed by the techniques described in Section 2.5 is removed: the pose (location and orientation) of each search object is now known *a priori*. The removal of this constraint could be leveraged to significantly reduce the complexity of 3D object recognition techniques.

However, as identified at the end of Section 2.6.1, all these techniques, including the spin image approach [64], the harmonic shape image approach [126] and the 3D-tensor approach [82, 81], use shape descriptors that cannot take 3D CAD model internal occlusions into account. The reason is that the shape descriptors are calculated in object-centered coordinate systems.

Shape descriptors calculated in object-centered coordinate systems are generally preferred to shape descriptors calculated in viewer-centered coordinate systems for one main reason: the objects do not have to be aligned to the view prior to calculate the descriptors. The result is that object descriptions do not change with the view, and, consequently, objects with unknown pose [64] can be more effectively and efficiently recognized. Since, in the AEC&FMindustry, 3D CAD model and 3D registration technologies can be leveraged to remove this constraint of the unknown pose of search objects, shape descriptors calculated in viewer-centered coordinate frames could be investigated. Such descriptors should enable accurate and efficient object recognition in scenes including very high levels of occlusion. The literature on 3D object recognition techniques based on using viewer-centered data descriptors is very sparse, if not inexistent, so that no such data descriptor has been identified.

In Chapter 3, an approach is introduced that uses a viewer-centered data representation, the *range point cloud*. This data representation is calculated from the scanning location and in the coordinate frame of the investigated range image. Its main advantage is that it enables using data descriptors that can take 3D model internal occlusions into account the same way as they are expected to occur in the range image. Ultimately, this enables the recognition of objects with very high levels of occlusions (see performance analysis in Chapter 4), and consequently multiple APPC applications (see Chapter 5). Furthermore, as will be shown in Chapter 5, the approach enables other applications than project 3D object recognition in site laser scans with benefit to the AEC&FM industry.

Chapter 3

New Approach

3.1 Overview

A novel approach is proposed to solve the investigated problem, restated here:

> **Investigated Problem:** *Develop an accurate, robust, computationally efficient and as automated as possible system for recognizing project 3D CAD model objects in site laser scans, where the model and the scans are registered in a common project 3D coordinate frame.*

The approach uses the *range point cloud* (or *range image*) as the 3D object data representation, and simultaneously shape descriptor, for model matching, which enables model internal occlusions be taken into account. Five steps constitute this approach:

1 - 3D CAD Model Conversion: In order to have access to the 3D information contained in project 3D CAD models that are generally in proprietary formats, an open-source 3D format is identified, the STereoLithography (STL) format. This format is chosen because it (1) faithfully retains 3D information from the original 3D CAD model; and (2) enables simple calculations in *Step 3*.

2 - Scan-Referencing: The project 3D model and laser scan registration information is used to register (or reference) the model in the scan's spherical coordinate frame. This step is a prerequisite to the calculation of the as-planned range point cloud conducted in *Step 3*.

3 - As-planned Range Point Cloud Calculation: For each range point (or *as-built range point*) of the investigated range point cloud, a corresponding virtual range point (or *as-planned range point*) is calculated by using the scan-referenced project 3D model as the virtually scanned world. Each point in

the as-planned range point cloud corresponds to exactly one point in the as-built range point cloud. They have the same scanning direction. In the virtual scan, however, it is known from which 3D model object each as-planned range point is obtained.

4 - Point Recognition: For each pair of as-built and as-planned range points, these are matched by comparing their ranges. If the ranges are *similar*, the as-planned range point is considered recognized.

5 - Object Recognition: The as-planned points, and consequently their corresponding as-built range points, can be sorted by 3D model object. As a result, for each object, its recognition can be inferred from the recognition of its as-planned range points.

An algorithmic implementation of this object recognition approach is given in Algorithm 1. Note that it includes additional procedures, *CalculateScanFrustum* and *CalculateVerticesNormals*, the need for which is explained later in this chapter.

The five steps of this approach are now successively detailed in Sections 3.2 to 3.6. The mathematical notations and variable names used in the description of this approach are described in Appendix H. Section 3.7 then rapidly discusses the need for sensitivity analyses with respect to the object recognition performance of this approach.

3.2 Step 1 - Project 3D Model Format Conversion

The 3D information contained in project 3D CAD models must be fully accessible to practically use this approach. Project 3D CAD models generally present the project 3D designed data in protected proprietary 3D CAD engine format (*e.g.* DXF, DWG, DGN, etc). An open-source format must thus be identified into which the 3D CAD model can be converted. This conversion must retain as much of the 3D information originally contained in the 3D CAD model as possible. Additionally, since the project 3D model is used to calculate the as-planned range point cloud (see Step 3 described in Section 3.4), the chosen open-source format must enable this calculation to be as efficient as possible.

Several open-source 3D data formats exist, including the Virtual Reality Modeling Language (VRML) format (now the X3D format), the STandard for the Exchange of Product data (STEP) format (and consequently the Industry Foundation Classes (IFC) format), the Initial Graphics Exchange Specification (IGES) format,

```
Data: Model, Scan
Result: Model.{Object.IsRecognized}
CalculateScanFrustum(Scan)                    // see Algorithm 20 in Appendix D
Step 1 - Convert Model into STL format.
STLconvert(Model)
CalculateVerticesNormals(Model)               // see Algorithm 27 in Appendix F
Step 2 - Reference Model in the coordinate frame of the scan.
ReferenceInScan(Model, T, R)                                  // see Algorithm 2
Step 3 - Calculate As-planned range point cloud.
CalculateAsPlannedCloud(Scan.{P_B}, Model, Scan.Frustum)      // see Algorithm 3
Step 4 - Recognize points.
for each Scan.P_P do
  | RecognizePoint(Scan.P_P, Scan.P_B)                        // see Algorithm 5
end
Step 5 - Recognize objects.
SortPoints(Model, Scan.{(P_P, P_B)})                          // see Algorithm 6
for each Model.Object do
  | RecognizeObject( Model.Object.{(P_P, P_B)})               // see Algorithm 7
end
```

Algorithm 1: Overall program *Recognize-3D-Model* recognizing the 3D CAD model objects in the 3D laser scanned data.

and the STereoLithography (STL) format. These vector graphics markup languages may describe 3D data with only one or a combination of elementary data representations that: (1) approximate object surfaces with facet tessellations, or (2) approximate object volumes with simple 3D parametric forms (*e.g.* 3D primitives).

For the purpose of simplification, only formats that use only one elementary data representation were investigated, and among these, representations based on facet approximations were preferred for three reasons:

1. They can faithfully represent the surface of 3D objects with any shape, thus retaining almost all the 3D information from original 3D CAD models.

2. They enable a simple calculation of the as-planned range point cloud (Step 3). The underlying reason for this is that polyhedra's facets are flat (2D) bounded surfaces.

Finally, among these 3D formats based on facet approximation, the *STereoLithography (STL)* format is chosen. The reason for this choice is that the STL format approximates the surfaces of 3D objects with a tessellation of triangles, and this approximation particularly enables a simple and efficient calculation of the as-planned range points (Step 3). See Appendix A for a detailed description of the STL format.

3.3 Step 2 - 3D Registration

As discussed in Section 2.6.2, the project 3D model and 3D laser scans can be most effectively and efficiently registered in a common coordinate system by using *benchmark-based project registration*.

This type of registration consists in identifying points (or benchmarks) in one data set and pairing them with their corresponding points in the second data set and then automatically calculate the transformation parameters (translations and rotations) to register the two data sets in the same coordinate system. This problem is generally referred to as the *rigid registration between two sets of 3D points with known correspondence* problem [58]. It defers from the *general rigid registration between two sets of 3D points* problem for which no point correspondence is *a priori* known [107].

When matching corresponding benchmark, it is unlikely that the points match exactly. As a result, the *rigid registration between two sets of 3D points with known correspondence* problem must be approached as an optimization problem. A good reference to this problem can be found in [58].

This problem is generally mathematically stated as: automatically identifying the rotation matrix ($\mathcal{R}$), translation matrix ($\mathcal{T}$) and scaling factor (k) that minimize a cost function that measures the closeness between the two point sets with n corresponding points ($n \geq 3$). The cost function is generally the mean squared error, $\overline{\epsilon_{Reg}}$, of the Euclidean distances between each point in one set, x_i and its corresponding point in the other set, y_i, registered in the same coordinate frame, calculated as:

$$\overline{\epsilon_{Reg}}\,(k, \mathcal{R}, \mathcal{T}) = \frac{1}{n}\sum_{i=1}^{n} \|y_i - (k\mathcal{R}x_i + \mathcal{T})\|^2 \tag{3.1}$$

Solutions to this problem are presented in [14] and [58], and a more robust refined one is presented in [120]. Iterative and noniterative algorithms for finding the solution are proposed in [61] and [59] respectively.

In the case of the benchmark-based registration problem, it can however be noticed that there is no scaling issue, in which case $k = 1$. The problem is thus redefined here as identifying the rotation matrix ($\mathcal{R}$) and translation matrix ($\mathcal{T}$) that minimize mean squared error, $\overline{\epsilon_{Reg}}$ calculated as:

$$\overline{\epsilon_{Reg}}\,(\mathcal{R}, \mathcal{T}) = \frac{1}{n}\sum_{i=1}^{n} \|y_i - (\mathcal{R}x_i + \mathcal{T})\|^2 \tag{3.2}$$

The *Step 3* of the proposed 3D object recognition approach, presented in Section 3.4, requires the 3D model be registered in the scan's spherical coordinate

frame. Therefore, first of all, the matrices $\mathcal{R}$ and $\mathcal{T}$ calculated during the registration process are used to register each vertex of the STL-formatted 3D model into the laser scan's Cartesian coordinate frame, and then the coordinates of each vertex are recalculated in the scan's spherical coordinate frame. The algorithmic implementation of this process is presented in Algorithm 2. Appendix B details the spherical coordinate frame used here, as well as the transformation formulas between the Cartesian and this spherical coordinate frames.

```
Data: Model, 𝒯, ℛ

for each Model.Object do
    for each Model.Object.Facet as F do
        for each F.Vertex do
            F.Vertex.[XYZ]_Scan ← ℛ (F.Vertex.[XYZ]_Model) + 𝒯
            F.Vertex.n⃗ ← ℛ (F.Vertex.n⃗)
            F.Vertex.[PTR]_Scan ← CartesianToSpherical(F.Vertex.[XYZ]_Scan)
                                        // see Algorithm 11 in Appendix B
        end
        F.n⃗ ← ℛ (F.n⃗)
    end
end
```

Algorithm 2: Procedure *ReferenceInScan* referencing the STL-formatted project 3D model in the scan's spherical coordinate frame.

The optimal (minimal) value of $\overline{\epsilon_{Reg}}$ provides some information about the overall quality of the registration optimization process. This value is thus used in *Step 4* as *a priori*information about the expected matching quality between each pair of as-built and as-planned points. In the rest of this thesis, this optimal value of $\overline{\epsilon_{Reg}}$ is referred to as the *registration error* or *referencing error*, and is also noted $\overline{\epsilon_{Reg}}$.

Finally, it is remined that the overall procedure for performing the rigid registration of two sets of 3D points consists in: (1) manually associate at least three benchmark points in the range point cloud to their corresponding benchmark points in the 3D model, and (2) run the registration algorithm to obtain the matrices $\mathcal{R}$ and $\mathcal{T}$ minimizing $\overline{\epsilon_{Reg}}$ and register the two point sets in the same coordinate frame. As a result, although this registration procedure is generally not time consuming, it is not fully automated.

3.4 Step 3 - Calculation of the As-planned Range Point Cloud

The *3D model scan-referencing* (*Step 2*) enables the virtual world defined by the project 3D model to be viewed from the viewpoint of the scanner, in a similar manner to virtual or augmented reality [104, 17]. From this viewpoint, it is then possible to calculate a *virtual range point cloud* (or *as-planned range point cloud*) corresponding to the investigated real range point cloud (or *as-built range point cloud*), using the 3D model as the virtually scanned world. For each *as-built range point*, a corresponding *as-planned range point* having the same scanning direction can be calculated in the virtual world, as summarized in Algorithm 3. Note that, Algorithm 3 includes the function *CalculateBVH* calculating a bounding volume hierarchy of the 3D model, BVH. The need for calculating this bounding volume hierarchy will be addressed in Section 3.4.2, and its calculation is detailed in Appendix D.

Data: Scan.$\{P_B\}$, Model, Scan.Frustum
Result: Scan.$\{P_P\}$

BVH ← `CalculateBVH(`Model, Scan.Frustum`)` `// see Algorithm 23 in Appendix D`

for each Scan.P_B **do**
  Scan.P_P ← `CalculateAsPlannedPoint(`Scan.P_B,BVH`)` `// see Algorithm 4`
end

Algorithm 3: Procedure *CalculateAsPlannedPointCloud* calculating the as-planned range point cloud corresponding to an as-built range point cloud.

The calculation of each as-planned range point is performed as follows. Consider one as-built range point, P_B. It is defined in spherical coordinates by its pan angle, tilt angle and range, (φ, θ, ρ). Its corresponding as-planned range point, P_P, is first assigned the same pan and tilt angles, φ and θ. Then, its range is calculated by performing the virtual scan in the scanning direction, or *ray*, defined by these two angles and using the scan-referenced 3D model as the virtually scanned world. Since the project 3D model is STL-formatted, its range is thus the distance between the scanner's origin and the closest intersection point of the ray with a STL facet of a 3D model object.

Once the closest intersected STL facet is identified, the as-planned point is not only assigned a range value, but it is also assigned, as an *IDobject* feature, the name or ID of the object to which the intersected STL facet belongs. So, contrary to the real scan, it is known in the virtual scan from which object each as-planned range point is obtained. A point that does not intersect any STL facet of any object is assigned an infinite range and a null *IDobject* feature value.

The complexity of the calculation of each as-planned range point lies in the identification of the closest STL facet intersected by its scanning direction. This problem is discussed further and existing approaches to solving it are reviewed in Section 3.4.1. The developed approach is then detailed in Section 3.4.2.

3.4.1 The Ray Shooting Problem

The identification of the closest model facet intersected by the scanning direction of an as-planned point is a *ray shooting amidst polyhedra* problem [48]. The *ray shooting* problem, and its special case the *ray shooting amidst polyhedra* problem, are intensively investigated problems particularly because of their applications in computer graphics [5].

A distinction can be made between the *on-line ray shooting* and the *off-line ray shooting* problems [48]. In off-line ray shooting problems, all the rays are known simultaneously. In on-line ray shooting problems, however, rays are known one at a time — the processing of one ray must be completed prior to starting the processing of the next. This leads to differently designed solutions for both types of problems. The problem investigated here is clearly an off-line ray shooting problem.

The calculation of the as-planned range point cloud, presents another characteristic, shared with most commonly investigated off-line ray shooting problems, which is that all the rays have a single source point [48]. Solutions to this problem have many applications in particular in computer graphics for 3D scene rendering.

In the rest of this section, different techniques used to solve the ray shooting problem are presented. The term "object" refers to a simple primitive form such as spheres and basic polygons. In the investigated as-planned range point cloud calculation problem, it corresponds to a STL triangular facet.

The brute force solution to the *off-line ray shooting with single source* problem consists in investigating the intersection of each ray with each object to deduce the closest intersected ray by each facet. This would be very inefficient — particularly in the investigated problem as range point clouds may consist of millions of points and project 3D models, once converted into STL format, may consist of thousands of facets. In order to accelerate ray shooting solutions, four main strategies may be implemented either separately or complementarily: *ray partitioning* and *shooting bounding volumes*, *space partitioning* and *culling* [45]. These four strategies are reviewed in the four sections below. The section *Conclusion* analyzes the applicability of all these techniques to the investigated calculation of as-planned range point clouds.

Rays Partitioning

Ray partitioning aims at exploiting the coherence between spatially adjacent rays. Indeed, rays with the same source and almost the same direction are likely to intersect the same object with a similar intersection point. Different strategies have thus been developed to group rays into beams [15, 56, 98], cones [11] pencils [105] or ray bounds [90].

Assarsson and Möller [16] particularly apply viewing frustum culling techniques (see description in Section *Culling Techniques*) to beams of rays in order to rapidly reduce the number of objects that may be intersected by any of the rays constituting the beam. This technique presents some limitations noted by Reshetov et al. [98] who present an improved version. In essence, these two techniques aim at identifying lower entry nodes in space partitioning trees (see section below) for entire groups of rays, thus reducing the overall complexity. Note that these two techniques perform their technique of "beam frustum culling" using axis-aligned bounding boxes (see Section *Shooting Bounding Volumes*).

Shooting Bounding Volumes

Bounding Volumes (BVs) are often used to rapidly test whether a ray may intersect a given object. Indeed, an object cannot be intersected by a ray if a volume bounding it is not itself intersected by the ray. Strategies are thus implemented that aim at computing for each search object a simple bounding volume so that, for the calculation of each ray, a sub-set of objects that may potentially be intersected by the ray can be identified rapidly.

Spheres and axis-aligned bounding boxes and oriented bounding boxes are commonly used bounding volumes [125]. But, more complex bounding volumes have also been analyzed, for instance by Kay and Kajiya [66]. In general, the choice of a bounding volume is the result of a trade-off between the ease of intersection testing and the reduction in the number of intersection testing it enables (or "tightness"), and thus results on specificities of the given problem [125]. Weghorst et al. [125] studied this trade-off for different types of bounding volumes.

Space Partitioning And Bounding Volume Hierarchies

Space partitioning aims at dividing the space into regions, sub-regions and so on until each leaf region contains only a small number of objects. Then, for the calculation of each ray, the resulting partition tree is walked in a top-down manner and only the objects contained in the leaf regions that are intersected by the ray

are tested for intersection with the ray. In order to significantly improve the performance of the calculations for each ray, it is important that the calculation for testing whether the ray intersects a region be very simple.

Space partitioning data structures, that have been investigated and successfully applied include uniform grids, octrees, binary space partitioning (BSP) trees, kd-trees, and bounding volume hierarchies (BVHs) [45].

As presented in the two sub-sections below, space partitioning data structures may be constructed in different manners and present different properties. However, for the calculation of all the rays at run-time, they are walked in a similar top-down manner [103]. At each node of the space partition tree, starting at its root, a simple test is conducted with the parameters of the ray and of the regions defined by the first partition so that it can be determined whether the ray intersects one or more of the sub-regions defined by this partition. Similar tests are recursively conducted with the intersected regions and so on until the regions are all leafs of tree. The result is that only the objects contained in the intersected leaf regions are investigated for potential intersection with the ray. The closest intersected object is the solution to the ray shooting problem for this one ray. The process is then repeated with all remaining rays — note that ray partitioning techniques presented in the previous section actually aim at not repeating for all rays the entire process from the root of the tree.

Uniform grids, Octrees, BSP trees and kd-trees:

Uniform grids, octrees, BSP trees and kd-trees partition the space by subdividing it, and have the specificity that the resulting regions do not overlap (only at edges).

Although these four structures are built by dividing the space in different ways, their construction typically follows the same procedure. The entire space is first considered. Then, a first partition is identified that divides the entire space in two or more regions. Each of these regions contains a certain number of objects. Objects intersecting two or more regions may either be considered as part of all of them, or be split so that each resulting object is inside one region only. The process is repeated with each sub-region until a termination criterion is reached — typically if the number of objects contained the region is less than a pre-defined number.

Uniform grids are built by subdividing the entire space in a uniform grid of cubes. Octrees are built by subdividing each space, or region, into eight cubes. BSP trees are built by subdividing each space, or region, using planes (hyperplanes) that can be oriented in any direction. Finally, kd-trees are a special case of BSP trees where the splitting planes are perpendicular to the coordinate system axes.

One main application of of these data structures (as well as BVHs) is in accelerating ray tracing algorithms for CAD rendering applications. For example, Knoll et al. [72] and Brönnimann and Glisse [23] present ray tracing algorithms using octrees, Wald et al. [123] an algorithm using a BSP tree, and Reshetov et al. [98] and Havran and Bittner [54] algorithms using kd-trees.

A particularly interesting work is presented by Keeler et al. [67] who construct a true *spherical visibility map* of scenes made of triangular facets. This spherical visibility map is stored in a BSP tree which can thus be used for speeding up ray shooting solutions. Additionally, this technique simultaneously achieves the culling of hidden surfaces, another accelerating technique described in more detail in the section *Culling Techniques* below. Note, however, that contrary to the other space partitioning data structures presented above, this spherical visibility map partitions the space based on the viewer's location, or ray source. As a result, it must be recomputed for every ray source. In contrast, uniform grids, octrees, BSP trees and kd-trees are all viewer-independent and thus only have to be computed once.

Bounding Volume Hierarchies (BVHs):

Bounding Volume Hierarchies (BVHs) are an extension of using Bounding Volumes (BVs) presented in Section *Shooting Bounding Volumes* above. BVHs partition the space and are constructed from the bottom up and have the specificity that bounding volumes may overlap [47].

BVHs are constructed as follows: (1) the BVs of all objects are calculated and considered as the leafs of the hierarchy; and then (2) the BVs are aggregated using a pre-defined closeness criterion, and the process typically stops until all the BVs are aggregated in a single BV, which consequently bounds all the objects in the scene [47].

As described in Section *Shooting Bounding Volumes* above, spheres and axis-aligned bounding boxes and oriented bounding boxes are commonly used BVs [125].

In a BVH, each parent node may have any number of children nodes. BVHs may thus be more convenient in some situations than uniform grids, octrees, BSP trees or kd-trees that can only split a space in a pre-defined number of regions. Additionally, BVHs can be rapidly updated in the case of dynamic scenes. They are thus very popular for implementing collision detection applications, such as in video games [121].

The effectiveness of BVHs in the searching process is dependent on the trade-off achieved by the BVs between (1) ease of intersection testing and (2) reduction in the number of intersection testing (tightness) they enable [125]. Therefore, the

effectiveness of a BVH is very dependent on the characteristics of the investigated problem.

Examples of ray shooting algorithms using BVHs can be found in [33, 47, 121, 125].

Culling Techniques

While space partitioning data structures enable faster identification of the closest facet intersected by a ray, other techniques, referred to as *culling techniques*, can be used complementarily to reduce the number of objects that actually need to be including in them, and consequently reduce the time necessary to walk them for the calculation of each ray. These techniques mainly include [6]:

Viewing frustum culling: The viewing frustum is a geometric representation of the volume in which facets may potentially be intersected by the rays. Facets outside this volume cannot be intersected by any ray, so they are discarded. If an object lies over a border, it is either kept entirely or spliy along this boundary in a process called clipping, and the pieces that lie outside the frustum are discarded.

Back-face culling: Rays cannot intersect a back-facing object, so all back-facing objects can be discarded from space data structures. Back-facing objects can easily be identified in the case where objects are oriented polygons.

Occlusion culling: Objects may lie entirely behind other objects, in which case they are said to be *occluded*. Since the closest intersection of a ray with an object is necessarily with a non-occluding object, occluded objects can be discarded from space data structures.

The problem of occlusion culling has been intensely studied, and is more generally referred to as the *hidden surface removal* problem. Many hidden surface removal techniques have been developed [37, 49, 70, 83], but they are either efficient, but so intricate that no attempt to implement them has yet been reported, or practical, but not robust enough for practical reliable application [67]. However, Keeler et al. [67] recently presented a new technique for efficiently and reliably constructing *spherical visibility maps* of scenes made of triangular facets. A spherical visibility map is organized in a BSP tree and the authors demonstrate its applicability to the rendering problem with only primary rays (no reflections or refractions are considered).

Conclusion

This section provided a general overview of techniques for solving the off-line ray shooting with single source problem. Many of these techniques would be applicable to the investigated calculation of as-planned range point clouds.

Space partitioning techniques could be applied to reduce the number of STL facets that would need to be investigated to identify the closest one intersected by the scanning direction (ray) of each as-planned point. Ray partitioning techniques, in particular beam tracing techniques, could be applied for further reducing the complexity. Finally, culling technique could certainly be applied, in particular back-face culling since STL facets are oriented.

In the next section, an approach is thus presented that efficiently and accurately calculates as-planned range point clouds. It uses a 3D model's BVH as well as back-facing and viewing frustum culling techniques. This approach enables accurate calculation of the range of any as-planned point in any scene. It will be shown in Chapter 4 that the performance, in particular efficiency, of the overall object recognition approach is mainly due to the performance of this as-planned range point cloud calculation technique.

3.4.2 Developed Approach

The proposed approach to calculate as-planned range point clouds uses a Bounding Volume Hierarchy (BVH) to efficiently organize the 3D model data. The particularity here is that the hierarchy uses a novel bounding volume referred to as the *Minimum Spherical Angular Bounding volume*, or MSABV. The MSABV, illustrated for one facet in Figure 3.1, is defined by the four pan and tilt angles bounding a facet, or group of facets, in the scan's spherical coordinate frame. It is however open (no limit in range). The detailed calculation of the MSABV of STL entities (facets and objects) is presented in Appendix C.

The MSABV of a group of facets is the union of the MSABVs of these facets. Therefore, MSABVs can be aggregated in a BVH. The proposed BVH is constructed by aggregating the MSABVs of all the facets of each STL object into one MSABV for each object, and finally by aggregating the MSABVs of all the objects of the project 3D model into one MSABV for the entire project 3D model. The proposed BVH thus has three levels as illustrated in Figure 3.2. The detailed calculation of the BVH of the project 3D model is presented in Appendix D. Appendix D particularly describes how the size of the BVH can be significantly reduced by performing *scan's viewing frustum culling* and *back-facing culling*.

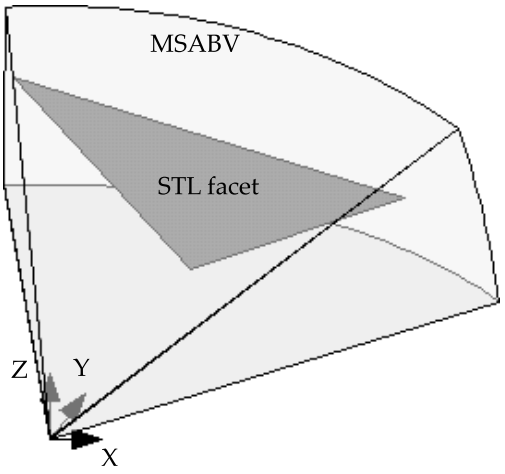

(a) 3D View.

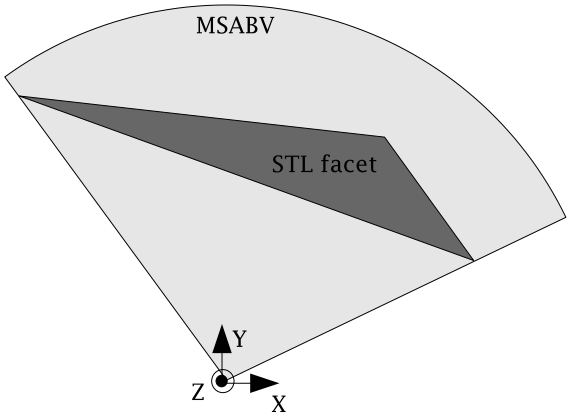

(b) Top View.

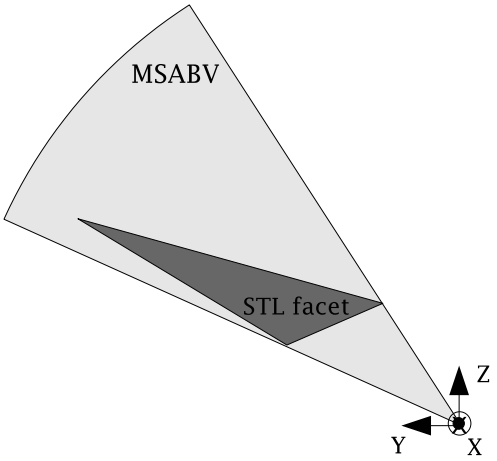

(c) Side View: Projection of the facet and MSABV by rotation around the z axis on one quadrant of the (YZ) plane.

Figure 3.1: Illustration of the MSABV (minimum spherical angular bounding volume) of a STL facet in the scan's spherical coordinate frame.

Then, as expected for any bounding volumes, a ray may intersect a STL facet (respectively object or model) only if it is itself contained inside the MSABV of the facet (respectively object or model). The calculations to test whether the scanning direction of an as-planned point is contained inside a MSABV are detailed in Appendix E.

This test is simpler to implement than the intersection test between a ray and a bounding box, but not necessarily simpler than with spheres. However, it will be shown in Chapter 4 that MSABVs are a tighter bounding volumes than spheres, enabling faster as-planned point cloud calculation for large point clouds.

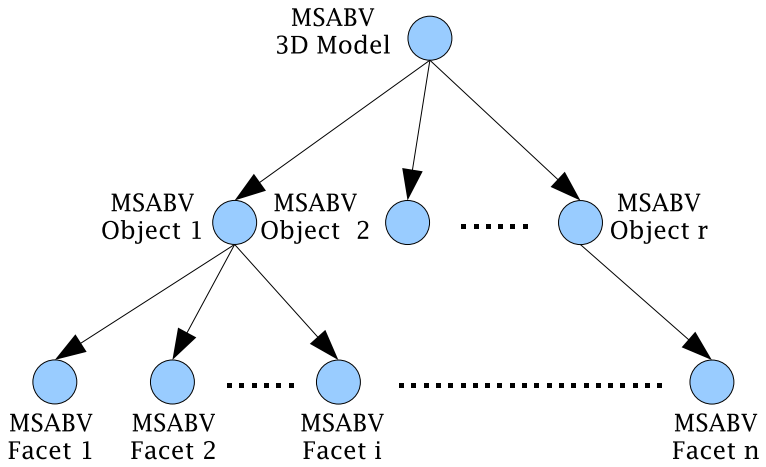

Figure 3.2: Illustration of the structure of the chosen BVH for project 3D model where bounding volumes are MSABVs.

Finally, for the calculation of the range of each as-planned point, the identification of the facets that can potentially intersect the scanning direction, or ray, of the as-planned point is performed by walking the BVH of the project 3D model in a top-down manner and testing only the intersection with the facets for which the ray intersects the MSABV. The calculation of the range of the intersection point of a ray with a facet, if it actually exists (the intersection with the MSABV does not ensure intersection with the facet), is detailed in Appendix F. The returned range is infinite if the intersection does not exist.

The overall algorithmic implementation of the calculation of each as-planned range point is presented in Algorithm 4. Note that, Algorithm 4 includes, at its end, the calculation of another as-planned point feature than its range, $Surf$, which is the *as-planned point covered surface*. The need for calculating this value and the description of its calculation, requiring the scan's pan and tilt resolutions (Res_φ and Res_θ), will be presented in Section 3.6.

3.5 Step 4 - Range Points Recognition

The as-planned range point cloud is calculated so that each as-planned range point corresponds to exactly one as-built range point (same scanning direction (φ, θ)). The recognition of each as-planned range point can thus be inferred by comparing it with its corresponding as-built range point. This requires a *point recognition metric* defined here.

Consider one pair of as-planned and corresponding as-built range points. They

```
Data: P_B, BVH
Result: P_P

Assign values to P_P.φ and P_P.θ.
P_P.φ ← P_B.φ
P_P.θ ← P_B.θ

Calculate P_P.ρ and other properties of P_P.
P_P.ρ ← ∞
P_P.IDobj ← NaN
for each BVH.Object do
    if IsRayInMSABV(P_P, BVH.Object.MSABV) = True then
                                              // see Algorithm 24 in Appendix E
        for each BVH.Object.Facet do
            if IsRayInMSABV(P_P, BVH.Object.Facet.MSABV) = True then
                                          // see Algorithm 24 in Appendix E ρ' ←
                CalculateIntersectionPointRange(BVH.Object.Facet, P_B)
                                              // see Algorithm 25 in Appendix F
                if ρ' < P_P.ρ then
                    P_P.ρ ← ρ'
                    P_P.IDobj ← BVH.Object.ID
                end
            end
        end
    end
end
P_P.(x, y, z) ← SphericalToCartesian(P_P (φ, θ, ρ))          // see Algorithm 10
P_P.Surf ← CalculateCoveredSurface(P_P, Scan.Res_φ, Scan.Res_θ) // see Algorithm 9
```

Algorithm 4: Function *CalculateAsPlannedPoint* calculating the as-planned range point corresponding to an as-built range point.

have the same pan and tilt angles. The point recognition metric can thus only consider their ranges. (Note that, if other point features, such as color or texture, are available for both points, they can certainly be incorporated in the metric). A simple point recognition metric is the comparison of the difference between their ranges, $\Delta\rho$, with a pre-defined threshold, $\Delta\rho_{max}$. If $|\Delta\rho|$ is smaller than or equal to $\Delta\rho_{max}$, then the as-planned range point is considered recognized; it is not recognized otherwise. The algorithmic implementation of this calculation is presented in Algorithm 5.

3.5.1 Automated Estimation of $\Delta\rho_{max}$

In order for the recognition of each point to be robust and performed automatically, $\Delta\rho_{max}$ must be adequately calculated automatically. An adequate value may depend on many characteristics such as:

```
Data: Scan.(P_B, P_P), Δρ_max

Δρ ← Scan.P_P.ρ − Scan.P_B.ρ
if |Δρ| ≤ Δρ_max then
 |  Scan.P_P.IsRecognized ← True
else
 |  Scan.P_P.IsRecognized ← False
end
```

Algorithm 5: Procedure *RecognizePoint* matching an as-planned range point to its corresponding as-built range point.

Point range measurement uncertainty: Range measurement uncertainty due to technology limitations is normally provided by laser scanner providers, though in very specific conditions (material reflectivity, with scanning directions perpendicular to the scanned surface, *etc*). Range measurement uncertainty generally increases with the measured range. For instance, in the case of the scanner used in this research, the provided range measurement uncertainty are: $1.5mm$ at $50m$ and $7mm$ at $50m$ for 100% reflective targets positioned perpendicularly to the scanning direction. It would therefore be appropriate to customize the threshold $\Delta\rho_{max}$ with the range of each as-planned point, $P_P.\rho$, in order to take this uncertainty into account:

$$\Delta\rho_{max} = f_1\left(P_P.\rho\right)$$

Point pan and tilt angles uncertainties: Pan and tilt angle measurement uncertainties result from imperfections of the pan&tilt unit embedded in the laser scanner. They are independent from the scanned point, and are generally provided by laser scanner providers. For instance, in the case of the scanner used in this research, pan and tilt uncertainties are respectively $60\mu rad$ and $70\mu rad$ ($0°0'12''$ and $0°0'14''$). These respectively translate into $0.6mm$ and $0.7mm$ precision at $10m$, or $6mm$ and $7mm$ precision at $100m$. The impact of pan and tilt uncertainties on the as-planned point range measurement is that the as-planned point range may be assigned to an incorrect direction. Methods using point neighborhood analysis can be used for dealing with such uncertainties. The calculation of the threshold $\Delta\rho_{max}$ could thus be further customized with the pan and tilt uncertainties, u_φ and u_θ, and each as-planned range point scanning direction defined by $P_P.\varphi$ and $P_P.\theta$:

$$\Delta\rho_{max} = f_1\left(P_P.\left(\rho,\varphi,\theta\right),\left(u_\varphi,u_\theta\right)\right)$$

Point reflection angle: Uncertainty in range acquisition also increases with the reflection angle between the scanning direction and the scanned surface normal vector (see illustration in Figure 3.3). If the as-planned reflection angle,

α, of each as-planned range point, P_P can be estimated when calculating its range, it could then be used to further customize the $\Delta\rho_{max}$ threshold:

$$\Delta\rho_{max} = f_1\left(P_P.\left(\rho, \varphi, \theta, \alpha\right), \left(u_\varphi, u_\theta\right)\right)$$

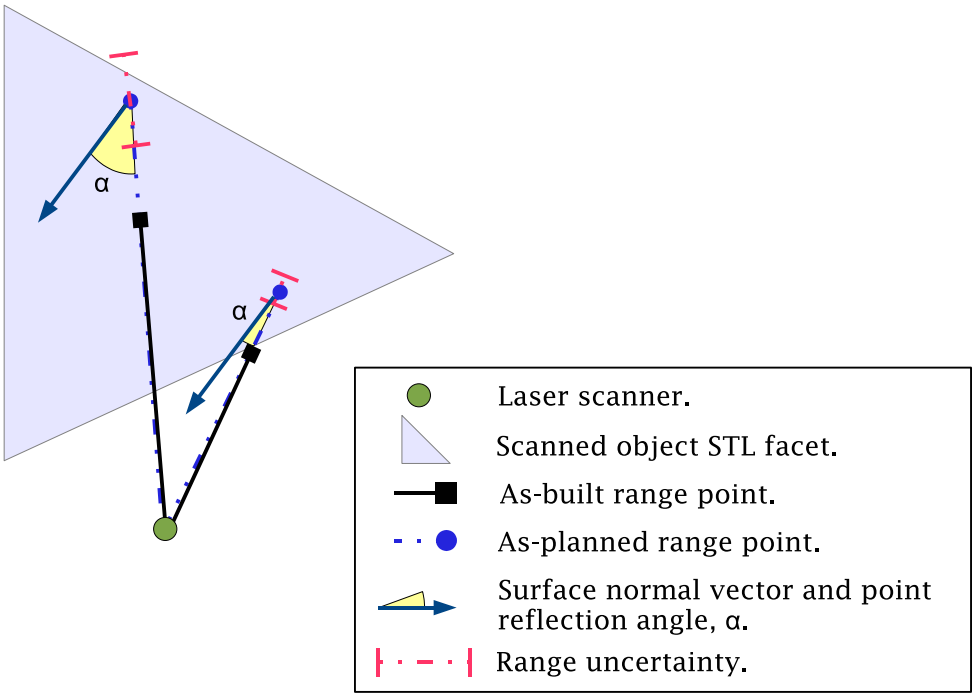

Figure 3.3: Impact of the reflection angle on the range measurement uncertainty.

Scanned Surface reflectivity: Range measurement uncertainty also decreases with the reflectivity of the surface it is acquired from. Thus, similarly as above, if the surface reflectivity, λ, can be obtained when calculating each as-planned range point, P_P, the threshold $\Delta\rho_{max}$ could then be further customized:

$$\Delta\rho_{max} = f_1\left(P_P.\left(\rho, \varphi, \theta, \alpha, \lambda\right), \left(u_\varphi, u_\theta\right)\right)$$

Registration error: Errors in scan registration lead to errors in model-to-scan referencing and thus may significantly affect object recognition results. Here, registration is performed using tie points (at least three non-aligned points), and it has been shown in Section 3.3 that it is possible to automatically obtain some registration error information, such as the *mean registration error*, $\overline{\epsilon_{Reg}}$, at the end of the registration process. The mean registration error, $\overline{\epsilon_{Reg}}$, could be used to adjust $\Delta\rho_{max}$, as larger $\Delta\rho_{max}$ values should be used with larger $\overline{\epsilon_{Reg}}$ values:

$$\Delta\rho_{max} = f_1\left(P_P.\left(\rho, \varphi, \theta, \alpha, \lambda\right), \left(u_\varphi, u_\theta\right), \overline{\epsilon_{Reg}}\right)$$

Construction error: During construction, crews do their best to build elements at their intended location. However, there is always some location error that may thus impact the matching of as-built and as-planned range points. An upper for such errors, ϵ_{Const}, could thus be used to adjust $\Delta\rho_{max}$:

$$\Delta\rho_{max} = f_1\left(P_P.\left(\rho, \varphi, \theta, \alpha, \lambda\right), \left(u_\varphi, u_\theta\right), \overline{\epsilon_{Reg}}, \epsilon_{Const}\right)$$

By taking all these scan and point characteristics into account, it would be possible to automatically estimate an adequate value of $\Delta\rho_{max}$ for each as-planned range point. However, this would require the estimation of the relations between $\Delta\rho_{max}$ and the different parameters mentioned above ($P_P.\left(\rho, \varphi, \theta, \alpha, \lambda\right)$, $\left(u_\varphi, u_\theta\right)$, $\overline{\epsilon_{Reg}}$, and ϵ_{Const}), in other words of the function $f_1\left(\right)$, *a priori*. For this, multiple experiments with complex setups would have to be conducted, which was completely out of the scope of this research. Thus, a simpler $\Delta\rho_{max}$ threshold estimation is used at this point. Only two criteria are retained for setting this value: for each scan, $\Delta\rho_{max}$ is set equal to the sum of the mean registration error $\overline{\epsilon_{Reg}}$ and an upper bound for construction error ϵ_{Const} which must thus be defined *a priori* — and a value of $50\,mm$ is chosen because it is larger than generally acceptable (specified) construction location errors, but small enough to avoid false positive point recognitions. In fact, after conducting multiple experiments, these two errors have appeared as probably the most critical sources of error to the proposed approach. The following formula for automatically estimating $\Delta\rho_{max}$ is thus used:

$$\Delta\rho_{max} = \overline{\epsilon_{Reg}} + \epsilon_{Const} \tag{3.3}$$

It will be shown in Chapter 4 that this simple automated estimation of $\Delta\rho_{max}$ leads to good object recognition accuracy performance.

3.6 Step 5 - Objects Recognition

3.6.1 Sort Points

When calculated, each as-planned range point is assigned, as an $IDobj$ feature, the ID of the object from which it is obtained. The as-planned range points can thus be sorted by $IDobj$, so that each model object is assigned an as-planned point cloud. The as-built range points corresponding to as-planned range points with a NaN $IDobj$ value (they also have infinite ranges) are discarded or can be grouped in a new object, *non-model object*. Then, since each as-planned range point corresponds to exactly one as-built range point, each model object is also assigned a corresponding as-built point cloud (regardless of the point recognition results). The algorithmic implementation of this step is presented in Algorithm 6

```
Data: Scan,Model
Result: Model,NonModel

for each Scan.P_P do
    if Scan.P_P.IDobj ≠ NaN then
        ObjectHandle ← GetObjectHandle(Scan.P_P.IDobj)
        ObjectHandle.({(P_P, P_B)}) ← Add(ObjectHandle.({(P_P, P_B)}),
        (Scan.P_P, Scan.P_B))
    else
        NonModel ← Add(NonModel, Scan.P_B)
    end
end
```

Algorithm 6: function *SortPoints* sorting the as-planned and corresponding recognized points by model object.

3.6.2 Recognize Objects

At this point, each model object is assigned an as-planned range point cloud and its corresponding as-built range point cloud. Note that these can be empty, in which case the object is clearly not recognized. In the case these are not empty, an *object recognition metric* must be used.

A basic object recognition metric might consider the number of recognized points and compare it to a pre-defined threshold. The problem with such a metric is the automated estimation of the threshold. Indeed, the further from the scanner an object is, the less points may be obtained from it, so that, with a given scan's angular resolution and a pre-defined threshold, it is possible that an object far enough from the scanner cannot be recognized. This could be avoided by choosing a low threshold value. However, this would result in a higher probability of Type I object recognition errors.

Another approach, that would somewhat avoid this problem, is to infer object recognition based on the as-planned range point cloud recognition rate. Indeed, the number of as-planned range points would vary with the scanner-object distance similarly to the number of recognized points, so that the recognition rate would be invariant with the distance between the scanner and the object and the scan's angular resolution. However, this metric presents a limitation, that the first metric did not have. It is not robust with respect to occlusions due to non-model objects (*external occlusions*). Indeed, an object occluded by other non-model objects would have a low as-planned point cloud recognition rate, potentially lower than a pre-defined threshold, despite possibly many recognized points.

A third metric is preferred. It infers object recognition by calculating the object *recognized surface*, $Surf_R$, and comparing it to a threshold, $Surf_{min}$. If $Surf_R$ is

larger than or equal to $Surf_{min}$, then the object is considered recognized; it is not otherwise. The algorithmic implementation of this object recognition metric is given in Algorithm 7.

```
Data: Model, Surf_min

for each Model.Object do
    Model.Object.Surf_R ← CalculateRecognizedSurface(Model.Object)        // see
    Algorithm 8
    if Model.Object.Surf_R ≥ Surf_min then
        Model.Object.IsRecognized ← True
    else
        Model.Object.IsRecognized ← False
    end
end
```

Algorithm 7: Procedure *RecognizeObject* from as-built and as-planned range point clouds.

For each object, the recognized surface, $Surf_R$, is calculated as the weighted sum of its recognized as-planned points, where each point's weight is its *as-planned covered surface*. The algorithmic implementation of this calculation is given in Algorithm 8.

```
Data: Object
Result: Surf_R

Surf_R ← 0
for each Object.P_B do
    if Object.P_B.IsRecognized = True then
        Surf_R ← Surf_R + Object.P_P.Surf
    end
end
```

Algorithm 8: Function *CalculateRecognizedSurface* calculating the recognized surface of a model object.

The covered surface of an as-planned point, $P_P.Surf$, is illustrated in Figure 3.4. It can be roughly defined as the area delimited by the equidistant boundaries between it and its immediate neighboring points, and is calculated as:

$$P_P.Surf = \frac{Surf_{unit}}{\cos\left(P_P.\alpha_\varphi\right)\,\cos\left(P_P.\alpha_\theta\right)}\;\left(P_P.\rho\right)^2 \tag{3.4}$$

where: α is the as-planned point reflection angle. It is the angle between the point scanning direction and the normal to the STL facet from which it is obtained, and can be decomposed into its pan and tilt components, α_φ and α_θ, as illustrated in Figure 3.5.

$Surf_{unit}$ is the surface (expressed in m^2), covered by a point with range 1 m, perpendicular to the point's scanning direction, given the scan angular resolution, defined by Res_φ and Res_θ. It is calculated with the following equation:

$$Surf_{unit} = \tan(Res_\varphi)\ \tan(Res_\theta) \tag{3.5}$$

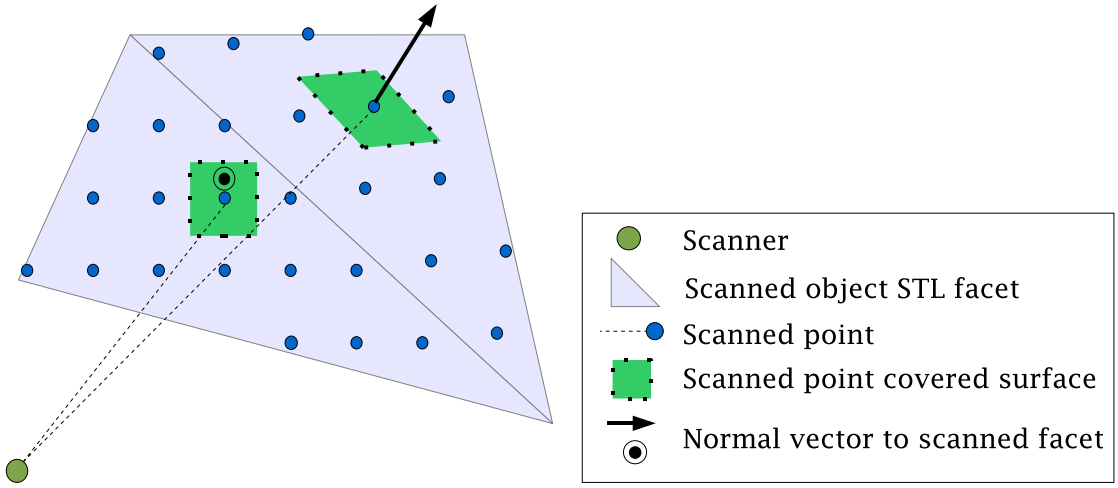

Figure 3.4: Illustration of the as-planned covered surfaces of as-planned range points.

The algorithmic implementation of the calculation of the covered surface of an as-planned range point is presented in Algorithm 9, with notations similar to those used in Figure 3.5. Note that the calculation of the covered surface of an as-planned range point can be performed at the same time as the calculation of its range. For this reason, Algorithm 9 is called by Algorithm 4.

3.6.3 Automated Estimation of $Surf_{min}$

In order to automate this object recognition process, an adequate value of $Surf_{min}$ must be defined automatically. A large value of $Surf_{min}$ would likely increase specificity rates (smaller Type I error rates), but would also decrease recall rates (larger Type II error rates). In contrast, a low value of $Surf_{min}$ would likely increase recall rates, but at the expense of smaller specificity rates.

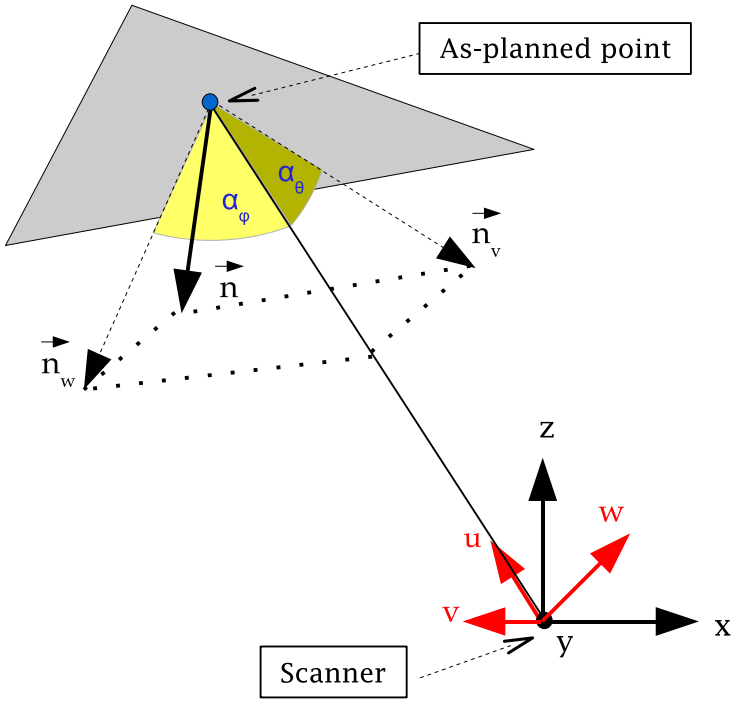

Figure 3.5: Illustration of α_φ and α_θ, the pan and tilt components of the reflection angle, α, of an as-planned point.

Data: P_P, Res_φ, Res_θ
Result: Surf

$\overrightarrow{u} \leftarrow [P_P.x, P_P.y, P_P.z]$
$\overrightarrow{u} \leftarrow \frac{1}{\|\overrightarrow{u}\|}\overrightarrow{u}$
$\overrightarrow{v} \leftarrow \overrightarrow{Z} \times \overrightarrow{u}$
$\overrightarrow{v} \leftarrow \frac{1}{\|\overrightarrow{v}\|}\overrightarrow{v}$
$\overrightarrow{w} \leftarrow \overrightarrow{u} \times \overrightarrow{v}$

Facet $\leftarrow$ `GetFacetHandle(`P_P.IDfacet`)`
Facet.$\overrightarrow{n_w} \leftarrow$ Facet.$\overrightarrow{n}$ - (Facet.$\overrightarrow{n} \cdot \overrightarrow{w}$) $\overrightarrow{w}$
Facet.$\overrightarrow{n_w} \leftarrow \frac{1}{\|\text{Facet}.\overrightarrow{n_w}\|}$ Facet.$\overrightarrow{n_w}$
$P_P.\alpha_\varphi \leftarrow \arccos($-Facet.$\overrightarrow{n_w} \cdot \overrightarrow{u})$

Facet.$\overrightarrow{n_v} \leftarrow$ Facet.$\overrightarrow{n}$ - (Facet.$\overrightarrow{n} \cdot \overrightarrow{v}$) $\overrightarrow{v}$
Facet.$\overrightarrow{n_v} \leftarrow \frac{1}{\|\text{Facet}.\overrightarrow{n_v}\|}$ Facet.$\overrightarrow{n_v}$
$P_P.\alpha_\theta \leftarrow \arccos($-Facet.$\overrightarrow{n_v} \cdot \overrightarrow{u})$

Surf $\leftarrow \frac{\tan(Res_\varphi)\tan(Res_\theta)}{\cos(P_P.\alpha_\varphi)\cos(P_P.\alpha_\theta)} (P_P.\rho)^2$

Algorithm 9: Function *CalculateCoveredSurface* calculating the *covered surface* of an as-planned range point.

Furthermore, the calculation of the object recognized surface, $Surf_R$, is invariant with the scan angular resolution. So, in order for the object recognition metric to remain invariant with this factor, $Surf_{min}$ (expressed in m^2) must be automatically adjusted with it, as transcribed with the formula:

$$Surf_{min} = A \ (Surf_{unit})$$

where: A is constant factor.

This formula can be interpreted as: at a distance of $1m$ from the scanner, at least A points of an object as-planned as-planned range point cloud must be recognized in order for this object to be itself recognized. If A is set too low, then the probability of false positive object recognition increases. Indeed, consider $A = 100$. Then, for an object at distance of $10m$ from the scanner, only 1 point would have to be recognized for its recognized surface, $Surf_R$, to be larger than $Surf_{min}$. However, if A is set too large, then the probability of type II recognition error increases. Indeed, consider $A = 1,000,000$. Then, for an object at distance of $10m$ from the scanner, $10,000$ points would have to be recognized for its recognized surface, $Surf_R$, to be larger than $Surf_{min}$. This further implies that the recognition of objects close to the scanner would be very sensitive to *external occlusions* (*e.g.* equipment, temporary structures).

$Surf_{min}$ is consequently calculated as follows. The largest distance of the 3D model to the scanner, $Model.\rho_{max}$, is calculated. It is the largest range of the STL-formatted 3D model vertices. Then, the value of $Surf_{min}$ is set so that, at the range distance $Model.\rho_{max}$ and with the given scan angular resolution, at least n as-planned range points must be recognized in order for their total covered surface to be larger or equal to $Surf_{min}$. This is transcribed into the formula:

$$Surf_{min} = n \ (Model.\rho_{max})^2 \ Surf_{unit} \tag{3.6}$$

Since no object has any part of it with a range larger than $Model.\rho_{max}$, this threshold achieves ensures that, for any object to be recognized, at least n of its as-planned range points must be recognized for the object to be recognized. As a result, this threshold simultaneously ensures that both a minimum surface and a minimum number of point be recognized. The value of n must be defined *a priori*. A value of $5\,points$ is chosen because it is expected to be sufficiently low for avoiding Type II recognition errors (object failed to be recognized) due to external occlusions, but sufficiently large for avoiding Type I recognition errors (object recognized although not present). The performance of this automated estimation of $Surf_{min}$ will be demonstrated in Chapter 4.

3.7 Sensitivity Analyses

Sensitivity analysis is addressed in chapter 4, with focus on the point and object recognition metrics.

The optimality of the automatically calculated $\Delta\rho_{max}$ and $Surf_{min}$ thresholds is thoroughly investigated. However, as discussed then, the sensitivity analysis results do not report on the optimality of the overall point recognition and object recognition metrics — although a good accuracy performance is demonstrated for the overall developed approach. For instance, the analyses do not cover the potential impact of customizing the $\Delta\rho_{max}$ threshold value for each individual point, for instance based on its planned range and reflection angle. The impact of different values of n, in the calculation of $Surf_{min}$, on the object recognition accuracy performance is not investigated either. And, finally, no experimental results are reported on the potential impact of using soft point recognition and object recognition metrics instead of the hard ones used at this point. These analyses are needed and should be conducted in future work.

Other aspects of the performance of the developed approach are covered in Chapter 4, but sometimes only partially. For instance, the quantitative estimation of the impact of registration error on the accuracy (and robustness) performance of the developed approach would be interesting but is not covered. Then, the efficiency of the developed method for calculating as-planned range point clouds is compared with a method using spheres as bounding volumes, but not with any method using bounding boxes as bounding volumes (the comparison with spheres as bounding volumes is covered), neither with the spherical visibility map method described by Keeler et al. [67]. These comparisons are needed to better demonstrate the efficiency of the developed approach.

Chapter 4

Experimental Analysis of the Approach's Performance

This chapter presents results of experiments conducted with the aim of investigating and demonstrating the performance of the developed approach for automated recognition of 3D model objects in site laser scans, in terms of accuracy, robustness, efficiency, and level of automation.

First of all, Section 4.1 rapidly qualitatively analyzes the level of automation of the developed approach. Then, Section 4.2 presents the data sets used to conduct the experiments demonstrating the accuracy, robustness and efficiency of the approach. Section 4.3 demonstrates the accuracy of the approach in terms of object recognition performance. The performance of the automated estimation of the two thresholds, $\Delta\rho_{max}$ and $Surf_{min}$, is also demonstrated. Then, Section 4.4 analyzes the robustness of the developed approach, particularly with respect to occlusions. The efficiency of the approach, namely its computational complexity, is covered in Section 4.5. Finally, Section 4.6 summarizes the observed performance and compares this performance with the targets estimated in Section 2.4.

4.1 Level of Automation

The level of automation and frequency of each of the five steps constituting the developed object recognition approach are summarized in Table 4.1.

Tbale 4.1 shows that the approach is almost fully automated. The only part that has to be performed manually is the manual matching of the benchmarks in both data sets (model and scan) in the registration step (*Step 2*) This manual process is however fairly simple and can be achieved in a matter of minutes.

Furthermore, *Step 1* only has to be performed once for all scans and *Step 2* only has to be conducted once per scan's location. This means that, in the case several scans are conducted from a given location, *Step 2* does not have to be repeated. In fact, it could be envisioned that scanners be located permanently, or at least for long periods of time, in fixed locations and scans be conducted regularly from these locations. In which case, only *Step 3*, *Step 4* and *Step 5* would have to be repeated for each of these scans, making the recognition process for all but the first scan fully automated.

Table 4.1: Level of automation and frequency of each of the five steps constituting the developed object recognition approach.

Approach's Step	Level of Automation	Frequency
Step 1 - Convert Model to STL format:	Fully automated	One time only
Step 2- Register model in scan:	Partially automated	Once per scanner's location
Step 3- Calculate as-planned scan:	Fully automated	Once per scan
Step 4- Recognize as-planned points:	Fully automated	Once per scan
Step 5- Recognize objects:	Fully automated	Once per scan

4.2 Experimental Data

The remaining analysis of the performance of the developed object recognition approach is performed using real-life data obtained from the construction of a building that is part of a power plant project in downtown Toronto in Ontario, Canada. The building is $60m$ long by $15m$ wide by $9.5m$ high. It has a steel structure, the construction of which is the focus of the conducted experiments. The 3D model contains 612 objects and, once converted into STL format, a total of $19,478$ facets. The as-built data consists of five scans conducted on two different days and from different locations. They were all obtained using the same scanner, a Trimble^{TM} GX 3D scanner, that uses time-of-flight technology. Some of the main characteristics of this scanner are presented in Table 4.2. Characteristics of the five scans are provided in Table 4.3. Note that, in the rest of this chapter, the scans will be referred to by their ID. Figure 4.1 presents a photo, the 3D CAD model, and one colored 3D laser scan of the building steel structure.

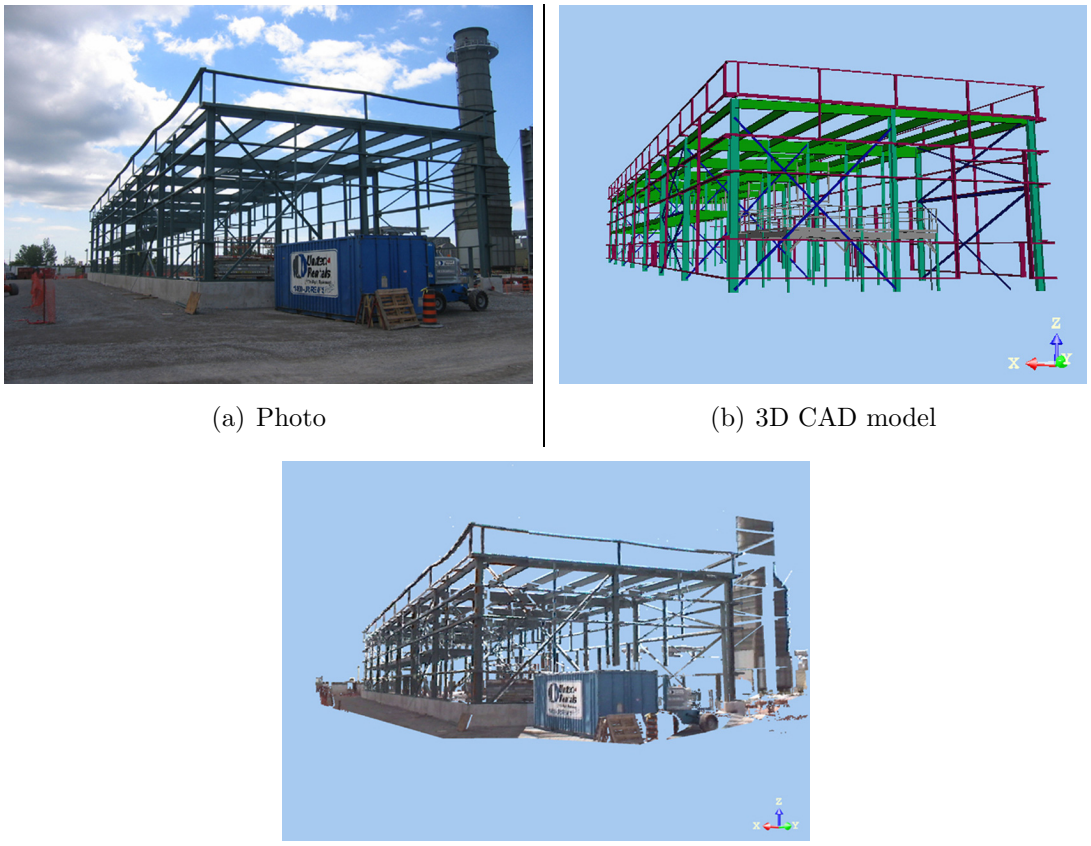

(a) Photo

(b) 3D CAD model

(c) Laser scan

Figure 4.1: (a) Photo, (b) 3D CAD model and (c) laser scan of the steel structure of the investigated PEC project building.

Table 4.2: Characteristics of the Trimble^{TM} GX 3D scanner.

Laser Type		Pulsed; 532nm; green
Distance	Range	2 m to 200 m
	Accuracy	1.5 mm @ 50 m; 7 mm @ 100 m
Angle	Range	Hor: 360°; Vert: 60°
	Accuracy	Hor: 60 μrad; Vert: 70 μrad
Maximum Resolution		Hor: 31 μrad; Vert: 16 μrad
Acquisition Speed		up to 5000 pts/s

4.3 Accuracy

In this section, the accuracy of the developed object recognition approach is investigated. Object recognition accuracy performance metrics are first described in

Table 4.3: Day, Number, ID, number of scanned points, resolution and mean registration error ($\overline{\epsilon_{Reg}}$ with respect to the 3D model) for the five scans.

Scan ID	Day	Number of range points	Resolution (μrad) Hor	Vert	$\overline{\epsilon_{Reg}}$ (mm)
1	1	691,906	582	582	36.86
2	1	723,523	582	582	45.49
3	2	810,399	582	582	29.57
4	2	650,941	582	582	16.26
5	2	134,263	300	300	19.54

Section 4.3.1. Experimental results demonstrating the overall recognition accuracy are then presented in Section 4.3.2. Finally, Sections 4.3.3 and 4.3.4 analyze the performance of the automated estimations of $\Delta\rho_{max}$ and $Surf_{min}$.

4.3.1 Accuracy Performance Metrics

The problem investigated here is an object recognition problem [13]. Fundamental robust metrics object recognition accuracy are the *recall rate* (or *sensitivity rate* or *true positive rate*), the *specificity rate* (or *true negative rate*), the *Type I error rate* (or *false positive rate*), the *Type II error rate* (or *false negative rate*), and the *precision rate*. In the investigated problem, these are defined as follows. The formula below use the notation $n(\{x\})$ for the cardinality of the set $\{x\}$:

Recall: Number of model objects that truly are in the investigated scan and are recognized divided by the total number of model objects that truly are in the investigated scan.

$$\text{Recall Rate} = \frac{n(\{\text{Object in scan}\} \cap \{\text{Object recognized}\})}{n(\{\text{Object in scan}\})}$$

Type II error rate: Number of model objects that truly are in the investigated scan but are not recognized divided by the total number of model objects that truly are in the investigated scan. This is equal to one minus the recall

$$\text{Type II Error Rate} = \frac{n(\{\text{Object in scan}\} \cap \{\text{Object not recognized}\})}{n(\{\text{Object in scan}\})}$$

Specificity (or true negative rate): Number of model objects that truly are not in the investigated scan and are not recognized divided by the total number of model objects that truly are not in the investigated scan.

$$\text{Specificity Rate} = \frac{n(\{\text{Object not in scan}\} \cap \{\text{Object not recognized}\})}{n(\{\text{Object not in scan}\})}$$

Type I error rate: Number of model objects that truly are not in the investigated scan but are recognized divided by the total number of model objects that truly are not in the investigated scan. This is equal to one minus the specificity.

$$\text{Type I Error Rate} = \frac{n\left(\{\text{Object not in scan}\} \cap \{\text{Object recognized}\}\right)}{n\left(\{\text{Object not in scan}\}\right)}$$

Precision: Number of objects that truly are in the investigated scan and are recognized divided by the total number of objects that are recognized.

$$\text{Precision Rate} = \frac{n\left(\{\text{Object in scan}\} \cap \{\text{Object recognized}\}\right)}{n\left(\{\text{Object recognized}\}\right)}$$

The accuracy performance analysis presented in the following two sections focuses on the analysis of the recall, specificity and precision rates only (Type I and II error rates directly relate to the first two).

It must be noted that the calculation of these accuracy performance metrics requires the manual visual identification of which objects truly are present or not in each investigated scan. This identification was conducted and might have resulted in a few errors. Nonetheless, it has been performed conservatively, so that the results are generally biased toward lower performance. Table 4.4 summarizes the number of model objects manually identified in each of the five investigated scans.

Table 4.4: Number of visually identified objects in the investigated five scans.

Scan ID	Number of objects visually identified
1	321
2	286
3	302
4	271
5	38

4.3.2 Experimental Results

Five experiments, *Experiment 1* to *Experiment 5*, are conducted with the scans *Scan 1* to *Scan 5* respectively (Table 4.5). For these experiments, the $\Delta\rho_{max}$ and $Surf_{min}$ values are calculated automatically using the proposed formulae in Equations 3.3 and 3.6 in Chapter 3. For the calculation of $Surf_{min}$, a value of $n = 5$ is chosen.

As discussed in Section 3.6.3, this value is expected to be low enough to prevent false negative recognitions (objects failed to be recognized because less than n of their as-planned range points are recognized), and high enough to prevent false positive recognitions (object recognized when only a couple of their as-planned range points are recognized). The threshold values automatically estimated for the five experiments are listed in Table 4.5. Note that the estimated values of $Surf_{min}$ are equal to about $0.01\,m^2$ which is the surface of a square of side $10\,cm$. Therefore, in these experiments, an object is recognized if the covered surface of its as-planned range points that are recognized is at least as large as the surface of a square of side $10\,cm$.

Table 4.5: Automatically estimated $\Delta\rho_{max}$ and $Surf_{min}$ thresholds for the five experiments.

Experiment	Scan ID	$\Delta\rho_{max}$ (mm)	$Surf_{min}$ (m^2)
1	1	86.86	0.0104
2	2	95.49	0.0118
3	3	79.57	0.0109
4	4	66.26	0.0118
5	5	69.54	0.0031

Appendix G displays, for *Experiment 3*, the data at the different stages of the recognition process, and provides detailed recognition statistics for each of the 612 model objects.

Table 4.6 summarizes the recognition results and performances obtained in the five experiments. It appears that the approach achieves very high specificity and precision rates. This indicates that it rarely recognizes model objects that are not present in the scan. Lower recall rates are however obtained (in average 82%), indicating that the approach fails to recognize some objects that truly are in the scans.

First of all, a more detailed analysis of the results, such as those presented in Figure G.7 and Table G.1 in Appendix G, shows that low recall rates are particularly obtained for small objects such as wall panel braces, while high recall rates are obtained for larger objects such as columns and beams. This is confirmed in Table 4.7.

Table 4.7 presents the same results as in Table 4.6, but with values obtained, not be summing up objects (*e.g.* in *Experiment 1*, 273 objects that are in *Scan 1* are recognized), but by summing up the planned covered surfaces of the objects (*e.g.* in *Experiment 1*, the as-planned covered surfaces of the 273 objects recognized

in *Scan 1* equals $252.71\,m^2$). The results in Table 4.7 thus indicate that the objects that the recognition approach does not recognize but that truly are in the scans are objects for which the covered surfaces of their as-planned range point clouds are small. In fact, further analysis shows that, among the objects that are manually identified but are not recognized in the five experiments, respectively 6 (out of 49), 8 (out of 49), 6 (out of 49), 8 (out of 30) and 2 (out of 8) have as-planned range point clouds with covered surfaces lower than $Surf_{min}$. As a result, it is possible that visible surfaces of those objects in the scan are lower than $Surf_{min}$, in which case these objects maybe should not be counted as false negative recognition errors. If they are not counted, the recall rates for each experiment increases further.

Table 4.6: Object recognition results for the five scans (the values in third and fourth columns are numbers of objects).

Experiment	Objects Recognized	Objects Scanned		Recall	Specificity	Precision
		No	Yes			
1	No	260	49	85%	90%	90%
	Yes	30	273			
2	No	298	49	83%	92%	90%
	Yes	26	239			
3	No	283	49	84%	91%	90%
	Yes	27	253			
4	No	327	60	78%	96%	94%
	Yes	13	212			
5	No	568	8	79%	99%	83%
	Yes	6	30			
all	No	1,736	215	82%	94%	91%
	Yes	102	1,007			

There are different sources of errors that impact at different levels the accuracy performance of the approach. They include:

3D registration error: A significant source of error for this approach is 3D registration error. While $\Delta\rho_{max}$ partially takes this error into account in the recognition of range points, this error may remain significant and still have a considerable impact on the object recognition results.

3D registration error is in fact particularly significant in the data sets used here. Indeed, as shown in Table 4.3, the average mean registration error for

Table 4.7: Object recognition results for the five scans (the values in third and fourth columns are as-planned (expected) covered surfaces in m^2).

Experiment	Objects Recognized	Objects Scanned		Recall	Specificity	Precision
		No	Yes			
1	No	12.25	13.12	95%	59%	97%
	Yes	8.65	252.71			
2	No	21.13	7.49	97%	77%	97%
	Yes	6.33	241.53			
3	No	17.43	20.01	93%	66%	97%
	Yes	9.02	256.78			
4	No	30.51	20.97	91%	94%	99%
	Yes	2.1	209.44			
5	No	0.57	0.34	97%	64%	97%
	Yes	0.31	11.23			
all	No	81.88	61.93	94%	76%	97%
	Yes	26.42	971.7			

the five scans with the 3D model is roughly equal to 30 mm. The reason for these high mean registration error values is that facility tie points were not acquired when these five scans were conducted. Instead, manual point matching had to be used, which typically leads to lower registration quality (and reliability). In the industry, tie-point -based scan registration error specifications are very stringent with values of a few millimeters at most [117]. With mean registration errors of a couple of millimeters, it is expected that the recognition results presented here would demonstrate better accuracy performance, starting with higher recall rates.

Construction error: The second most significant source of error is construction error. Here as well, while $\Delta\rho_{max}$ partially takes this error into account in the recognition of range points, this error may remain significant and still have a considerable impact on the object recognition results.

Thresholds values: Although the recognition results summarized in Tables 4.6 and 4.7 are fairly good, it could be argued, at this point, that these results could have been better if the thresholds, $\Delta\rho_{max}$ and $Surf_{min}$, had different values. The performance of the methods proposed for the automated estimations of these thresholds is actually analyzed in more detail in Sections 4.3.3 and 4.3.4, respectively.

Schedule Error: Another source of error that has not been mentioned yet is referred to as *schedule error*. Indeed, the performance of the proposed approach is expected to be optimal when the 3D as-built facility is scanned in a state similar to the matched 3D model, because internal occlusions most likely match then. In the five experiments conducted here, the entire project 3D model is used to perform the object recognition. Since the states in which the project was scanned during the five scans included most of the model objects, the negative impact of recognizing a full model in a scan of a partially built project did not occur obviously. Indeed, in such a situation, the comparison of the real scan and the as-planned scan may lead to inappropriate recognition results and thus may impact the recognition accuracy. In particular, if the 3D model contains additional objects from those actually present, then the presence of these objects prevents the recognition of the model objects they occlude in the model but are present in the scan.

The solution to this problem is to use a *project 4D model* that better reflects the actual status of the scanned facility at the time of the scan. A project 4D model is obtained by combining information from the project 3D model and the project schedule. The use of project 4D models with the developed approach is further discussed in Section 5.2.3. Furthermore, it is discussed in Chapter 5 how the developed approach can be used to track progress and thus update the project schedule, and consequently 4D model automatically.

4.3.3 Automated Estimation of $\Delta\rho_{max}$

In this section, we investigate the performance of the proposed method for the automated estimation of the threshold $\Delta\rho_{max}$. It is proposed in Section 3.5.1 that the value of $\Delta\rho_{max}$ be automatically estimated using Equation 3.3. It has been shown, in the analysis of the overall recognition accuracy, that the automated estimations of $\Delta\rho_{max}$ (and $Surf_{min}$) generally lead to good recognition results. However, it is investigated here whether other values of $\Delta\rho_{max}$ could have led to even better recognition performances.

Figure 4.2 shows for each of the five experiments presented earlier, the scan mean registration error $\overline{\epsilon_{Reg}}$, the automatically estimated value of $\Delta\rho_{max}$ and the recognition performances for other $\Delta\rho_{max}$ values. In these experiments, the results are obtained with the automatically estimated values of $Surf_{min}$ presented in Table 4.5 (it will be shown in the next section that values of $Surf_{min}$ estimated with this automated method are appropriate).

The results in Figure 4.2 show that, in any of the experiment, for values of $\Delta\rho_{max}$ lower than $\overline{\epsilon_{Reg}}$, the recall rate is very low, although the precision and specificity

rates are very high. In contrast, for values of $\Delta\rho_{max}$ higher than $\overline{\epsilon_{Reg}}$, the recall rate is much higher with not significantly lower precision and specificity rates. Therefore, using $\overline{\epsilon_{Reg}}$ as a minimum for the $\Delta\rho_{max}$ value appears appropriate. The value of ϵ_{Const} of $50\,mm$ also appears adequate in general, although a lower value might be preferred depending on the user's expectations in terms of construction error.

In conclusion, the proposed method for automatically estimating $\Delta\rho_{mmax}$ performs well with good trade-offs between high recall rates on one side and high sensitivity and precision rates on the other. Nonetheless, a more thorough sensitivity analysis could be conducted to better estimate optimal values for $\Delta\rho_{max}$. More complex methods to automatically estimate $\Delta\rho_{max}$ could also be investigated. For instance, it would be interesting to investigate customizing the value of $\Delta\rho_{max}$ for each range point as a function of, for instance, its planned range and reflection angle on the surface it is expected (as-planned) to be obtained from. Additionally, a soft recognition decision criterion could be investigated instead of the hard one used at this point.

4.3.4 Automated Estimation of $Surf_{min}$

In this section, we investigate the performance of the proposed method for the automated estimation of the threshold $Surf_{min}$. It is proposed in Section 3.6.3 to automatically set $Surf_{min}$ using Equation 3.6 with a value of n equal to 5. It has been shown in the analysis of the overall recognition accuracy that the automated estimations of $Surf_{min}$ (and $\Delta\rho_{max}$) generally lead to good recognition results. However, it is investigated here whether other values of $Surf_{min}$ could have led to even better recognition performances.

Figure 4.3 shows for each of the five experiments presented above, the automatically estimated $Surf_{min}$ value and the object recognition performances for other values of $Surf_{min}$ (note the logarithmic scale of the x axis). In these experiments, the results are obtained with the automatically estimated values of $\Delta\rho_{max}$ presented in Table 4.5 (it has been shown in the previous section that values of $\Delta\rho_{max}$ estimated with this automated method are appropriate).

The results in Figure 4.3 show that, in any experiment, for values of $Surf_{min}$ higher than the automatically calculated one, the recall rate is very low, although the precision and specificity rates are very high. In contrast, for values of $Surf_{min}$ lower than the automatically calculated one, the recall rate is much higher with not significantly lower precision and specificity rates.

In conclusion, the proposed method for the automated estimation of $Surf_{min}$ performs well with good trade-offs between high recall rates on one side and high sensitivity and precision rates on the other. Nonetheless, it would be of interest to

conduct a more detailed sensitivity analysis. In particular, the impact of different values of n on the accuracy performance of the approach would be needed. Additionally, similarly to the $\Delta\rho_{max}$, it would be interesting to investigate the use of a soft decision criterion for the recognition of objects, instead of the hard criterion used at this point. Other methods to automatically estimate $Surf_{min}$ could also be explored.

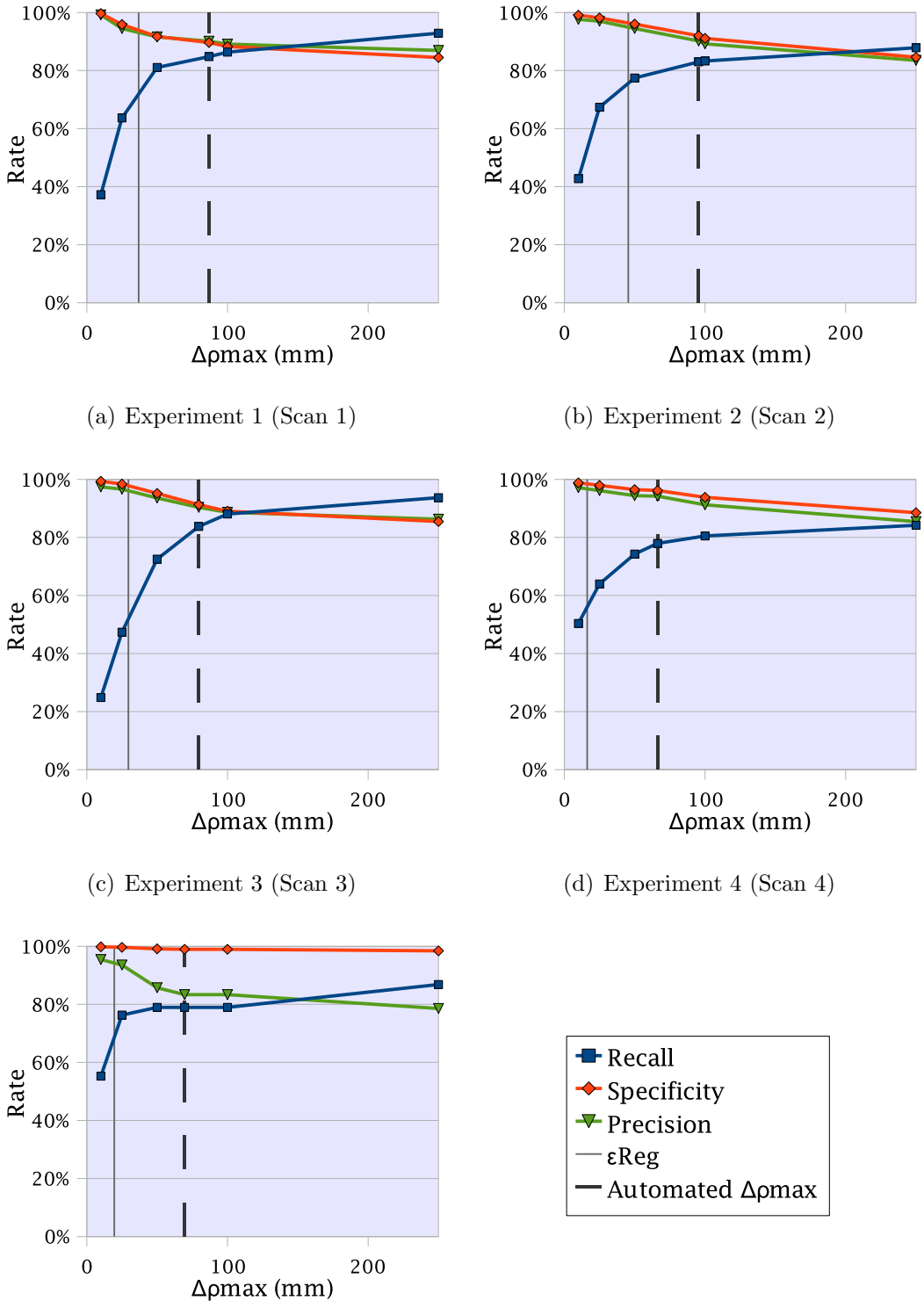

(a) Experiment 1 (Scan 1)

(b) Experiment 2 (Scan 2)

(c) Experiment 3 (Scan 3)

(d) Experiment 4 (Scan 4)

(e) Experiment 5 (Scan 5)

Figure 4.2: Mean registration error $\overline{\epsilon_{Reg}}$, Automatically calculated $\Delta\rho_{max}$ and performances for different values of $\Delta\rho_{max}$.

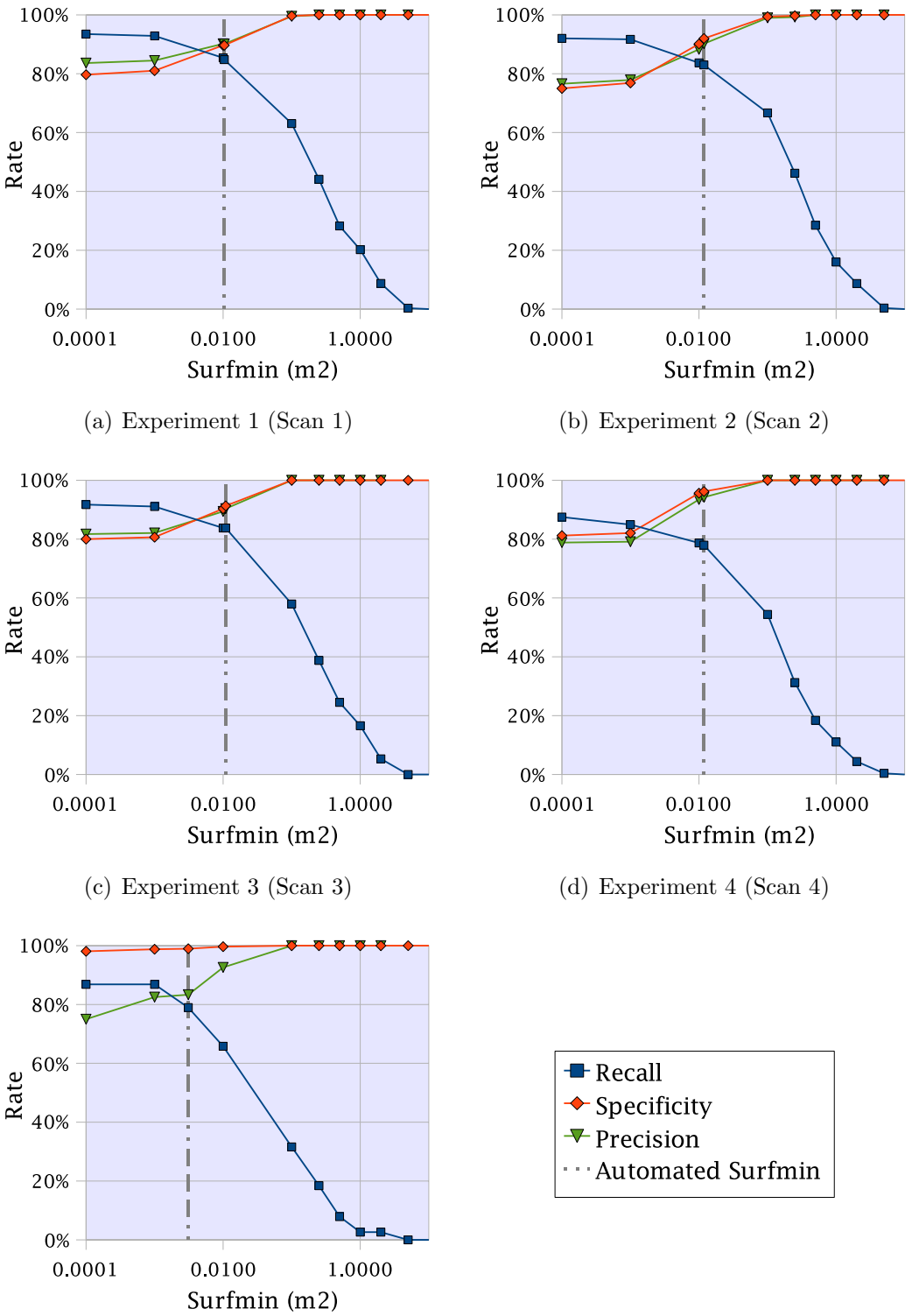

(a) Experiment 1 (Scan 1)

(b) Experiment 2 (Scan 2)

(c) Experiment 3 (Scan 3)

(d) Experiment 4 (Scan 4)

(e) Experiment 5 (Scan 5)

Figure 4.3: Performance for different values of $Surf_{min}$, and automatically estimated value of $Surf_{min}$.

4.4 Robustness

In this section, the performance of the developed object recognition approach is tested with respect to occlusions. This is done by analyzing the accuracy performance presented in Section 4.3 for different *object occlusion rates*.

The difficulty of such an analysis lies in the estimation of the occlusion rate of 3D model objects in a given scene. Results for two types of occlusion rates are presented here. First, Section 4.4.1 analyzes the accuracy performance with respect to the *planned internal occlusion rate (PIOR)*. This rate is a lower bound of the true total occlusion rate but can be reliably estimated. Then, Section 4.4.2 analyzes the accuracy performance with a crude estimation of the *total occlusion rates (TORs)* of objects.

4.4.1 Planned Internal Occlusion Rate

In the developed approach, it is possible to compute the *planned internal occlusion rate (PIOR)* of an object, as the ratio of its as-planned covered surface, calculated by summing the covered surfaces of its as-planned range points, and its visible surface without occlusion, estimated by summing up the surfaces of its front-facing STL facets:

$$\text{PIOR} = 1 - \frac{\text{As-planned Covered Surface}}{\text{Visible Surface Without Occlusion}}$$

The PIOR is an estimated lower bound of the total occlusion rate since it considers planned internal occlusions, but not external ones. Additionally, visible facets may sometimes occlude each other, so that the visible surface without occlusion calculated by summing the surfaces of front-facing facets is an upper bound of the true visible surface without occlusion. In any case, the analysis of the accuracy performance for different PIORs should give an idea of the robustness of the developed approach with occlusions.

Figure 4.4 shows the recall rates and numbers of recognized objects for different object PIORs. It first appears that recall rates tend to decrease with the PIOR, particularly for PIORs above 75%. This may be interpreted as a somewhat limited robustness with occlusions. However, it can also be seen in Figure 4.4 that many objects with internal occlusions rates of at least 85% are successfully recognized. A little bit more that forty objects with occlusion rates of 95% and above are even successfully recognized in the five experiments. This better demonstrates the capacity of the approach to recognize highly occluded objects. Furthermore, it must be reminded that PIORs are only lower bounds of total occlusion rates.

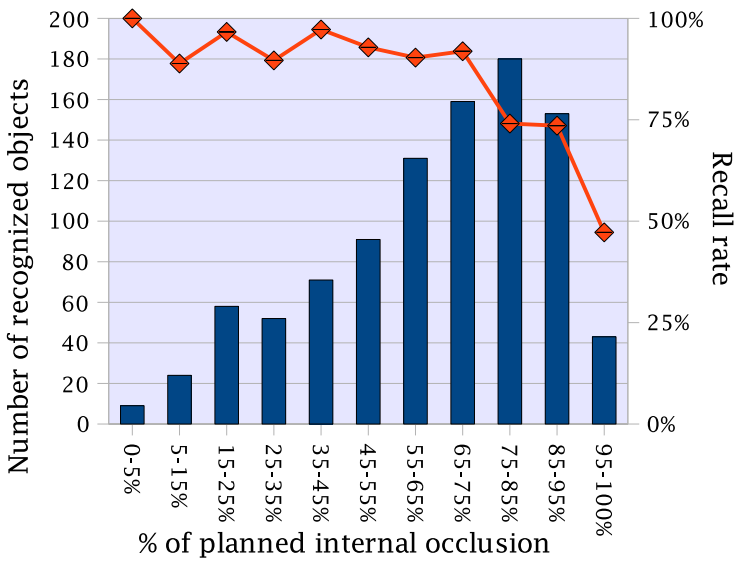

Figure 4.4: Recall rates for different levels of planned internal occlusions.

4.4.2 Total Occlusion Rate (TOR)

The *total occlusion rate (TOR)* of an object can be estimated as the ratio of the recognized as-planned covered surface of an object, calculated by summing up the covered surfaces of all its as-planned range points that are recognized, and the visible surface of an object without occlusion, estimated by summing up the surfaces of its front-facing STL facets:

$$\text{TOR} = 1 - \frac{\text{Recognized As-planned Covered Surface}}{\text{Visible Surface Without Occlusion}}$$

This computation of the TOR is a crude estimation of the true TOR. Indeed, the recognized as-planned covered surface does not only vary with the level of occlusion, but also with the performance of the point recognition metric, so that a low point recognition performance would artificially increase the estimation of the TOR using the formula suggested here. Additionally, as explained in Section 4.4.1, the visible surface without occlusion calculated by summing the surfaces of front-facing facets is an upper bound of the true visible surface without occlusion. However, since it has been demonstrated in Section 4.3 that the developed approach achieves good accuracy performance, calculated recognized as-planned covered surfaces are probably good estimations of the true recognized surfaces, and this computation of the TOR can be assumed as an acceptable estimation of the true TOR.

Figure 4.5 shows the recall rates and numbers of recognized objects for different TORs estimated as suggested above. Compared to the results in Figure 4.4, both

the histogram and curve appear shifted to the right which is consistent with the fact the PIOR is a lower bound of the TOR. The results in Figure 4.5 first show that the recall rates are very high (about 100%) for TORs up to 85% but then significantly decrease. This shows that the developed approach handles occlusions well. The results even appear better than with the 3D-tensor -based approach developed by Mian et al. [82, 81] that is the 3D object recognition technique that has reported the best performance with occlusion to date (objects up to 85% were successfully recognized). Indeed, with the developed approach, the recall rate also decreases after 85% but not as significantly — this is just a crude comparison of the two approaches since the results were obtained with different data sets. In addition, It can be seen in Figure 4.4 that many objects with internal occlusions rates of at least 95% are successfully recognized. This further demonstrates the capacity of the developed approach to recognize highly occluded objects.

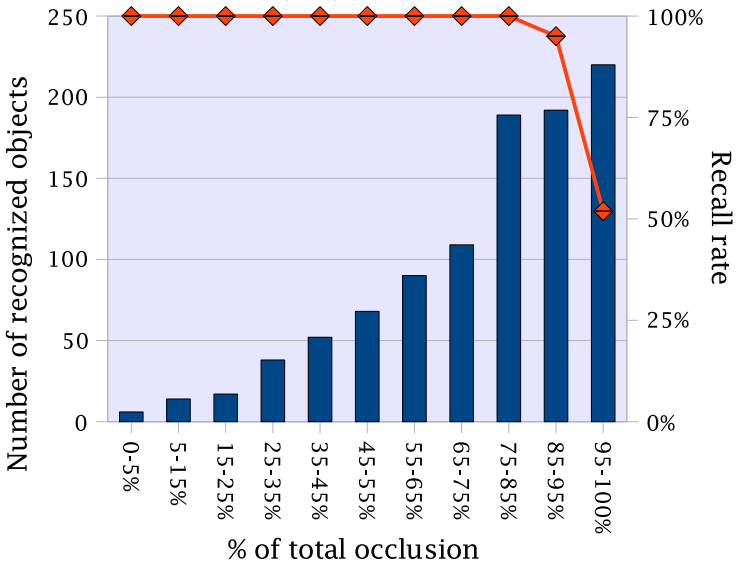

Figure 4.5: Recall rates for different levels of occlusions.

4.5 Efficiency

The efficiency of the developed approach is measured by the computational time necessary to recognize project 3D model objects in site laser scans. In Section 4.5.1, the overall computational time is analyzed with the five experiments described at the beginning of Section 4.3.2. Then, Section 4.5.2 investigates in more detail the efficiency of the developed approach for calculating as-planned range point clouds by comparing its performance with the one of another commonly implemented technique.

4.5.1 Overall Computational Performance

First of all, as discussed in Section 4.1 and summarized in Table 4.1, *Step 1* of the developed object recognition approach, namely the conversion of 3D model into STL format, only needs to be performed once for all the scans. The complexity of this step is thus not critical, so that it is discarded in this analysis — for information, it took only about five seconds to convert into STL format the 3D model used the five experiments presented in this chapter.

Table 4.8 summarizes the computational times of *Step 2*, *Step 3*, and *Step 4* and *Step 5* combined, for the five experiments described in Section 4.3.2. These times were obtained by running the VB.NET developed program on a computer having a 2.41 GHz processor and 2 GB RAM memory.

It first appears that it takes overall, for instance for *Experiment 3* — where *Scan 3* contains a little bit more than 810,000 scanned points and the 3D model contains 612 objects —, only about 3.5 minutes to recognize and extract the as-built range point clouds corresponding to all the 3D model objects present in the scan.

Then, it can also be concluded from Table 4.8 that *Step 3* seems to be the most critical one in terms of computational time. Its computational time is directly related to the efficiency of the developed technique for calculating as-planned range point clouds. As a result, it is of interest to compare the efficiency of this technique with the efficiency of other potential ones. This analysis is conducted in Section 4.5.2.

Table 4.8: Computational times (in seconds) of the steps 2 to 5 of the recognition process for the five scans.

	Experiment:				
	1	2	3	4	5
Process Step Times:					
Step 2 - Register model in scan	0.6	0.6	0.6	0.6	0.6
Step 3 - Calculate as-planned scan	174.3	156.2	186.4	157.2	70.4
Steps 4+5 - Recognize as-planned points and objects	11.2	8.5	10.0	8.4	2.5
Total (2+3+4+5)	186.1	165.3	197.0	166.1	73.5

4.5.2 Performance of The Developed Technique for Calculating As-planned Range Point Clouds

In this section, the efficiency of the developed technique for calculating as-planned range point clouds is assessed.

The efficiency of the chosen technique for this calculation impacts the computational times of *Step 3*, but also *Step 2*. Indeed, typical viewer-independent space partitioning data structures only need that the the location of the viewer (the ray source) be registered in the Cartesian coordinate system of the 3D model, which is a simple operation. In contrast, in the developed technique, the space partitioning data structure (a Bounding Volume Hierarchy (BVH)), and more exactly the type of bounding volumes it uses, the *minimum spherical angular bounding volume (MSABV)*, is viewer-dependent and is thus computed in the scan's spherical coordinate frame, which implies the registration (rotation, translation and coordinate conversion) of a large number of vertices. It is thus important to consider the computational time of *Step 2* in this efficiency analysis (although it will be shown that is has a negligible impact).

In order to analyze the efficiency of the developed approach for calculating as-planned range point clouds, it is proposed to compare the computational times of *Step 2* and *Step 3* obtained using this technique with those obtained using another common ray shooting technique.

This second technique is similar to the developed one in the sense that it uses the BVH as a spatial partitioning data structure. However, it uses spheres as bounding volumes. Spheres are observer-independent bounding volumes. Thus, the sphere-based technique differs from the developed one as the BVH can be calculated off-line, as soon the 3D model is converted in the STL format. The chosen sphere-based BVH has the same three-level structure as the MSABV-based BVH used in the developed approach (see Figure 3.2 in Section 3.4.2).

The calculation of the bounding spheres of a set of n 3D points has been a very intensively investigated problem. In the experiment conducted here, the approach presented in [46] is used for the calculation of the bounding sphere of each STL object. Note that this approach does not calculate the exact minimum bounding sphere, but is a computationally efficient approach to accurately estimate it. The calculation of the minimum bounding sphere of a STL facet is a special case of the problem solved in [46], and for which the solution can be obtained using a simple deterministic method.

The same culling techniques are also implemented, namely scan's viewing frustum culling and back-face culling.

The sphere-based technique used here is very popular since it is very efficient for dealing with real-time applications with dynamic scenes, such as in first-person shooter computer games. The reasons for this efficiency are that (1) sphere-based BVH are observer-independent, and (2) it is very simple to calculate whether a ray intersects a sphere.

In order to compare both techniques, a new experiment, *Experiment 5'*, is conducted with the same data as in *Experiment 5* but using the sphere-based technique instead of the MSABV-based one. Both techniques lead to the same performance in terms of accuracy, level of automation and robustness, but with very different computational complexities. Table 4.9 summarizes the computational times recorded for *Experiment 5* and *Experiment 5'*. The computational time for *Step 3* is also detailed for better analysis. It clearly appears that the MSABV-based technique is significantly more computationally efficient. This may first be surprising since the MSABV-based technique requires the computation of the BVH as part of the *Step 3*. However, spheres are not as "tight" bounding volumes as MSABVs. Therefore, with spheres, more ray-facet intersections are tested in average for the calculation of an as-planned point. And, since as-planned range point clouds typically contain at least several thousands of points, the time necessary to calculate the MSABV-based BVH is rapidly made up by the shorter average time to calculate each as-planned point. Note also that the impact of the developed technique on the computational complexity of *Step 2* is insignificant compared to the complexity of *Step 3*.

Table 4.9: Comparison of the computational performances of the developed object recognition technique using a MSABV-based BVH (*Experiment 5*) and of the common technique using a sphere-based BVH (*Experiment 5'*).

Computational times of Steps 2 and 3:	Experiment 5	Experiment 5'
Step 2 - Register model in scan:	0.6	≈0
Step 3 - Calculate as-planned range point cloud:	70.4	454.6
Step 3.1 - Calculate BVH:	55.3	NaN
Step 3.2 - Calculate cloud:	15.1	454.6
Total (2+3)	71.0	454.6

This experiment demonstrates that the developed approach achieves in practice efficient computational times to calculate as-planned range point clouds. It can however be noted that AEC&FM project 3D objects often have cubic forms in which case it would probably be more interesting to compare the efficiency of the developed approach with one using axis-aligned or oriented bounding boxes as

bounding volumes. The efficiency of the developed approach could also be compared with the efficiency of the technique by Keeler et al. [67] based on the calculation of spherical visibility maps and described in Section 3.4.1 (sub-section *Uniform grids, Octrees, BSP trees and kd-trees*). None of these comparisons have however been conducted at this point, and future work could focus on such investigations.

Furthermore, it should be noted that the computational time for the calculation of the MSABV-based BVH (*Step 3.1*) is strongly correlated with the value of the parameter $Incr$ used to calculate the bounding tilt angles of each STL facet's MSABV (see Appendix C). In the experiments conducted here, this parameter is set to $10\,mm$ which is very small. The advantage with such a small value is that it ensures reliable results in all situations. With the data sets used here, however, the same experiments conducted with a value of $Incr$ of $100\,mm$ lead to the same recognition results but with a computational time of Step 2 an order of magnitude lower. The reason is that, in these experiments, the distance between the scanner and the 3D model, and more exactly each facet of the model, is fairly large so that the phenomenon illustrated in Figure C.6 of Appendix C has an insignificant impact here. This indicates that the value of $Incr$ should be adjusted to different situations. In fact, $Incr$ should probably be automatically estimated for each facet as a function of the bounding pan angles of the facet's spherical bounding volume, the minimum distance of the facet to the scanner, and the scan angular resolution. This automated estimation of $Incr$ has not been investigated, and the small value of $10\,mm$ is systematically used.

Then, it must be noted that, while the number of points in each of the scans used here is large enough to provide reliable results with respect to the overall computational performance of the developed approach, it is expected that, in real life applications, scanned point clouds contain even more points. In fact, laser scanners of new generation enable the acquisition of scans with angular resolutions down to $150\mu rad$ [76], which is four to ten times denser by area than the scans here. As a result, it is expected that, in practice, the computational complexity of calculating MSABV-based BVHs will be insignificant compared to the reduction in the complexity of calculating as-planned range point clouds that they enable.

Furthermore, as already mentioned in Section 4.1, if it is decided to locate at a given spot a laser scanner for long periods or even the entire duration of a project, and conduct many scans from that spot, then the 3D model BVH is the same for all these scans and thus only has to be calculated once, which would reduce even further its impact on the overall computational complexity.

4.6 Conclusion

This chapter has investigated the performance of the developed approach in terms of level of automation, accuracy, robustness and efficiency.

It has first been shown that the developed approach is almost fully automated. The only manual part is the matching of corresponding benchmarks in the project 3D model and laser scan for the registration step (*Step 2*). Compared to currently used manually-intensive techniques for tracking the status of 3D objects on site, this approach thus constitutes a ground-breaking improvement in terms of level of automation.

With respect to accuracy, the results obtained with real-life data show that the developed approach enables the recognition of project 3D objects in laser scans with high recall, sensitivity and precision rates. It has been shown that the observed object recognition failures occurred with small objects, which is expected to have only small effects on applications such as automated 3D progress tracking. It has also been shown that the data used in the experiments conducted here had the particularity of having poor registration quality, which had a significant impact on the reported recognition results. With registration quality constraints such as those already used in the AEC&FM industry, the accuracy of the developed approach would likely further improve. Finally, other recognition failures were also due to errors in the 3D model. As a result, the developed approach has the potential to achieve the levels of object recognition accuracies qualitatively estimated in Section 2.4. It should also be noted that previous studies in civil engineering have only attempted to recognize a type of design 3D objects a 2D image and not a particular object.

In parallel, it has been shown that the developed approach is very robust with occlusions. It performs at least as well as, and possibly even better than, the best techniques reported in the literature, such as the recent one proposed by Mian et al. [82, 81].

Using the approach described in this thesis, object recognition can be achieved in small computational times. For instance, the as-built range point clouds of the 612 objects constituting a project 3D model were recognized in laser scans of close to a million range points in less than five minutes. Such computational times are significantly lower than the maximum of a few hours set as a performance objective in Section 2.4.

In conclusion, the developed approach demonstrates high performance for practical 3D object recognition in site laser scans. Further work could nonetheless be conducted with the aim of further improving this performance. For instance,

(1) the methods for the automated estimations of $\Delta\rho_{max}$ and $Surf_{min}$ could be refined; (2) soft recognition metrics could be explored; and (3) other techniques for the calculation of as-planned range point clouds could be investigated.

Given the demonstrated performance of the developed approach for project 3D CAD object recognition in construction site laser scans, it is now possible to investigate the use of the results that it can provide for important applications such as automated 3D progress tracking and automated dimensional quality control. The investigation of such applications is the focus of Chapter 5 that also shows the possibility to use the developed approach for other applications such as planning for scanning and strategic scanning.

Chapter 5

Enabled Applications: Feasibility Analysis and Experiments

The developed approach enables Automated 3D Data Collection (A3dDC). Further, as illustrated in Figure 5.1, if it is used with 3D laser scans acquired during the entire life of a project, it then enables the automated acquisition of the evolution of the 3D as-built status of the model 3D objects over time, that can be stored in a Project 4D Information Model (P4dIM). Note that the P4dIM can be integrated as a part of the entire Project Information Model (PIM).

The P4dIM enables multiple applications related to the management of construction projects' life cycle 3D data. Sections 5.2 to 5.4 present results of experiments demonstrating three Automated Project Performance Control (APPC) applications: *Automated construction progress (and productivity) tracking*, *Automated dimensional QA/QC*, and similarly *Automated dimensional health monitoring*. Then, Sections 5.5 and 5.6 present two other enabled applications with potential benefit to laser scanning in the AEC&FM context: *Planning for scanning* and *Strategic scanning*.

5.1 Experimental Data

The experimental results presented in this chapter are obtained with the same data sets as the ones used in Chapter 4. These include the 3D CAD model of the steel structure of a building and five laser scans obtained on two different days of its construction and from different locations. For more information about this experimental data, please refer to Section 4.2.

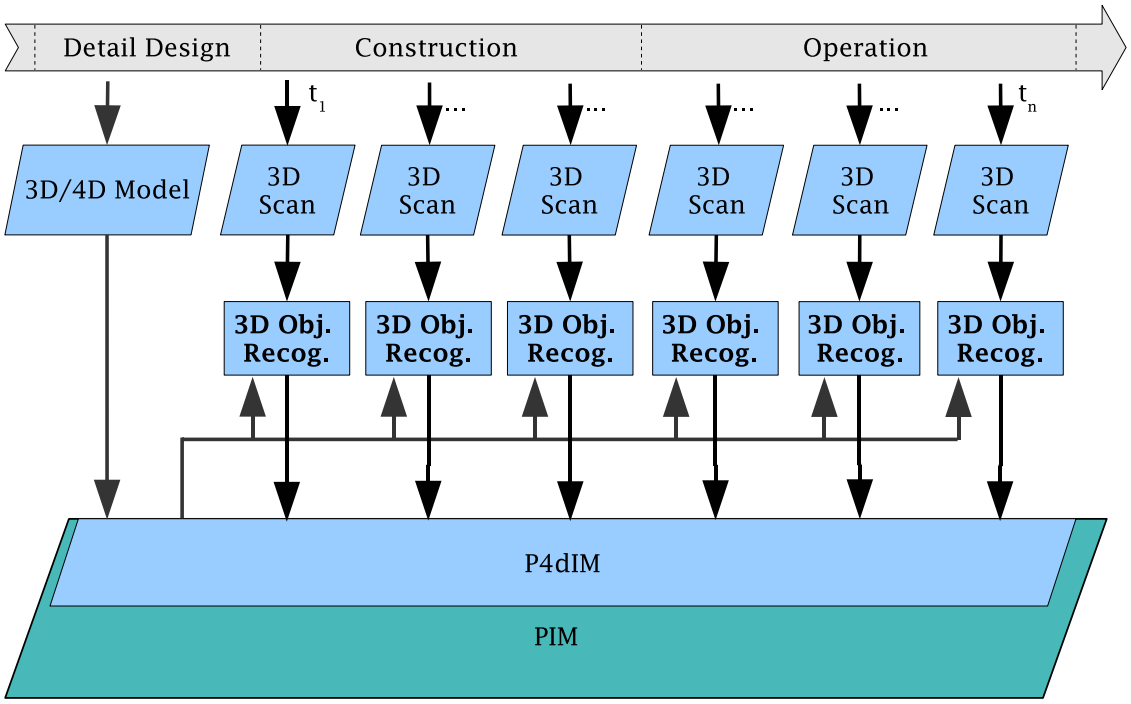

Figure 5.1: Illustration of automated construction of a Project 4D Information Model (p4dIM).

5.2 APPC: Automated Construction Progress Tracking

By analyzing the object recognition information contained in the P4dIM for two different days, it should be possible to automatically infer the construction progress between these two days — and productivity information can be inferred directly from progress.

Previously investigated Automated Data Collection (ADC) systems for progress tracking use indirect progress measurement methods, typically by tracking the location and activity of construction resources such as workers and equipment [86, 101, 124]. The developed approach, however, directly recognizes quantities put in place (even partial objects like partially built brick walls). The P4dIM can thus be used to measure progress directly.

5.2.1 Progress Calculation Method

As an example, consider a project with its 3D model. Scans may be conducted at different days but also during a same day from different locations and in different directions. Consider $\{S\}_{di}$ and $\{S\}_{di+1}$, the sets of scans conducted at respectively

day d_i and d_{i+1}. Then, *construction progress between the days d_i and d_{i+1} can be estimated by identifying in the P4dIM the objects that are recognized in $\{S\}_{di+1}$ but not in $\{S\}_{di}$.*

5.2.2 Experimental Results

An experiment is conducted that uses the data presented in Section 5.1, and that aims at investigating the performance of using the P4dIM and the progress calculation method above for construction project tracking.

Combining Daily Scans

First, it can be noted in the results presented in Tables 5.1 to 5.2 that combining the recognition results of different scans acquired on a same day increases, sometimes significantly, the overall object recognition accuracy performance for that day, in particular the recall rate. This is particularly true if the scans are obtained from very different locations.

Table 5.1: Recognition results for the day d_1 (values in columns 3 and 4 are numbers of objects).

Scan ID	Objects Recognized	Objects Scanned		Recall	Specificity	Precision
		No	Yes			
1	No	260	49	85%	90%	90%
	Yes	30	273			
2	No	298	49	83%	92%	90%
	Yes	26	239			
d_1	No	194	58	85%	83%	89%
	Yes	39	321			

Progress Inference

The performance of inferring construction progress for the periods d_0–d_1 and d_1–d_2 is now investigated based on the recognition results obtained for d_1 and d_2. d_0 is the day 0 of the construction, when no project element is built yet.

Table 5.3 summarizes the progress recognition accuracy performance obtained for the sets of scans $\{S\}_{d1}$ and $\{S\}_{d2}$ using the information contained in the P4dIM

Table 5.2: Recognition results for the day d_2 (values in columns 3 and 4 are numbers of objects).

Scan ID	Objects Recognized	Objects Scanned		Recall	Specificity	Precision
		No	Yes			
3	No	283	49	84%	91%	90%
	Yes	27	253			
4	No	327	60	78%	96%	94%
	Yes	13	212			
5	No	568	8	79%	99%	83%
	Yes	6	30			
d_2	No	212	48	87%	86%	90%
	Yes	34	318			

automatically constructed with the developed approach and the progress calculation method presented in Section *Progress Calculation Method*. In this table *actual progress* for a period d_i–d_{i+1} is calculated as the set of objects that are visually identified in at least one scan of d_{i+1} but not visually identified in any scan of d_i.

The results are quite disappointing, particularly for the period d_1–d_2. For instance, only 3 of the 9 objects that are part of the actual progress are properly recognized.

The problem is that the proposed approach to estimate the recognized progress is very sensitive to the accuracy of the object recognition results obtained for each day. For a period d_i–d_{i+1}, errors in both the object recognition results for d_i and d_{i+1} impact the estimation of progress. For instance, a failure to recognize an object in the scans of d_i may result, if it is recognized in at least one scan of d_{i+1}, in the wrong conclusion that it is part of the progress. Similarly, a failure to recognize an object in the scans of d_{i+1} may result, if it was not in any scan of d_i, in the wrong conclusion that it is not built yet. The reason why the results reported for the period d_0–d_1 are much better than for those of the period d_1–d_2 is that there is obviously no error in the object recognition results for day d_0 (nothing is built), so that only object recognition errors with the scans of day d_1 impact the accuracy of the recognized progress.

As discussed in Section 4.3.2, the object recognition results obtained with the available experimental data are not very good, due to several reasons, but mainly the poor registration quality. With regard to the the discussion in the previous paragraph, this likely explains the poor progress recognition results presented in Table 5.3.

Table 5.3: Progress recognition results for the periods d_0–d_1 and d_1–d_2 where recognized progress is calculated using the method in Section *Progress Calculation Method* (values in columns 3 and 4 are numbers of objects).

Period	Objects in Recognized Progress	Objects in Scanned Progress		Recall	Specificity	Precision
		No	Yes			
$d_0 - d_1$	No	194	58	85%	83%	89%
	Yes	39	321			
$d_1 - d_2$	No	587	6	33%	97%	16%
	Yes	16	3			

In order to be able to better assess the feasibility of using information contained in the P4dIM to automatically track progress, the following change in the calculation of the recognized progress is suggested: *the recognized progress for a period d_i–d_{i+1} is the set of objects that are recognized (using the developed approach) in at least one scan of day d_{i+1} and that are not visually identified in any scan of day d_i.*. In essence, progress calculation method is a relaxed version of the normally more appropriate (because fully automated) method presented in Section *Progress Calculation Method*. In this relaxed method, progress is calculated by simulating perfect recognition information for the scans of day d_i, so that it is only sensitive to the object recognition errors with the scans of d_{i+1}.

Table 5.4 summarizes the progress recognition accuracy performance obtained for the same data as in Table 5.3 but using this relaxed progress calculation method.

The results show that progress is quite successfully automatically recognized. For the period d_0–d_1, the results are the same as in Table 5.3, because the objects recognized at day d_0 are the same as the ones actually built: none. For the period d_1–d_2, much better results than in Table 5.3 are reported. First, 100% of the scanned progress over that period (9 objects) is automatically recognized. Then, most of the scanned *non-progress* (objects not part of the progress) is also automatically recognized (specificity rate of 95%). However, the precision rate appears to be very low (23%). Indeed, 31 objects are recognized as part of the scanned progress during the period d_1–d_2 although they are not (Type I error). This means that these 31 objects are recognized in at least one of the scans of $\{S\}_{d2}$, and are not visually identified in any scan of $\{S\}_{d1}$. This is actually to be related to the object recognition results reported with the scans of d_2, $\{S\}_{d2}$. Indeed, as can be seen in Table 5.2, 34 objects are recognized in at least one scan of $\{S\}_{d2}$ although

they are not in any of these scans. The reasons for these Type I errors, identified in Section 4.3, are:

1. The small sizes of these objects. (Note that this implies that they are probably not critical in terms of progress tracking); and
2. The poor 3D registration quality, which particularly impacts the recognition of small objects.

Table 5.4: Progress recognition results for the periods d_0–d_1 and d_1–d_2 using the relaxed method for the calculation of the recognized progress (values in columns 3 and 4 are numbers of objects).

Period	Objects in Recognized Progress	Objects in Scanned Progress		Recall	Specificity	Precision
		No	Yes			
$d_0 - d_1$	No	194	58	85%	83%	89%
	Yes	39	321			
$d_1 - d_2$	No	572	0	100%	95%	23%
	Yes	31	9			

Overall, the results in Table 5.4 demonstrate that, if 3D high-quality 3D registration can be ensured, P4dIMs built with the developed approach could potentially be used to automatically track construction progress (and consequently productivity). Nonetheless, it is acknowledged that the experiments presented here do not suffice to fully prove the feasibility of implementing this P4dIM-based APPC application. More comprehensive data sets with, in particular, better registration quality, would need to be obtained to strengthen this analysis.

The results presented in this section are further discussed below. In particular, means to improve them are suggested.

5.2.3 Discussion

Using 4D Models for Supporting Progress Tracking

The experimental results presented in Section 5.2.2, in particular the results reported in Table 5.3, illustrate the sensitivity of progress tracking calculation results to object recognition errors.

One way to improve these results is to take advantage of construction projects' 4D models. A project 4D model is the result of the fusion of the project 3D model and the project Construction Project Management (CPM) schedule. With the 4D model, the physically derived precedence relationships from the CPM schedule can be used to extract the *as-planned 3D model* of each day. This *as-planned 3D model* only contains the project 3D objects that are planned to be built at that date, and should improve automated progress monitoring results in two ways:

1. The *as-planned 3D model* of day d_i should provide a good estimate of the objects that are already built at day d_i, so that the progress at day d_{i+1} can be automatically inferred with the proposed method.

   From current practice, it is clear that most projects proceed only in the most general form with respect to their schedules and most individual activities are generally offset by days and weeks from their original schedule dates. CPM schedules may thus be argued to provide poor information with respect to the as-built status of a project at a given date. However, by using the developed laser scanning -based object recognition approach to recognize progress from day d_0, the progress recognized at the end of each day, d_i, can be used to automatically update and recompute the CPM schedule (and consequently the 4D model), so that the schedule is automatically maintained up-to-date.

2. An automatically updated CPM schedule, and consequently 4D model, also provides an up-to-date estimation of the expected as-planned 3D model for day d_{i+1}, which should optimize the object recognition accuracy performance for scans conducted on day d_{i+1} — as-built and as-planned range point clouds would better match —, and consequently ensure higher progress recognition accuracy performance for the period d_i–d_{i+1}.

Scanned Progress vs. True Progress

With the developed approach, only the scanned progress can be recognized. Therefore, if the scanned progress significantly differs from the true progress, the recognized progress will be misleading. It is thus important to ensure that the scanned progress actually reflects the true progress. This can be done by conducting many scans from many locations and in many directions.

It could be argued that this would result in the need to analyze many scans with a lot of redundant information. In that regard, Section 5.5 will discuss the possibility to use the developed approach to plan in advance and thus optimize the number and locations of scans to be conducted to ensure the acquisition of data from all (critical) objects.

Furthermore, despite multiple scans during one day, it is still likely that no range data is ever obtained for some objects, because they are systematically occluded by either *internal occlusions* or *external occlusions*.

Internal occlusions, partial or total, are taken into account by the developed object recognition approach and do not impact its accuracy performance, (it is only calculated based on the objects present in the scans). However, total internal occlusions may impact progress recognition accuracy similarly to object recognition errors. For instance, an object actually built at a day d_i may be fully occluded from all the scan locations of that day, but recognized in a scan of day d_{i+1}. This would result in the wrong conclusion that the object is part of the progress during the period d_i–d_{i+1} (Type I error). Similarly, an object actually built at day d_{i+1} may be fully occluded from all the scan locations of that day. This would result in the wrong conclusion that the object is not part of the progress during the period d_i–d_{i+1} (Type II error).

External occlusions cannot be taken into account a priori, although they are very common on construction sites. For instance, as can be seen in Figure G.2 (page 122) with *Scan 3*, portable toilets as well as a large container are present on the side of the scanned structure. Their presence results in full occlusions of some structural elements. Similarly to internal occlusions, neither partial nor full external occlusions impact the accuracy performance of the developed object recognition approach. However, total external occlusions may similarly impact the object recognition accuracy.

Two techniques can be implemented to reduce and mitigate the impact of total occlusions of built 3D model objects on the accuracy of the proposed approach for automated progress monitoring:

Reducing external occlusions: Scanned scenes should always be cleared as much as possible of non-model objects prior to conducting scanning operations. Such good practice would reduce the number of external occlusions, thus reducing their negative impact on the accuracy performance of the proposed approach for automated progress recognition.

Leveraging precedence relationships from CPM schedules: The physically derived precedence relationships from the CPM schedule can also be used to recognize with reasonable confidence objects which are not recognized in a day's fused scans and yet can be inferred to exist due to the recognition of successor elements. Implementing this could help significantly reduce the impact of all types of occlusions on the accuracy performance of the proposed approach for automated progress recognition.

Progress vs. 3D Progress

Finally, it must be noted that not all construction activities can be monitored in terms of progress and productivity by collecting 3D information only (*e.g.* painting activities). Reliable and efficient ADC systems for complete project progress and productivity tracking should thus consider fusing data and information from several monitoring systems such as those described in [86], [101] or [124].

5.3 APPC: Automated Dimensional QA/QC

The P4dIM obtained with the developed approach could be used to perform *automated dimensional Quality Assessment / Quality Control (QA/QC).*

The P4dIM stores detailed life-cycle range point clouds for each project object (as long as it has been scanned and recognized). Then, it can be observed that many AEC&FM project 3D objects are designed with parametric forms or combinations of parametric forms (*e.g.* cubic floors, cylindrical columns, H-beam). Approaches fitting parametric forms to point clouds, such as those presented in [74], could thus be used to fit to each object as-built point cloud the same type of 3D parametric form as the one it is designed with. Then, the main form parameters (*e.g.* length, width and height) of the designed and fitted 3D parametric forms can be compared to each other to infer dimensional quality information.

The advantage of such a comparison is that it is fully compatible with typical dimensional tolerances, that generally refer to the parameters of the 3D parametric form(s) used to design the objects. In fact, Boukamp and Akinci [20] present an approach for automatically extracting and processing construction specifications, including dimensional tolerances, from project documentations for each project object, or object type. Such an approach could be combined with the proposed method for automated dimensional monitoring to create a system for fully automated dimensional QA/QC.

As an illustrative example, consider a structural concrete column with a cylindrical shape, for which a recognized dense and sufficiently large range point cloud is stored in the P4dIM (see example in Figure 5.2). A cylinder fitting algorithm can be used to fit a cylinder to the scanned data, and the fitting results can be used to perform automated dimensional quality control, such as:

Horizontal location: The horizontal location of the as-built column can be controlled by investigating whether the horizontal location of the center point of the fitted cylinder is the same, within tolerances, as the horizontal location of the column in the scan-referenced 3D model.

Verticality: The verticality of the as-built column can be controlled by investigating whether the direction of the main axis of the fitted cylinder is vertical, within tolerances.

Diameter and Length: The diameter and length of the as-built column can be controlled by investigating whether the diameter and length of the fitted cylinder are the same, within tolerances, as those of the same column in the scan-referenced 3D model.

Note that information about the quality of the fit can also be used to estimate the reliability of the dimensional quality control results.

5.4 APPC: Automated Dimensional Health Monitoring

The structural health of a structure is often related to its dimensional integrity. Since 3D as-built point clouds of each project object are stored in the P4dIM over time, using methods such as the one presented in the previous section, could be used to monitor objects as-built dimensions over time. And, since 3D laser scans can be conducted remotely (from tens of metres), this would enable safe dimensional monitoring operations.

It must be noted that dimensional health monitoring often involve the analysis of the deformation of elements. Fitting the exact same hard parametric form as the one used in the 3D model is likely not appropriate to recognize deformations, and algorithms fitting deformable parametric forms should be preferred. Examples of algorithms to fit deformable forms, including deformable parametric forms, can be found in [34, 62].

5.5 Planning For Scanning

Further than enabling APPC applications, the developed approach would enable three additional important applications: *planning for scanning* and *strategic scanning*. The first one is presented in this section, and the next one in Section 5.6.

For each scan, the developed approach conducts, from the same position, a virtual (as-planned) scan using the scan-referenced project 3D model as the virtually scanned world. The assumption is that, if the building is built where it is intended to be, the project elements should be positioned in the exact same way in the two

(a) Design of the structure.

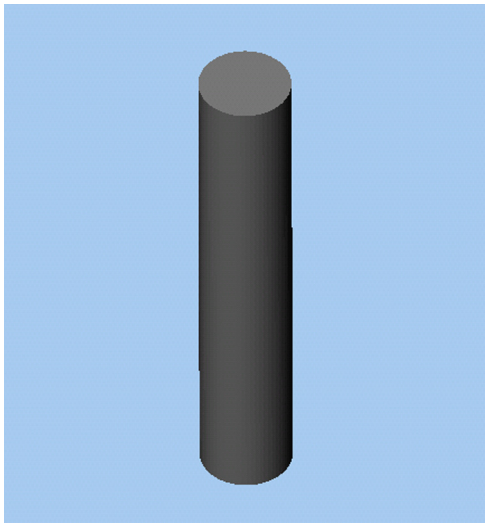

(b) Design of one of the structure's columns.

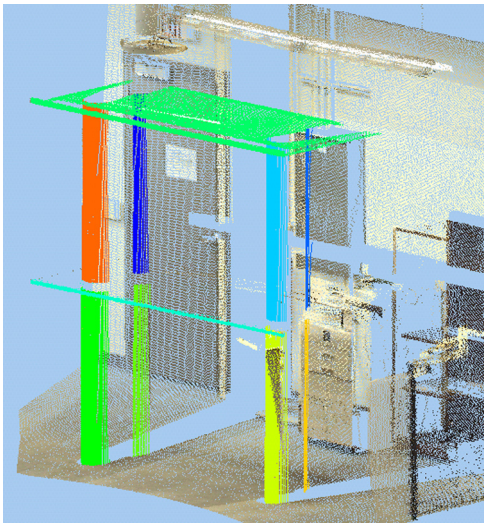

(c) Recognized points from the structure in the as-built scan.

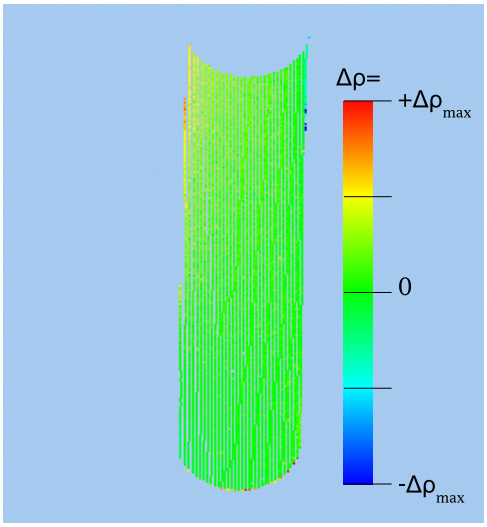

(d) Recognized points from the column. Points colors are set to $\Delta\rho$.

Figure 5.2: Example of a model and recognized as-built range point cloud of a structure. The results are detailed for one column with a cylindrical shape from a structure.

scans. The analysis of the performance of the developed approach presented in Chapter 4 confirms that this assumption is generally correct.

However, what this performance analysis does not clearly emphasize is that an as-planned point cloud can be used to *test* a scanning position prior to conducting the scan in reality, and investigate whether it would enable the acquisition of 3D information of objects considered of interest.

For instance, in the case of project progress monitoring, it can be determined *a priori* the recognition of which objects is critical to infer the expected progress. Then, the analysis of the as-planned range point cloud from a given location can provide information about which objects are expected to be recognized in the real scan from this location — and even the quantity of information (surface) that is expected to be recognized for each of them. If no (or not enough) information about a critical object is expected to be obtained from this location, another scan location can be investigated.

This idea can be pushed further. The developed approach could be used, before the construction of a project is even started, to plan the *project life cycle scanning operations*. It would enable the optimization of the number of scans and their locations that would need to be performed during a project in order to ensure the acquisition of 3D information *a priori* identified as critical to specific APPC applications.

This approach can be seen as part of the more general paradigm of *construction inspection planning*. Preliminary work investigating a formalism for construction inspection planning has been reported by Gordon et al. [51].

Note that such an approach for planning for scanning would perform well only if the virtually scanned scenes faithfully represent the scenes expected to be scanned in reality. As discussed in Section 5.2.3, using the project 4D model would be very beneficial to that end. Also, as mentioned in Section 5.2.3, *external occlusions* (*e.g.* equipment and temporary structures) are very common on construction sites and constitute an additional source of recognition error. So, using the developed approach for planning for scanning would result in the necessity to ensure that scanned scenes be cleared as much as possible of non-model objects prior to conducting real scanning operations.

5.5.1 Experiment

An experiment is conducted to test the feasibility of using the developed approach for planning for scanning.

Table 5.5 summarizes the planned *vs* scanned (visually identified) object recognition results and performance obtained for the same five experiments as in Section 4.3 and in terms of number of objects. Table 5.6 summarizes the same results but in terms of as-planned covered surface.

It first appears in Table 5.5 that the developed approach achieves very good results in terms of recall, meaning that most of the scanned objects are also planned.

Table 5.6 confirms this result by showing that objects, that are planned but are not scanned, actually have as-planned range point clouds with small covered surfaces. They are thus probably not critical in terms of progress tracking.

It can, however, be argued from the results presented in Table 5.5 (and similarly in Table 5.6), that the approach achieves poor specificity and precision performances. However, these values are misleading. Indeed, they are to be related to the fact that these experiments are conducting using the entire 3D model of the project to calculate the as-planned point clouds. So, many objects may be in the as-planned point clouds but may not be built yet at the time of the scans. For instance, it can be seen in the 3D model displayed in Figure G.1 (page 123), that there is a small structure inside the main building frame that is in the 3D model and contains many objects (exactly 131), but that is not present in any of the five scans. These objects significantly impact, directly or indirectly (as internal occluders), the specificity and precision performances presented here.

Table 5.5: Planned vs. scanned objects for the five scans (the values in third and fourth columns are numbers of objects).

Experiment	Objects Planned	Objects Scanned		Recall	Specificity	Precision
		No	Yes			
1	No	156	6	98%	54%	70%
	Yes	134	316			
2	No	114	8	97%	35%	57%
	Yes	210	280			
3	No	140	6	98%	45%	64%
	Yes	170	296			
4	No	119	8	97%	35%	54%
	Yes	221	264			
5	No	556	2	95%	97%	67%
	Yes	18	36			
all	No	1,085	30	98%	59%	61%
	Yes	753	1,192			

In conclusion, as-planned range point clouds can be used to effectively predict the content, in terms of objects and covered surfaces, of actual laser scans. It thus possible to used as-planned range point clouds to perform planning for scanning.

Table 5.6: Planned vs. scanned objects for the five scans (the values in third and fourth columns are the sums of objects' as-planned covered surfaces in m^2).

Experiment	Objects Planned	Objects Scanned		Recall	Specificity	Precision
		No	Yes			
1	No	0.22	0.01	100%	1%	93%
	Yes	20.67	265.82			
2	No	0.16	0.05	100%	1%	90%
	Yes	27.29	248.97			
3	No	0.24	0	100%	1%	91%
	Yes	26.21	276.79			
4	No	0.19	0.01	100%	1%	88%
	Yes	32.42	230.4			
5	No	0	0	100%	0%	93%
	Yes	0.88	11.57			
all	No	0.81	0.08	100%	1%	91%
	Yes	107.48	1033.55			

5.6 Strategic Scanning

Further than planning for scanning, the developed approach could be used to perform strategic scanning.

As mentioned above, as-planned scans can be conducted prior to real scans to predict their expected 3D information content. Since, in an as-planned scan, it is known from which object each range point is obtained, it would be possible, when conducting the real scan from the exact same position, to control the scanner so that only range points that are expected to provide 3D information about the objects of interests are acquired.

This is of great interest to the AEC&FM industry. Indeed, project managers, who are currently dedicating resources to conduct project 3D scanning, face the situation that they must save enormous amounts of scanned data, from which only a small portion is actually useful to their control processes. With the proposed approach, only useful 3D scanned data would be acquired, thus reducing the overall amount of data being stored and processed during the life of a project.

Chapter 6

Conclusions and Recommendations

It is concluded that a method exists, which has been presented in this thesis, by which particular 3D objects may be reliably recognized in 3D construction images when *a priori*3D design information is available.

6.1 Contribution

This thesis presented a novel approach for accurate, robust, efficient and (almost) fully automated recognition of project 3D objects in site laser scans. It leverages the opportunities that project 3D CAD models and 3D registration technologies provide in the AEC&FM context.

A detailed analysis of the performance of this approach with respect to accuracy, robustness, efficiency and level of automation has been presented based on real-life data. The developed approach demonstrates high performances in all these areas, both by comparison with existing techniques for 3D object recognition in range images, and with respect to targets qualitatively estimated *a priori*, specific to this specific AEC&FM context, related to previous 2D image work, and based on the personal expertise of the author as well as feedback from an industry practitioner (the project manager of the project where all the experiments were conducted).

This approach is in fact the first reported work for automated 3D object recognition in site range images. Its performance demonstrates a potential for use in practice.

Performances, in particular accuracy, efficiency and robustness, are also reported with quantitative measures, so that this approach can be used as a benchmark for comparison with future research.

Experiments described in Chapter 5, show how the developed approach can be used to automatically construct a P4dIM recording the 3D status of each project 3D object over time. The P4dIM could then enable multiple APPC applications such as *Automated project progress control*, *Automated dimensional QA/QC* and *Automated dimensional health monitoring*. While only frameworks for the implementation of the two latter applications have been investigated, more detailed and conclusive experimental results with real-life data are reported on the feasibility of implementing automated project progress control.

Finally, experimental results with real-life data have shown how the developed approach can be used for implementing *automated planning for scanning* for optimizing scanning activities on site. Further optimizing of the scanning activities on site could be achieved by implementing *strategic scanning*, for which an implementation framework has simply been laid down.

6.2 Limitations

Despite the reported high performance of this work, some limitations of the developed approach and of its applicability to support APPC applications exist and must be emphasized.

In terms of accuracy, the achieved performance does not show perfect recall, sensitivity and precision rates. A major reason for the "not so high" reported accuracy performance results is the fact that the conducted experiments had poor registration quality. Additionally, the use of the complete 3D model to recognize objects in scans of scenes of a partially built project further impacted the accuracy results. In order to further demonstrate the performance of this approach, it would thus be of major interest to conduct a new set of experiments with higher registration quality and using 4D models.

The chosen recognition metrics may also be questioned. A more detailed sensitivity analysis of the accuracy performance with different estimations of the thresholds $\Delta\rho_{max}$ and $Surf_{min}$ may indicate that the chosen estimations are not optimal. Soft recognition criteria instead of the hard ones defined at this point may also result in improved object recognition performance.

In terms of efficiency, the developed approach shows a performance higher than qualitatively expected. Nonetheless, some areas of potential improvement have been identified. For instance, other ray shooting techniques for calculating as-planned range point clouds may lead to more efficient results: Ray partitioning could be implemented to complement the proposed technique, and more efficient methods

for calculating the bounding tilt angles of the MSABVs of STL facets could be investigated. Alternative techniques using viewer-independent bounding volumes (*e.g.* bounding boxes) could also be explored.

With respect to the APPC applications enabled by using P4dIMs constructed with the developed object recognition approach, the reported results are limited as well.

Although experimental results have been presented with respect to the accuracy performance of implementing automated progress tracking using P4dIMs built using the developed approach, the results are not quite conclusive. These are probably due to the poor quality of the experimental data at hand. Additionally, precedence information contained in CPM schedules has not been leveraged at this point.

Similar comments can be made with respect to the reported results on the planning for scanning application.

Finally, in the case of automated dimensional QA/QC, dimensional health monitoring and strategic scanning applications, no experimental results demonstrating their feasibility have been reported.

Furthermore, it must be noted that many APPC applications do not only rely on 3D information, but also other types of information (*e.g.* material availability, shipping information). It is suggested in this thesis to fuse different sources and types of information (*e.g.* resource location information obtained with RFID-based sensing systems) for increasing the completeness of such APPC applications. However, no experimental results are reported to support this.

6.3 Suggestions for Future Research

The previous section already listed some areas of potential improvement to the developed approach as well as to the use of P4dIMs constructed with it for supporting APPC applications.

Overall, it appears that the developed approach already performs very well with respect to efficiency and level of automation. In contrast, the accuracy performance of the approach has only been demonstrated to some level. The author believes that its true performance is much higher, with significant impact on APPC applications such as automated project progress tracking. A new set of more comprehensive and precise experiments is therefore needed. These experiments should demonstrate the possibility to achieve higher object recognition accuracy (*e.g.* $95-100\%$ recall rates) and robustness (*e.g.* higher recall rates for objects as much as 95% occluded). In

particular, the impact of higher registration quality on object recognition accuracy and robustness performance should be better demonstrated.

Additionally, these experiments should better demonstrate the performance of applications such as automated progress tracking and automated dimensional QA/QC using P4dIMs built using the developed approach.

If all these experiments show conclusive results, there is then little doubt that the AEC&FM industry will show interest in adopting this approach as a standard practice for project control (particularly for industrial projects) as well as a benchmark for comparing future solutions.

Appendix A

Description of the STL Format

The STereoLithography (STL) file format is known as the Rapid Prototyping industry's standard data transmission format. It was originally created by the company *3D Systems Inc.*, and most of today's CAD systems are capable of producing STL files. The STL format approximates the surfaces of a solid 3D surface with a tessellation of triangles, as illustrated with one example in Figure A.1. This appendix provides a detailed description of this format. Comprehensive detailed information about it can be found in [4].

A `.STL` file can be either in ASCII or binary format. The binary format does not allow the distinction between solids within the file, so that one file equals one solid, while the ASCII format allows this distinction, which is more adequate to the investigated problem.

As shown in Figure A.3, an ASCII formatted `.STL` file does not include any header and it successively describes each of the 3D objects included in the file, referred to as *solids*. Each solid is described by a series of triangles, referred to as *facets*. Each facet is described by (1) the $[x, y, z]$ coordinates in floating point numbers of its three vertices and (2) the $[x, y, z]$ coordinates of its unit normal vector (see Figure A.2). The direction of the normal vector is always related to the order in which the three vertices are described using the right hand rule, as illustrated in Figure A.2. It is therefore possible to ignore in the STL file the description information of the normal and infer it from the vertices.

In any given file, all the facet vertices are recorded so that all the facet normal vectors point either outwards or inwards with respect to the overall solid volume. The choice of the direction must be made by the user (outwards being generally the default choice).

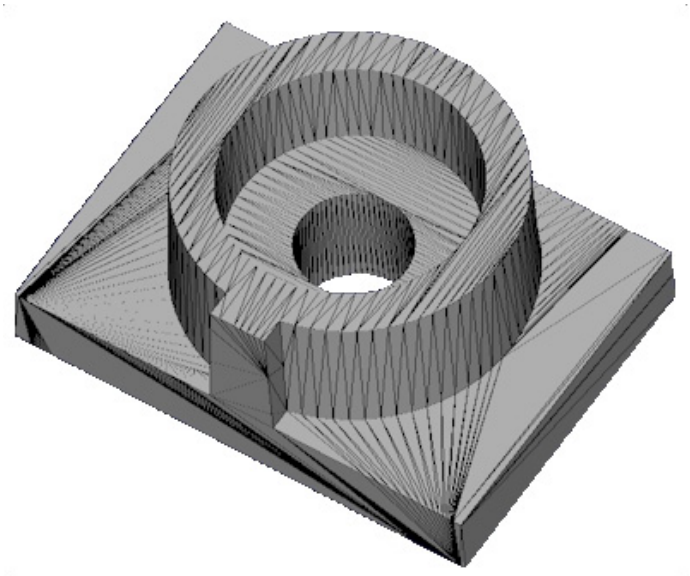

Figure A.1: Example of 3D STL-formatted object [122]. The STL format faithfully approximate the surface of any 3D object with a tesselation of oriented triangular facets.

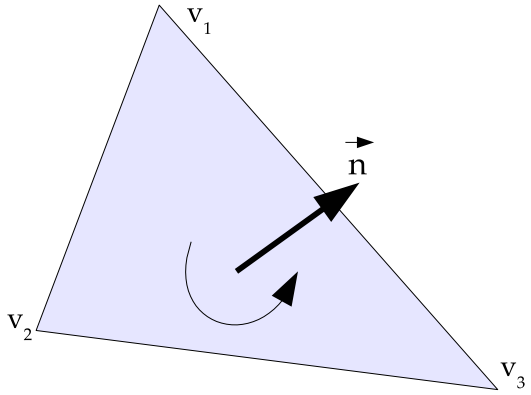

Figure A.2: Illustration of one STL triangular facet.

solid *name*
  facet normal n_x n_y n_z
    outer loop
      vertex V_{1x} V_{1y} V_{1z}
      vertex V_{2x} V_{2y} V_{2z}
      vertex V_{3x} V_{3y} V_{3z}
    endloop
  endfacet
  facet...
  ...
  endfacet
endsolid
solid...
...
endsolid

Figure A.3: ASCII format of a `.STL` file

Appendix B

The Spherical Coordinate Frame

This appendix describes the spherical coordinate frame used in this research. It also presents the transformation formula and corresponding algorithmic implementations for converting spherical coordinates into Cartesian coordinates, and *vice versa*.

B.1 The Spherical Coordinate Frame

Spherical coordinates can be expressed using different sets of three coordinates. The spherical coordinate system used here is illustrated in Figure B.1. Its three coordinates are:

Azimuth or Pan angle: Angle, φ, from the positive X-axis to the vector defined by the frame origin and the point projected on the (X-Y) plane. This angle is defined on the $[0; 2\pi[$ interval.

Zenith or Tilt angle: Angle, θ, from the positive Z-axis to the vector defined by the frame origin and the point. This angle is defined on the $[0; \pi[$ interval.

Radial Distance or Range. Euclidean distance, ρ, from the origin to the point. This distance is defined on the $[0; \infty[$ interval.

In this thesis, these coordinates are generally referred to as Pan, Tilt and Range (PTR) coordinates.

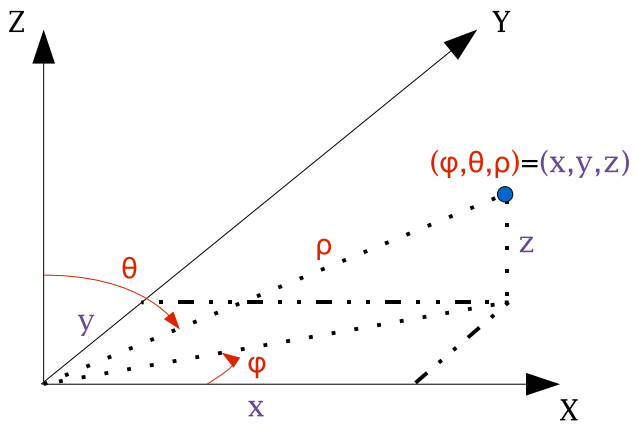

Figure B.1: Spherical coordinate frame.

B.2 Coordinate Frame Conversions

B.2.1 Spherical to Cartesian

The conversion of spherical coordinates, as defined here, into Cartesian coordinates is simple. The following formula can be used to calculate this conversion. Its algorithmic implementation is presented in Algorithm 10:

$$\begin{cases} x = \rho \sin(\theta) \cos(\varphi) \\ y = \rho \sin(\theta) \cos(\varphi) \\ z = \rho \cos(\theta) \end{cases}$$

Data: $[\varphi, \theta, \rho]$
Result: $[x, y, z]$

$x \leftarrow \rho$ `sin(`θ`)` `cos(`φ`)`
$y \leftarrow \rho$ `sin(`θ`)` `cos(`φ`)`
$z \leftarrow \rho$ `cos(`θ`)`

Algorithm 10: Function *SphericalToCartesian* converting spherical coordinates as defined here (pan, tilt, range) into Cartesian coordinates.

B.2.2 Cartesian to Spherical

The conversion of Cartesian coordinates into spherical coordinates, as defined here, is however more complicated. In particular, the calculation of the pan angle φ, that must be defined on the segment $[0; 2\Pi)$, must distinguish five different cases.

Figure B.2 illustrates these different cases. The following formula can be used to calculate this conversion. Its algorithmic implementation is presented in Algorithm 11:

$$\begin{cases} \rho = \sqrt{x^2 + y^2 + z^2} \\ \theta = \arccos\left(z/\rho\right) \\ \varphi = \begin{cases} \pi/4 & \text{if } x = 0 \text{ and } y \geq 0 \quad \text{(case 1)} \\ 3\pi/4 & \text{if } x = 0 \text{ and } y < 0 \quad \text{(case 2)} \\ \arctan\left(y/x\right) & \text{if } x > 0 \text{ and } y \geq 0 \quad \text{(case 3)} \\ 2\Pi \ + \ \arctan\left(y/x\right) & \text{if } x > 0 \text{ and } y < 0 \quad \text{(case 4)} \\ \Pi \ + \ \arctan\left(y/x\right) & \text{if } x < 0 \quad \text{(case 5)} \end{cases} \end{cases}$$

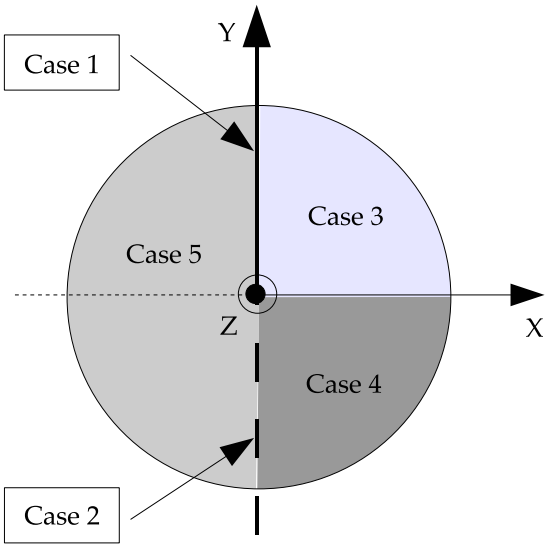

Figure B.2: The five different cases that must be distinguished in the calculation of the pan angle from Cartesian coordinates.

```
Data: [x, y, z]
Result: [φ, θ, ρ]

ρ ← √(x² + y² + z²)
θ ← acos(z/ρ)
if x = 0 then
    if y ≥ 0 then // Case 1
        φ ← π/4
    else// Case 2
        φ ← 3π/4
    end
else if x > 0 then
    if y ≥ 0 then // Case 3
        φ ← atan(y/x)
    else// Case 4
        φ ← 2Π + atan(y/x)
    end
else // Case 5
    φ ← Π + atan(y/x)
```

Algorithm 11: Function *CartesianToSpherical* converting Cartesian coordinates into spherical coordinates as defined here (pan, tilt, range).

Appendix C

Calculation of the Minimum Spherical Angular Bounding Volumes (MSABVs) of STL Entities

This appendix describes the calculation of the *Minimum Spherical Angular Bounding Volume (MSABV)* of a STL facet and of a STL object.

Figure C.1 illustrates the MSABV of a STL facet. A MSABV is described by a set of four spherical angles, two pan angles (φ_{min} and φ_{max}) and two tilt angles (θ_{min} and θ_{max}) that bound a definite set of points, here the vertices of the STL entity (facet or object). These four spherical bounding angles are defined as:

φ_{min}**:** The smallest of the two pan angles that *bound* the facet (or object).

φ_{max}**:** The largest of the two pan angles that *bound* the facet (or object).

θ_{min}**:** The smallest of the two tilt angles that *bound* the facet (or object).

θ_{max}**:** The largest of the two tilt angles that *bound* the facet (or object).

These definitions may appear odd at this point but are very important. The analysis conducted in this appendix will explain the reason for them.

The calculation of the bounding pan and tilt angles of mesh surfaces in a spherical coordinate frame is not trivial, mainly due to the fact that the ranges of definition of spherical pan and tilt angles are bounded. A simple method is presented here that takes advantage of the fact that (1) STL facets only contain three vertices; and (2) the MSABV of a STL object can be easily calculated based on the MSABVs

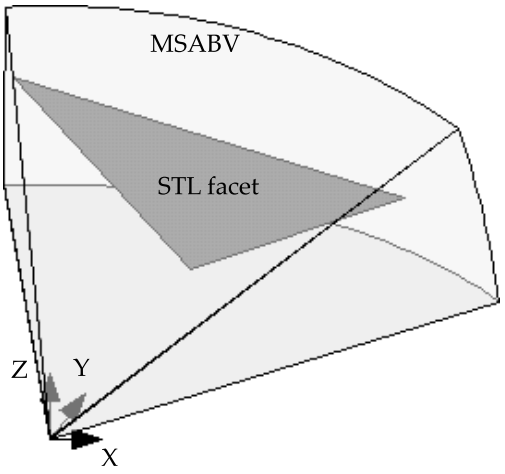

(a) 3D View.

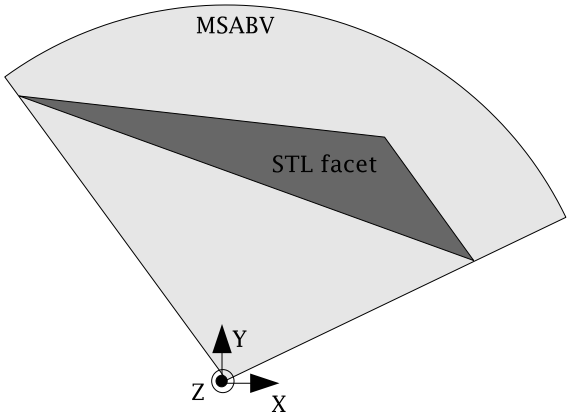

(b) Top View.

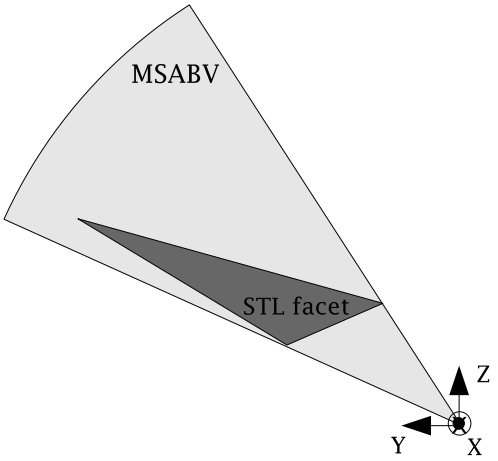

(c) Side View: Projection of the facet and MSABV by rotation around the z axis on one quadrant of the (YZ) plane.

Figure C.1: Illustration of the MSABV of a STL facet.

of its STL facets. The calculation of the MSABV of a STL facet is presented in Section C.1, and the calculation of the MSABV of a STL object is presented in Section C.2.

C.1 MSABV of a STL Facet

Figure C.2 displays a STL facet and the coordinates of its three vertices in the spherical coordinate frame of an investigated scan. It can be easily shown that the bounding pan and tilt angles of a STL facet are the pan and tilt angles of points

located at its boundary. The calculation of the bounding pan angles however differs from the calculation of the bounding tilt angles. They are thus presented separately in Sections C.1.1 and C.1.2 respectively.

The algorithmic implementation of the calculation of the MSABV of a STL facet is presented in Algorithm 12. It can be noted in this algorithm that the function *CalculateFacetMSABV* calculates three parameters in addition to φ_{min} and φ_{max}: *Above*, *Below* and *Inverted*. These parameters provide information concerning specific cases in which the MSABV of STL facet may fall into, and for which the interpretations of the bounding angles are different, as will be seen in Section C.1.1 below.

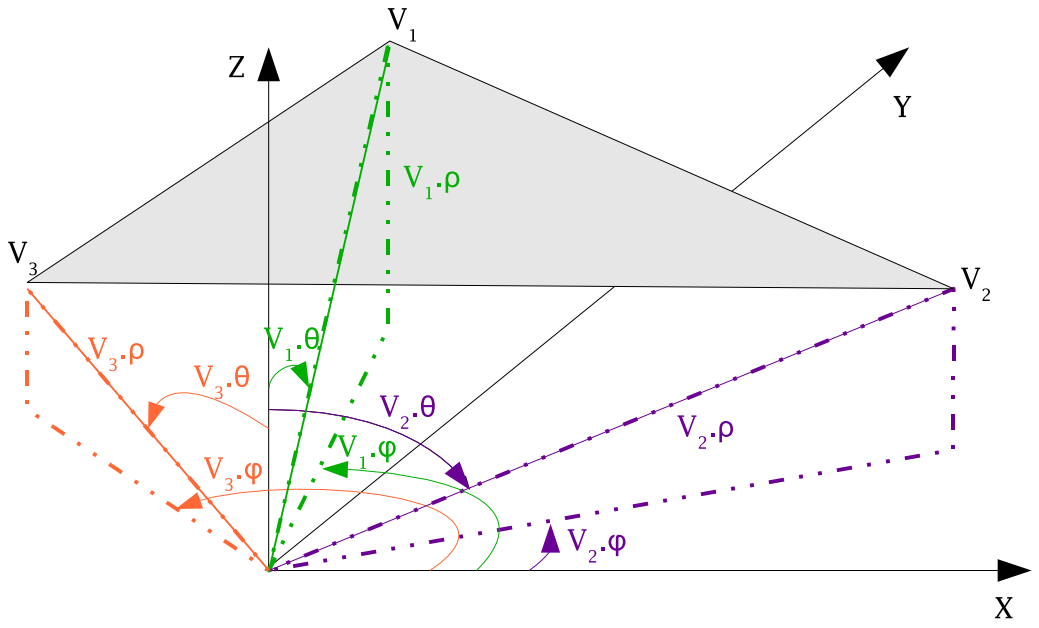

Figure C.2: Spherical coordinates of the three vertices of a STL facet.

Data: Facet, Incr
Result:

Facet.MSABV.$(\varphi_{min}, \varphi_{max}$, Inverted, Above, Below) ←
`CalculateFacetBoundingPanAngles(Facet)`
`// see Algorithm 13`
Facet.MSABV.$(\theta_{min}, \theta_{max})$ ← `CalculateFacetBoundingTiltAngles(Facet, Incr)`
`// see Algorithm 15`

Algorithm 12: Procedure *CalculateFacetMSABV* calculating the MSABV of a STL facet.

C.1.1 Bounding Pan Angles: φ_{min} and φ_{max}

Figure C.3 shows a scene with a STL facet viewed from the top of the scanner. It can be shown, as illustrated in Figure C.3, that the bounding pan angles of a STL facet, φ_{min} and φ_{max}, are always the pan angles of two of its vertices. Additionally, at least in the case illustrated here, which is referred to the *Regular* case, φ_{min} is the smallest and φ_{max} the largest of the pan angles of the three vertices. Therefore, they can be calculated as:

$$\varphi_{min} = \min\left(V_1.\varphi, V_2.\varphi, V_3.\varphi\right)$$
$$\varphi_{max} = \max\left(V_1.\varphi, V_2.\varphi, V_3.\varphi\right)$$

where: V_1, V_2 and V_3 are the three vertices of the STL facet.

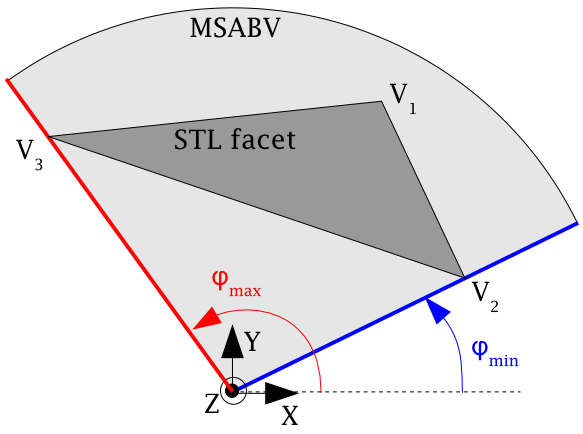

Figure C.3: Illustration of the MSABV of a STL facet for the situation where the facet has *Regular* bounding pan angles, φ_{min} and φ_{max}.

However, as shown in the two examples in Figure C.4, they are some cases for which φ_{min} and φ_{max} are not respectively the smallest and largest of the pan angles of the three vertices. In the example in Figure C.4(a), φ_{max} is truly the largest of the pan angles of the three vertices, but φ_{min} is not the smallest. And, in the example in Figure C.4(b), φ_{min} is truly the smallest of the pan angles of the three vertices, but φ_{max} is not the largest. Such cases are due to the fact that pan angles are only defined in the interval $[0; 2\pi[$, and they occur when "the facet intersects the positive x axis when viewed from the top". These cases are referred to as facets with *Inverted* bounding pan angles.

As shown in the example in Figure C.5, two additional cases must be distinguished, when the facet is *Above* or *Below* the scanner, which occurs when the z

axis intersects the facet. In these two cases, values of φ_{min} and φ_{max} calculated with the three vertices would be misleading and must be set to 0 and 2π respectively.

In conclusion, STL facets must be classified into four groups, *Regular*, *Inverted*, *Above* and *Below*, so that their bounding pan angles, φ_{min} and φ_{max} can be interpreted adequately. As will be seen in Appendix E, it is actually important to distinguish facets *Above* from facets *Below* the scanner.

Algorithm 13 presents the algorithmic implementation of the calculation of the bounding pan angles of a STL facet. The strategy is to: (1) sort the values of the pan angles of the three vertices into $\varphi_{mintemp}$, $\varphi_{midtemp}$, $\varphi_{maxtemp}$; and then (2) analyze those values to deduce which case the STL facet falls into and calculate the values of φ_{min} and φ_{max} accordingly. The calculation of the values φ_{min} nor φ_{max} according to the different cases is presented in Algorithm 14.

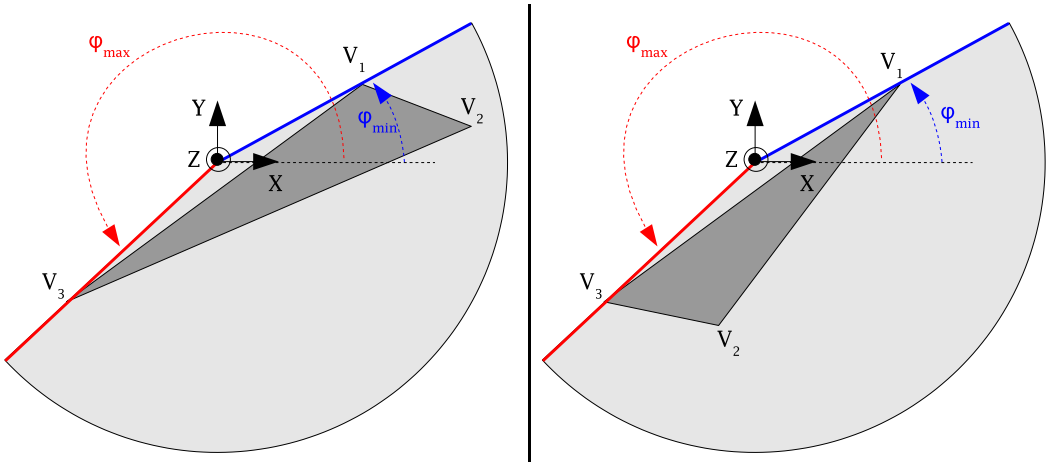

(a) Type I Inverted.

(b) Type II Inverted.

Figure C.4: Illustration of the MSABV of a STL facet for the two situations where the facet has *Inverted* bounding pan angles.

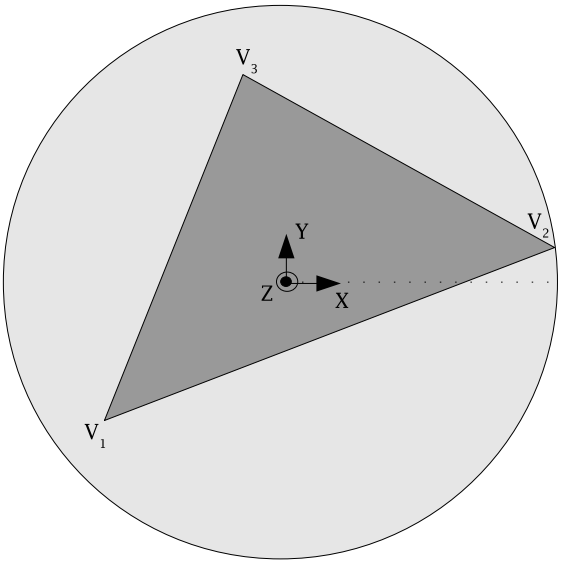

Figure C.5: Illustration of the MSABV of a STL facet for the situations where the facet is *Above* or *Below* the scanner.

In Algorithm 14, $Facet.\overrightarrow{n}$ is the unit vector normal to the STL facet as defined in the STL format (see Appendix A). Also, It can be noted in this algorithm that the distinction between a facet Above and a facet Below the scanner considers only the case when the facet is *front-facing* (with respect to the scanner's location). This is appropriate since, as will be discussed in Appendix D, no as-planned range point can be obtained from an back-facing facet, so that all the back-facing facets are discarded. The calculation of whether a STL facet is *back-facing* is presented in Appendix D.

Data: Facet
Result: φ_{min}, φ_{max}, Inverted, Above, Below

$\varphi_{maxtemp} \leftarrow \mathsf{Facet.V}_1.\varphi$

if $\mathsf{Facet.V}_2.\varphi > \varphi_{maxtemp}$ **then**
  $\varphi_{midtemp} \leftarrow \varphi_{maxtemp}$
  $\varphi_{maxtemp} \leftarrow \mathsf{Facet.V}_2.\varphi$
else
  $\varphi_{midtemp} \leftarrow \mathsf{Facet.V}_2.\varphi$
end

if $\mathsf{Facet.V}_3.\varphi > \varphi_{maxtemp}$ **then**
  $\varphi_{mintemp} \leftarrow \varphi_{midtemp}$
  $\varphi_{midtemp} \leftarrow \varphi_{maxtemp}$
  $\varphi_{maxtemp} \leftarrow \mathsf{Facet.V}_3.\varphi$
else if $\mathsf{Facet.V}_3.\varphi > \varphi_{midtemp}$ **then**
  $\varphi_{mintemp} \leftarrow \varphi_{midtemp}$
  $\varphi_{midtemp} \leftarrow \mathsf{Facet.V}_3.\varphi$
else
  $\varphi_{mintemp} \leftarrow \mathsf{Facet.V}_3.\varphi$
end

$(\varphi_{min}, \varphi_{max}, \mathsf{Inverted}, \mathsf{Above}, \mathsf{Below}) \leftarrow$ `CalculateFacetBoundingPanAngles2`$(\varphi_{mintemp}, \varphi_{midtemp}, \varphi_{maxtemp}, \mathsf{Facet}.\overrightarrow{n})$ `// see Algorithm 14`

Algorithm 13: Function *CalculateFacetBoundingPanAngles* calculating the bounding pan angles of a STL facet.

```
Data: φ_mintemp, φ_midtemp, φ_maxtemp, n⃗
Result: φ_min, φ_max, Inverted, Above, Below

Above ← False
Below ← False
Inverted ← False

if φ_maxtemp − φ_mintemp > π then
    if φ_midtemp − φ_mintemp ≤ π then
        if φ_maxtemp − φ_midtemp ≤ π then
            if n⃗ · Z⃗ < 0 then // Z⃗: vertical axis of the scan's coordinate
            frame
             |  Above ← True
            else
             |  Below ← True
            end
            φ_min ← 0
            φ_max ← 2π
        else
            Inverted ← True
            φ_min ← φ_midtemp
            φ_max ← φ_maxtemp
        end
    else
        Inverted ← True
        φ_min ← φ_mintemp
        φ_max ← φ_midtemp
    end
else
    φ_min ← φ_mintemp
    φ_max ← φ_maxtemp
end
```

Algorithm 14: Function *CalculateFacetBoundingPanAngles2* calculating whether a STL facet falls into any of the three special cases (*Inverted*, *Above*, *Below*), and calculating the values of its bounding pan angles, φ_{min} and φ_{max}, accordingly.

C.1.2 Bounding Tilt Angles: θ_{min} and θ_{max}

The calculation of the bounding tilt angles is simpler in the sense that it does not require distinguishing between different cases. However, it is more complicated because, as tentatively illustrated with one example in Figure C.6, while the bounding tilt angles of a STL facet are also the tilt angles of points located at its boundary, they are not necessarily those of two of its vertices. The calculation of the exact bounding tilt angles, θ_{min} and θ_{max}, of a STL facet thus requires calculating the smallest and largest tilt angles of its three edges and then deduce θ_{min} and θ_{max} from the set composed of these three edges.

The exact calculation of the bounding tilt angles of an edge of a STL facet, *i.e.* a segment, is however quite complicated, as it would require determining the equation of the edge in spherical coordinates. Such a function is not only non-linear, but is also piecewise continuous.

A simpler but approximative approach is used here. As illustrated in Figure C.7, the strategy is to calculate the tilt angles of a finite number of evenly spread points on each edge. The bounding tilt angles of the edge are then estimated as the bounding tilt angles of the set composed of all these points. The algorithmic implementation of this calculation is presented in Algorithm 15.

This approach requires setting the incremental distance used to pick the points along the edge, $Incr$. If $Incr$ is small, the resulting estimated bounding tilt angles will be a good approximation of the true bounding tilt angles, but this will be achieved at the expense of a longer calculation time. In the experiments presented in this thesis, a value of $Incr$ of **10mm** is used for ensuring a good estimation of the facets' bounding tilt angles, despite its computational impact.

A method for the selection of $Incr$ based on some properties of each STL facet (bounding pan angles and distance to the scanner) is discussed in Chapter 4, but has not been implemented. Such a method would enable reducing the computational complexity of this calculation.

Another, certainly better, method would be to calculate the bounding tilt angles of each section of the edge, *i.e.* sub-segment, for which the equation in spherical coordinates is fully continuous, and then infer the bounding tilt angles of the edge as the bounding tilt angles of the set of sections constituting the edge. Such a method has not been investigated either.

C.2 MSABV of a STL Object

The MSABV of a STL object can be deduced from the MSABV of all its facets. More exactly, it is the union of the MSABV of its facets. The algorithmic implemen-

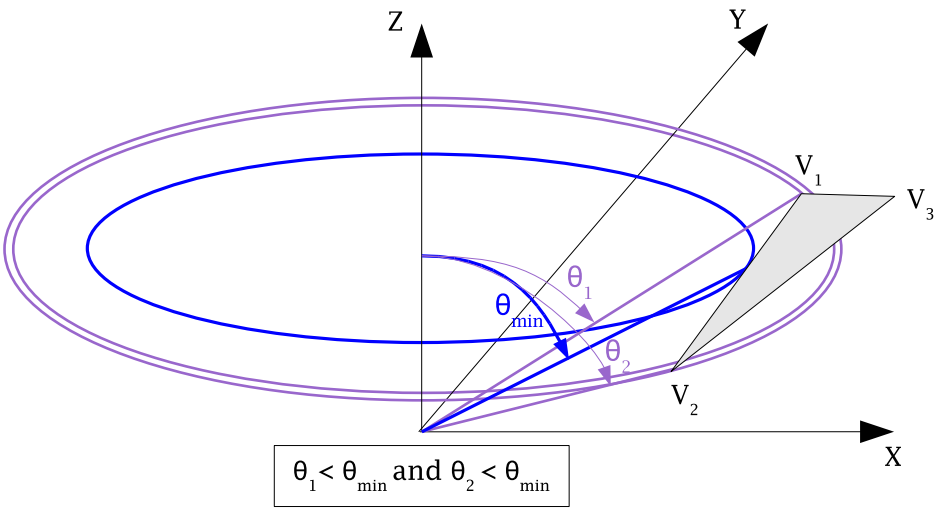

Figure C.6: Example of a case where θ_{min} is not the tilt angle of one of the three STL triangle vertices.

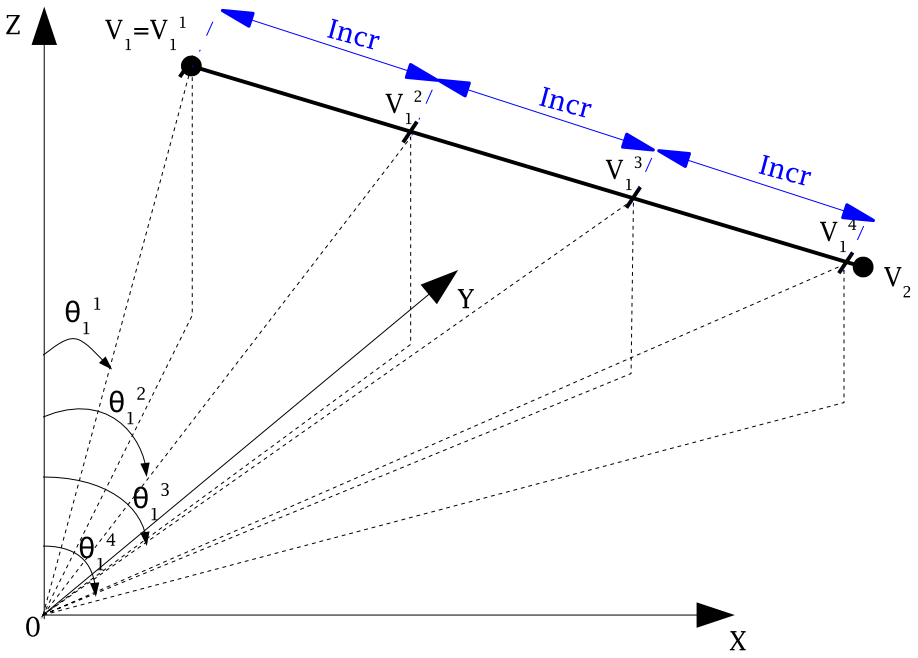

Figure C.7: Illustration of the proposed strategy for estimaing of the bounding tilt angles of an edge of a STL facet.

tation of this calculation is presented in Algorithm 16, that calls the Algorithms 17 and 18 for the calculations of the bounding pan and tilt angles respectively. It can be seen that, similarly to the STL facets, the interpretation of the bounding pan

Data: Facet, Incr
Result: θ_{min} and θ_{max}

$\theta_{min} \leftarrow \pi$
$\theta_{max} \leftarrow 0$
for each Facet.Edge *as* E **do**
  E.Length $\leftarrow \left\| \overrightarrow{\mathsf{E}.V_b.[x,y,z] - \mathsf{E}.V_a.[x,y,z]} \right\|$
  E.$\overrightarrow{u} \leftarrow \frac{\overrightarrow{\mathsf{E}.V_b - \mathsf{E}.V_a}}{\mathsf{E.Length}}$
  TempPoint.$[x,y,z] \leftarrow \mathsf{E}.V_a.[x,y,z]$
  while $\left\| \overrightarrow{\mathsf{TempPoint}.[x,y,z] - \mathsf{E}.V_a.[x,y,z]} \right\| \leq$ E.Length **do**
    TempPoint.$\theta \leftarrow$ `CalculateTiltAngle`(TempPoint.$[x,y,z]$)
    if TempPoint.$\theta < \theta_{min}$ **then** $\theta_{min} \leftarrow$ TempPoint.θ
    if TempPoint.$\theta > \theta_{max}$ **then** $\theta_{max} \leftarrow$ TempPoint.θ
    TempPoint.$[x,y,z] \leftarrow$ TempPoint.$[x,y,z]$ + Incr (E.$\overrightarrow{u}$)
  end
end
if Facet.Above = True **then** $\theta_{min} \leftarrow 0$
if Facet.Below = True **then** $\theta_{max} \leftarrow \pi$

Algorithm 15: Function *CalculateFacetBoundingTiltAngles* estimating the bounding tilt angles of a STL triangle.

angles must distinguish between four cases: *Regular*, *Above*, *Below* and *Inverted*. A STL object falls in one of the last three cases if at least one of its facets falls into that same case.

Data: Object
Result: φ_{min}, φ_{max}, θ_{min}, θ_{max}, Inverted, Above, Below

Object.MSABV.$(\varphi_{min}, \varphi_{max}$, Above, Below, Inverted$) \leftarrow$
`CalculateObjectBoundingPanAngles`(Object.{Facet}) `// see Algorithm 17`
Object.MSABV.$(\theta_{min}, \theta_{max}) \leftarrow$ `CalculateObjectBoundingTiltAngles`(Object.{Facet})
`// see Algorithm 18`

Algorithm 16: Function *CalculateObjectMSABV* calculating the MSABV of a STL object.

```
Data: {Facet}
Result: φ_min, φ_max, Above, Below, Inverted

Above ← False
Below ← False
Inverted ← False

for each Facet do
    if Facet.Above = True then Above ← True
    if Facet.Below = True then Below ← True
    if Facet.Inverted = True then Inverted ← True
end

φ_min ← 2 π
φ_max ← 0
if Above = True or Below = True then
    φ_min ← 0
    φ_max ← 2 π
else if Inverted = True then
    for each Facet do
        if Facet.Inverted = True then
            if Facet.φ_min > φ_min then φ_min ← Facet.φ_min
            if Facet.φ_max < φ_max then φ_max ← Facet.φ_max
        else
            if Facet.φ_min > π then
                if Facet.φ_min < φ_max then φ_max ← Facet.φ_min
            else
                if Facet.φ_max > φ_min then φ_min ← Facet.φ_max
            end
        end
    end
else
    for each Facet do
        if Facet.φ_min < φ_min then φ_min ← Facet.φ_min
        if Facet.φ_max > φ_max then φ_max ← Facet.φ_max
    end
end
```

Algorithm 17: Function *CalculateObjectBoundingPanAngles* calculating whether a STL object fall into one of the four cases (*Regular*, *Above*, *Below*, *Inverted*) and calculating its bounding pan angles, φ_{min} and φ_{max}, accordingly.

Data: {Facet}
Result: θ_{min}, θ_{max}

$\theta_{min} \leftarrow \pi$
$\theta_{max} \leftarrow 0$

for each Facet **do**
  if Facet.$\theta_{min} < \theta_{min}$ **then** $\theta_{min} \leftarrow$ Facet.θ_{min}
  if Facet.$\theta_{max} > \theta_{max}$ **then** $\theta_{max} \leftarrow$ Facet.θ_{max}
end

Algorithm 18: Function *CalculateObjectBoundingTiltAngles* estimating the bounding tilt angles of a STL object.

Appendix D

Construction of the Bounding Volume Hierarchy (BVH) of a project 3D Model

This appendix describes the calculation of the proposed *Bounding Volume Hierarchy (BVH)* of a STL-formatted 3D model, where the bounding volumes are *Minimum Spherical Angular Bounding Volumes* (MSABVs). The calculations of the MSABV of STL entities (facets and objects) is presented in Appendix C.

It is particularly shown here that the size of the BVH can be significantly and easily reduced (or pruned), without impacting the resulting as-planned point calculation, by using *scan's viewing frustum culling* and *back-facing facet culling* techniques, leading to a significant reduction in the computational complexity of of the BVH for the calculation of each as-planned range point.

The *back-facing facet culling* and *scan's viewing frustum culling* techniques used here are described in Sections D.1 and D.2 respectively. The resulting calculation of the pruned BVH is presented in Section D.3.

D.1 Back-Facing Facet Culling

An as-planned range point can only be obtained from a *front-facing* facet, with respect to the scanner's location. The reason is that, in the problem investigated here, facets are part of closed tessellated volumes, so that, from any view point, any back-facing facet is always hidden behind other front-facing facets.

Then, as presented in Appendix A, all the facet normal vectors of a STL-formated model are oriented toward the outside of objects (or all of them toward

the inside; this is chosen *a priori*), so that it is simple, given a STL facet's normal vector, to identify whether it is back-facing (or front-facing) from the scanner's location (see illustration in Figure D.1).

This *back-facing* property must not be confused with the *visibility* property. In the case of closed tessellated volumes, back-facing facet are always hidden, front-facing facet are not necessarily all visible, so that the set of hidden facets is smaller than the set of back-facing ones. As a result, performing *facet visibility culling* generally achieves a more effective facet culling than back-facing facet culling. However, it is more complicated to calculate whether a facet is hidden rather than simply back-facing, so that back-facing facet culling can be implemented more efficiently. Back-facing facet culling is preferred here.

As illustrated in Figure D.1, the facing property (front-facing or back-facing) of a STL facet can easily be calculated by comparing the direction of its normal vector with its location with respect to the scanner's origin. For this, the scalar product between any vector from the scan's origin to any point on the STL facet (for instance the coordinate vector of its first vertex V_1) and the vector normal to the facet $\overrightarrow{n}$ is calculated. If the scalar product is strictly negative, then the facet is front-facing; it is back-facing otherwise. The algorithmic implementation of this calculation is presented in Algorithm 19. It assumes that the normal vector to the facet points outside the object's volume. This can be ensured for all facets when converting the 3D model into STL format (see Appendix A).

The number of back-facing facets in a scan-referenced 3D model is typically roughly equal to half of all the model facets — mainly because most AEC&FM 3D objects present vertical and horizontal symmetries. Therefore, by implementing back-facing facet culling, the size of the BVH of the 3D model can be significantly reduced, leading a significant improvement in the computational complexity of the calculation of each as-planned range point.

Data: Facet
Result:

if Facet.$\overrightarrow{V_1}$ · Facet.$\overrightarrow{n} < 0$ **then**
  Facet.IsFrontFacing ← True
else
  Facet.IsFrontFacing ← False
end

Algorithm 19: Procedure *CalculateFacetIsFrontFacing* calculating whether the facet is front-facing from the scanner's origin.

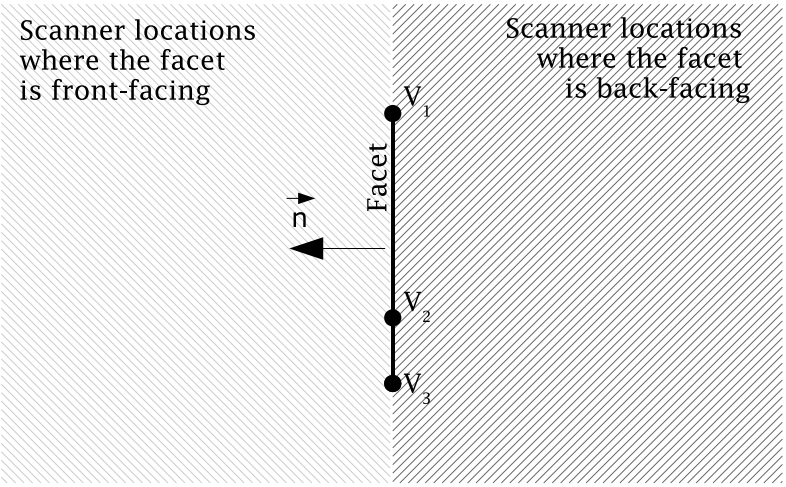

Figure D.1: Illustration of the facing property (front-facing or back-facing) of a STL facet given its location with respect to the scanner's origin. This figure considers that facet normal vectors are oriented toward the outside of the volumes they describe.

D.2 Scan's Viewing Frustum Culling

D.2.1 Calculation of a Scan's Viewing Frustum

It is possible to calculate the MSABV of the scan too, which can be seen as the *scan's viewing frustum*. The scan's viewing frustum can be calculated as follows. It is first assumed that the scan is conducted by scanning vertical lines of points "from left to right". This assumption is appropriate as all known laser scanners, including the one used in this research, conduct scans this way. As a result, the bounding pan angles of the scan's frustum are the pan angles of its first and last points. Similarly to the MSABVs of STL entities, the interpretation of these bounding angles must however distinguish two cases: *Regular* and *Inverted*. Note that the cases *Above* and *Below* do not apply here, because the scan's viewing frustum is the MSABV of a set of points, not of a surface.

Then, the bounding tilt angles of the scan's frustum are calculated as the minimum and maximum of the tilt angles of all the range points constituting the scan. As just mentioned, contrary to the MSABV of STL facets and objects, we deal here with points not surfaces, so that there is no need to calculate the bounding tilt angles of the edges connecting the scan's points.

The algorithmic implementation of this calculation of a scan's viewing frustum is presented in Algorithm 20. Since the scan's frustum does not depend on the scan-referencing of the model, its calculation can be performed at the very beginning of

the recognition process, as shown in Algorithm 1.

```
Data: Scan
Result:

Calculation of the bounding pan angles of a scan's viewing frustum.
Scan.Frustum.φ_max ← Scan.P_B 1 // First scanned point
Scan.Frustum.φ_min ← Scan.P_B max // Last scanned point
Scan.Frustum.Inverted ← False
if φ_max < φ_min then
    Scan.Frustum.Inverted ← True
end

Calculation of the bounding tilt angles of a scan's viewing frustum.
for each Scan P_B do
    if P_B.θ < Scan.θ_min then Scan.Frustum.θ_min ← P_B.θ
    if P_B.θ > Scan.θ_max then Scan.Frustum.θ_max ← P_B.θ
end
```

Algorithm 20: Procedure *CalculateScanFrustum* calculating a scan's frustum.

D.2.2 Does a STL Entity Intersect a Scan's Viewing Frustum?

As illustrated in Figure D.2, none of the rays of an investigated scan can intersect a STL entity (facet or object) if the entity's MSABV does not intersect the scan's viewing frustum. Therefore, the BVH can be pruned of the STL entities whose MSABV do not intersect the scan's viewing frustum.

The calculation for testing whether the MSABV of a STL facet intersects the scan's viewing frustum, and therefore whether the STL facet itself intersects it, is presented in Algorithm 21. This test simply compares the bounding pan and tilt angles of the MSABV of the facet and of the scan's viewing frustum. This comparison must distinguish several cases depending on whether the MSABV of the STL facet or/and the scan's viewing frustum fall into the different special cases identified in Section C.1 (Appendix C) and Section D.2.1 respectively.

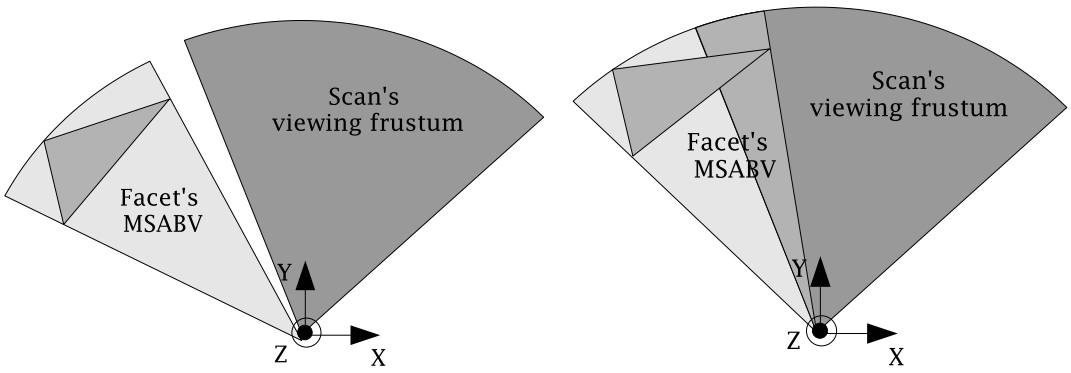

(a) MSABV not intersecting a scan's viewing frustum

(b) MSABV intersecting a scan's viewing frustum

Figure D.2: Illustration of the intersection of a MSABV with a scan's viewing frustum.

```
Data: Facet, ScanFrustum
Result:

with Facet.MSABV as BV

Facet.IsInFrustum ← False
if BV.Above = True then
    if BV.θ_max ≥ ScanFrustum.θ_min then  Facet.IsInFrustum ← True
else if BV.Below = True then
    if BV.θ_min ≤ ScanFrustum.θ_max then  Facet.IsInFrustum ← True
else if BV.Inverted = True then
    if ScanFrustum.Inverted = True then
        if BV.θ_min ≤ ScanFrustum.θ_max and BV.θ_max ≥ ScanFrustum.θ_min then
            Facet.IsInFrustum ← True
        end
    else
        if BV.φ_min ≥ ScanFrustum.φ_min or BV.φ_max ≤ ScanFrustum.φ_max then
            if BV.θ_min ≤ ScanFrustum.θ_max and BV.θ_max ≥ ScanFrustum.θ_min then
                Facet.IsInFrustum ← True
            end
        end
    end
else
    if ScanFrustum.Inverted = True then
        if BV.φ_min ≤ ScanFrustum.φ_min or BV.φ_max ≥ ScanFrustum.φ_max then
            if BV.θ_min ≤ ScanFrustum.θ_max and BV.θ_max ≥ ScanFrustum.θ_min then
                Facet.IsInFrustum ← True
            end
        end
    else
        if BV.φ_min ≤ ScanFrustum.φ_max and BV.φ_max ≥ ScanFrustum.φ_min then
            if BV.θ_min ≤ ScanFrustum.θ_max and BV.θ_max ≥ ScanFrustum.θ_min then
                Facet.IsInFrustum ← True
            end
        end
    end
end
```

Algorithm 21: Procedure *CalculateFacetIsInFrustum* calculating whether the MSABV of a STL facet, and consequently the facet itself, intersects the scan's viewing frustum.

It can be noted that a STL object intersects a scan's viewing frustum if at least one of its facets intersects it. The calculation of whether a STL object intersects a scan's viewing frustum can thus be simply performed after the calculations for all its facets have been performed. Its algorithmic implementation is presented in Algorithm 22.

```
Data: Object
Result:

Object.IsInFrustum ← False
for each Object.Facet do
    if Object.Facet.IsInFrustum = True then
        Object.IsInFrustum ← False
    end
end
```

Algorithm 22: Procedure *CalculateObjectIsInFrustum* calculating whether a STL object intersects the scan's frustum.

D.3 Calculation of the BVH

The resulting algorithmic implementation of the calculation of the pruned BVH is presented in Algorithm 23. This calculation only depends on the scan-referenced 3D model and the scan's frustum. As a result, it can be performed prior to the calculation of the as-planned range point cloud, as shown in Algorithm 3.

It can be noted that Algorithm 12, calculating the MSABV of a facet and called by Algorithm 23, requires the parameter *Incr* as input. The need for this parameter and its estimation are described in Appendix C.

```
Data: Model, ScanFrustum
Result: BVH

DEFINE Incr

Calculate the MSABV and culling properties of STL facets and objects:
for each Model.Object do
    for each Model.Object.Facet do
        CalculateFacetisFrontFacing(Model.Object.Facet)     // see Algorithm 19
        CalculateFacetMSABV(Model.Object.Facet, Incr)
                                              // see Algorithm 12 in Appendix C
        CalculateFacetIsInFrustum(Model.Object.Facet, ScanFrustum)        // see
        Algorithm 21
    end
    CalculateObjectMSABV(Model.Object)      // see Algorithm 16 in Appendix C
    CalculateObjectIsInFrustum(Model.Object)              // see Algorithm 22
end

Calculate the BVH of the 3D model:
for each Model.Object do
    if Model.Object.IsInFrustum = True then
        AddObjectNodeToBVH (BVH,Model.Object)
        for each Model.Object.Facet do
            if Model.Object.Facet.IsFrontFacing = True then
                if Model.Object.Facet.IsInFrustum = True then
                    AddFacetNodeToBVHObject (BVH.Object, Model.Object.Facet)
                end
            end
        end
    end
end
```

Algorithm 23: Function *CalculateBVH* calculating the pruned BVH of the STL-formatted 3D model.

Appendix E

Containment of a Ray in a Minimum Spherical Angular Bounding Volume (MSABV).

This Appendix describes the calculation to test whether a ray corresponding to the scanning direction of an as-planned range point is contained in a minimum spherical angular bounding volume (MSABV) (of a STL facet or object). The calculation differs when the MSABV falls into one of the different cases identified in Appendix C: *Regular*, *Above*, *Below*, *Inverted*.

In the case a MSABV falls in the *Regular* case, as illustrated in Figure E.1, the scanning direction of an as-planned range point, P_P, is contained in this MSABV if, and only if:

1. The pan angle of the point scanning direction, $P_P.\varphi$, verifies:

$$P_P.\varphi \geq MSABV.\varphi_{min} \quad \textbf{and} \quad P_P.\varphi \leq MSABV.\varphi_{max}$$

2. And, the tilt angle of the point scanning direction, $P_P.\theta$, verifies:

$$P_P.\theta \geq MSABV.\theta_{min} \quad \textbf{and} \quad P_P.\theta \leq MSABV.\theta_{max}$$

Similarly, in the case a MSABV falls into the *Inverted* case, as illustrated in Figure E.2, the scanning direction of an as-planned range point, P_P, is contained in this MSABV if, and only if:

$$(P_P.\varphi \leq MSABV.\varphi_{min} \quad \textbf{or} \quad P_P.\varphi \geq MSABV.\varphi_{max}) \quad \textbf{and}$$

$$(P_P.\theta \geq MSABV.\theta_{min} \quad \textbf{and} \quad P_P.\theta \leq MSABV.\theta_{max})$$

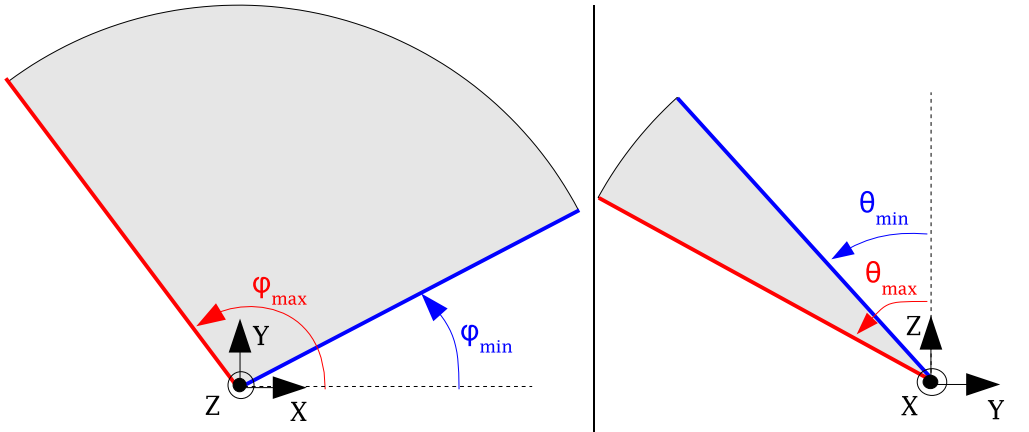

(a) Top view.

(b) Side View: Projection of the MSABV by rotation around the z axis on one quadrant of the (YZ) plane.

Figure E.1: Illustration of a MSABV in the *Regular* category.

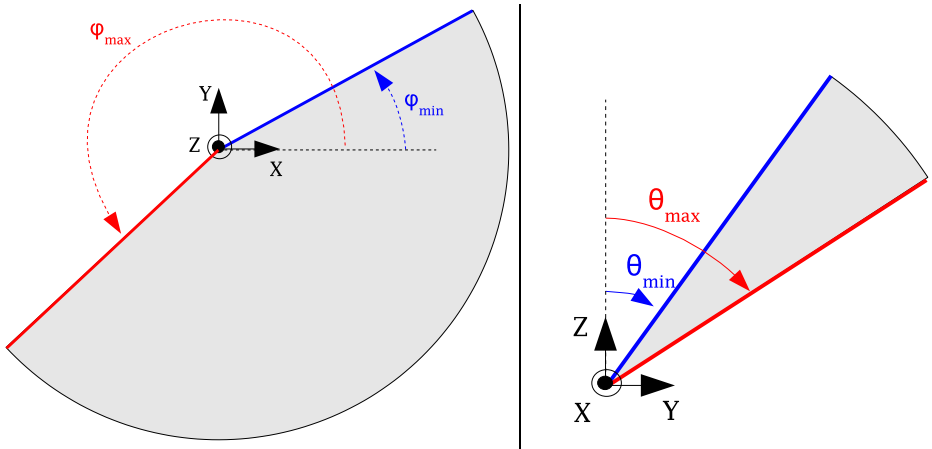

(a) Top view.

(b) Side View: Projection of the MSABV by rotation around the z axis on one quadrant of the (YZ) plane.

Figure E.2: Illustration of the case where a MSABV has *Inverted* bounding pan angles.

In the case a MSABV falls into the *Above* case, as illustrated in Figure E.3(a), the scanning direction of an as-planned range point, P_P, is contained in this MSABV if, and only if:

$$P_P.\theta \leq MSABV.\theta_{max} \qquad \text{(no constraint on the pan angle)}$$

Finally, in the case a MSABV falls into the *Below* case, as illustrated in Figure E.3(b), the scanning direction of an as-planned range point, P_P, is contained in this MSABV if, and only if:

$$P_P.\theta \geq MSABV.\theta_{min} \qquad \text{(no constraint on the pan angle)}$$

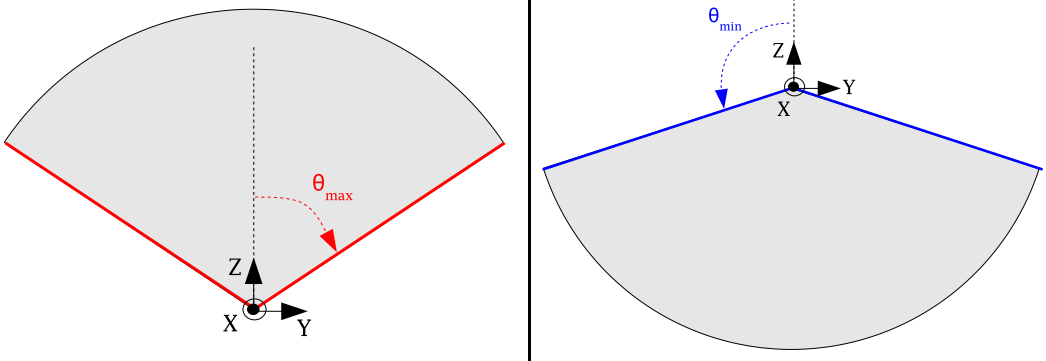

(a) Above case. Side View: Projection of the MSABV by rotation around the z axis on the (YZ) plane.

(b) Below case. Side View: Projection of the MSABV by rotation around the z axis on the (YZ) plane.

Figure E.3: Illustration of the case where a MSABV is *Above* (a) or *Below* (b) the scanner.

The overall algorithmic implementation of the calculation to test whether the scanning direction of an as-planned range point is contained in a MSABV is provided in Algorithm 24.

```
Data: P_P, MSABV
Result: IsSurrounded

IsSurrounded ← False

if MSABV.Above = True then
    if P_P.θ ≤ MSABV.θ_max then
        IsSurrounded ← True
    end
else if MSABV.Below = True then
    if P_P.θ ≥ MSABV.θ_min then
        IsSurrounded ← True
    end
else if MSABV.Inverted = True then
    if P_P.φ ≥ MSABV.φ_max or P_P.φ ≤ MSABV.φ_min then
        if P_P.θ ≥ MSABV.θ_min and P_P.θ ≤ MSABV.θ_max then
            IsSurrounded ← True
        end
    end
else
    if P_P.φ ≥ MSABV.φ_min and P_P.φ ≤ MSABV.φ_max then
        if P_P.θ ≥ MSABV.θ_min and P_P.θ ≤ MSABV.θ_max then
            IsSurrounded ← True
        end
    end
end
```

Algorithm 24: Function *IsRayInMSABV* calculating whether the scanning direction of as-planned range point is contained in a MSABV.

Appendix F

Calculation of the Range of the Intersection Point of a Ray and a STL Facet

In this appendix, we describe the calculation of the range, ρ', of the intersection point of the scanning direction of an as-planned range point with a STL facet. The intersection point may not necessarily exist.

This problem can be seen as a constrained version of the linear projection of a point (here the scan's origin) on the plane defined by the STL facet in a given direction (here the scanning direction of the as-planned range point). The constraint is that the sub-ensemble on which the point is projected, the STL facet, is bounded. Figure F.1 illustrates this problem.

This problem can be solved using the following two-step process for which the algorithmic implementation is presented in Algorithm 25:

Projection. Project the scan's origin as P_{Proj} on the 2D plane defined by the STL facet along the scanning direction of the investigated as-planned range point. This is a simple projection problem that won't be described here. Its algorithmic implementation is simply included in Algorithm 25.

Constraint. Assess whether the projected point, P_{Proj}, is within the boundaries of the STL facet. If the point is within the boundaries, its range, ρ' is calculated. If it is not, it is assigned an infinite range. A method for identifying whether the projected point is within the boundaries of the STL facet is presented in the following section.

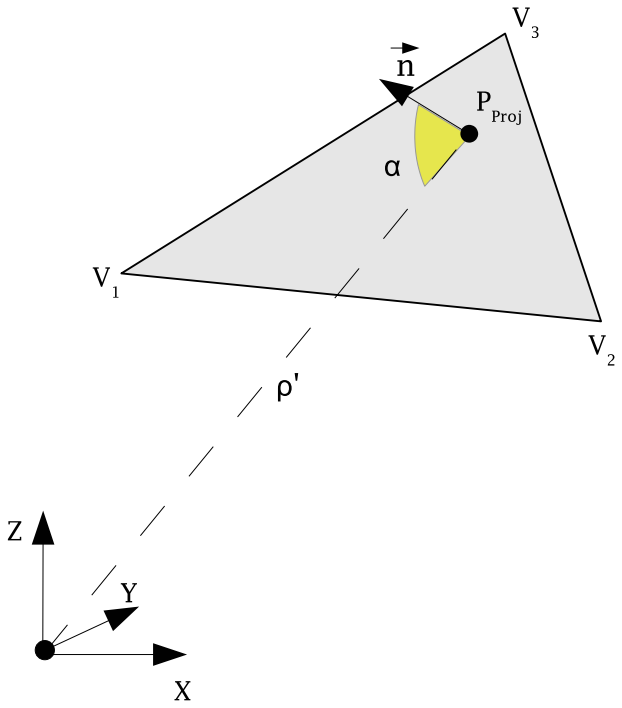

Figure F.1: Illustration of the calculation of the intersection of the scanning direction of an as-planned range point with a STL facet.

Data: Facet, P_B
Result: ρ'

$\overrightarrow{u_P} \leftarrow \frac{1}{\left\|\overrightarrow{P_B}\right\|}\overrightarrow{P_B}$
$\alpha \leftarrow -\overrightarrow{u_P} \cdot \mathsf{Facet}.\overrightarrow{n}$
$P_{Proj}.[x,y,z] \leftarrow P_B.[x,y,z] + \frac{\left(\overrightarrow{P_B - \mathsf{Facet.Vertex}_1} \cdot \mathsf{Facet}.\overrightarrow{n}\right)}{\cos\alpha}\overrightarrow{u_P}$
if `IsPointInsideFacet(`Facet, P_{Proj}`)` = True **then** `// see Algorithm 26`
  $\rho' \leftarrow \sqrt{(P_{Proj}.x)^2 + (P_{Proj}.y)^2 + (P_{Proj}.z)^2}$
else
  $\rho' \leftarrow \infty$
end

Algorithm 25: Function *CalculateIntersectionPointRange* calculating whether a point projected on a 2D surface is inside the STL triangle defining that surface.

F.1 Is Projected Point Inside Facet?

One simple approach to assess whether the projected point, P_{Proj}, is within the boundaries of the STL facet is the following. It uses the fact that each facet edge is a section of the line that is the intersection of the plane defined by the facet and a

second plane perpendicular to the first one. Figure F.2 illustrates the three planes, perpendicular to the plane defined by a STL facet, that define the three edges of the facet. Each of these three planes is simply defined by a point, $Plane.Pt$, that can be set to one of the facet's vertices, and a normal vector, $Plane.\overrightarrow{n}$, that can easily be computed based on the facet's vertices and normal vector. For instance, $Plane_1.Pt$ and $Plane_1.\overrightarrow{n}$ of the plane $Plane_1$ defining the edge between the vertices $Facet.V_1$ and $Facet.V_2$ of a STL facet, are calculated as:

$$\begin{aligned} Plane_1.Pt &= Facet.V_1 \\ Plane_1.\overrightarrow{n} &= (Facet.V_2 - Facet.V_1) \times Facet.\overrightarrow{n} \end{aligned}$$

The formula used for $Plane_1.\overrightarrow{n}$ assumes that the normal vector to the STL facet points toward the outside of the object, which is consistent with the previous assumptions on the matter. Again, this can be ensured during the conversion of the 3D model into STL format (see Appendix A).

Then, the projected point, P_{Proj}, is inside the facet if, and only if:

$$\begin{aligned} &(P_{Proj} - Facet.V_1) \cdot Plane_1.\overrightarrow{n} \leq 0 \quad \textbf{and} \\ &(P_{Proj} - Facet.V_2) \cdot Plane_2.\overrightarrow{n} \leq 0 \quad \textbf{and} \\ &(P_{Proj} - Facet.V_3) \cdot Plane_3.\overrightarrow{n} \leq 0 \end{aligned}$$

The algorithmic implementation of this calculation is presented in Algorithm 26.

```
Data: Facet, P_Proj
Result: IsInside

IsInside ← False

if (P_Proj − Facet.Vertex_1.XYZ) · Facet.Vertex_1.n ≤ 0 then
    if (P_Proj − Facet.Vertex_2.XYZ) · Facet.Vertex_2.n ≤ 0 then
        if (P_Proj − Facet.Vertex_3.XYZ) · Facet.Vertex_3.n ≤ 0 then
            IsInside ← True
        end
    end
end
```

Algorithm 26: Function *IsPointInsideFacet* calculating whether a point projected on a 2D surface is inside the STL triangle defining that surface.

Note that the vectors normal to the planes $Plane_1$, $Plane_2$ and $Plane_3$ can be calculated as soon as the 3D model is converted into STL format, and then

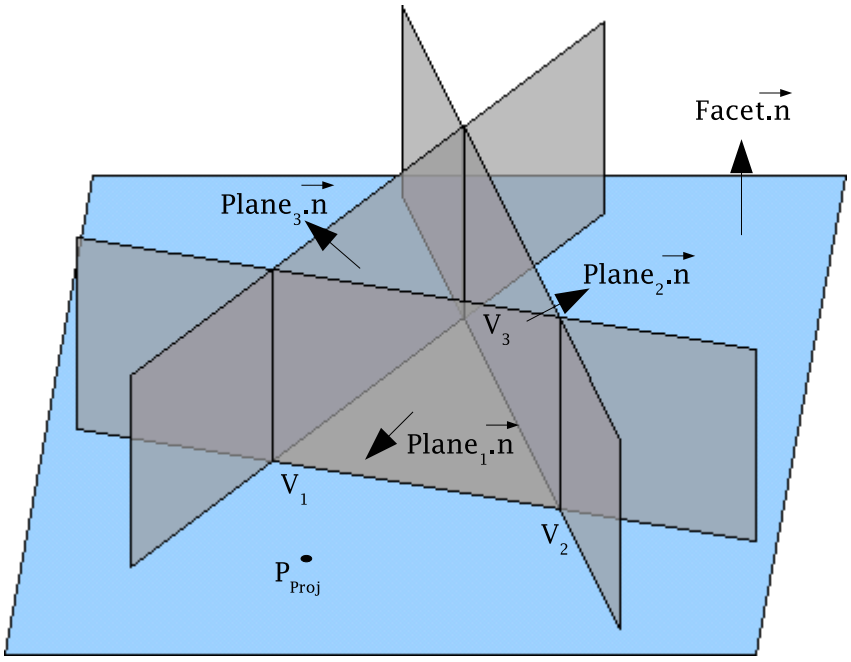

(a) Perspective view.

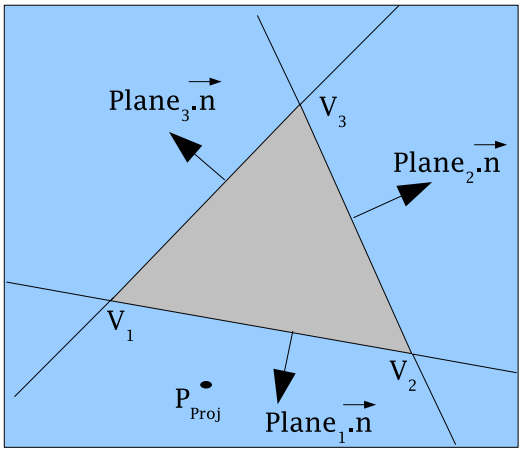

(b) Topview.

Figure F.2: Illustration of the calculation of whether a point on the plane defined by a STL facet is inside the facet.

scan-referenced with the rest of the model during *Step 2* of the developed object recognition process. The algorithmic implementation of the calculation of the vectors normal to the planes $Plane_1$, $Plane_2$ and $Plane_3$ of a STL facet is presented in Algorithm 27, and this algorithm is called in Algorithm 1 as soon as the 3D model has been converted into STL format. Note that the normal vector of the plane i is simply assigned to the vertex i. The scan-referencing of the vectors normal to the planes $Plane_1$, $Plane_2$ and $Plane_3$ of each facet in the scan's coordinate frame is

included in Algorithm 2.

```
Data: Model
Result:

for each Model.Object do
    for each Model.Object.Facet As F do
        for i = 1 to 3 do
            j ← i + 1
            if j = 4 then j ← 1
            F.Vertex_i.n⃗ ← (F.Vertex_j − F.Vertex_i) × F.n⃗
        end
    end
end
```

Algorithm 27: Procedure *CalculateVerticesNormals* calculating the normals of the planes perpendicular to the plane of a STL facet and defining its three edges.

Appendix G

Object Recognition Results of Experiment 3

This Appendix presents the different data sets (model and scan) at the different steps of the recognition process obtained in *Experiment 3* described in Chapter 4. A table with the detailed object recognition statistics for each of the 612 objects of the 3D model is also provided at the end of this appendix.

G.1 Input Data

The experiment's input data consists of the 3D CAD model of the building's structure and the laser scan *Scan 3* presented in Chapter 4. The 3D CAD model is presented in Figure G.1. It contains 612 objects including large objects, such as columns and beams, and small objects, such wall panel braces or hand rail tubes. *Scan 3* is presented in Figure G.2. It contains $810,399$ range points and has a scan angular resolution of $582\,\mu rad$ in pan and $582\,\mu rad$ in tilt.

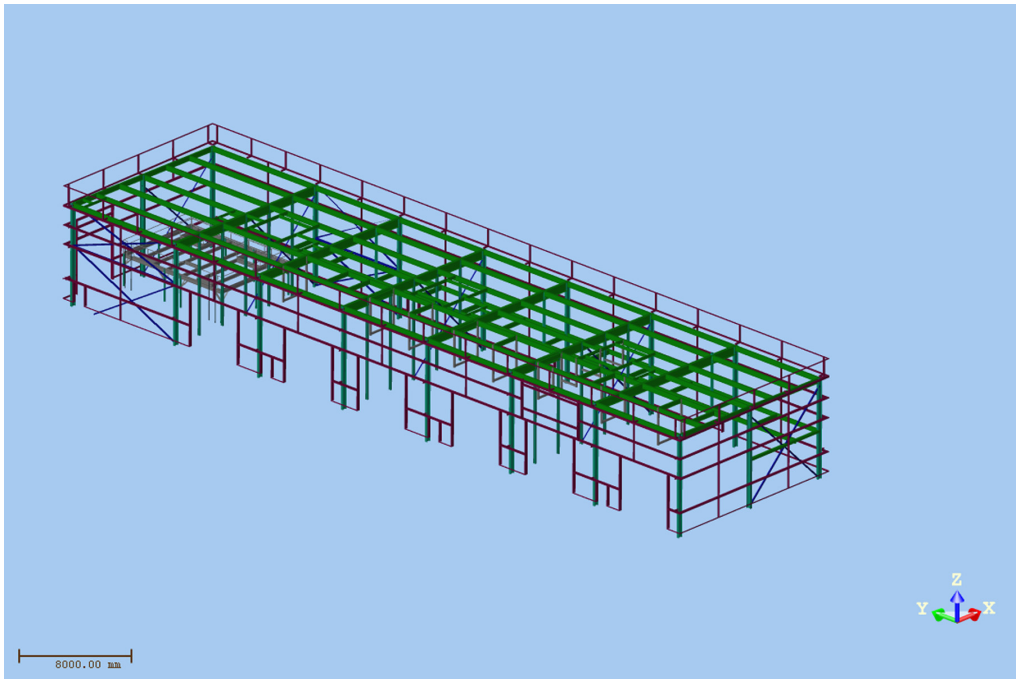

Figure G.1: 3D CAD model.

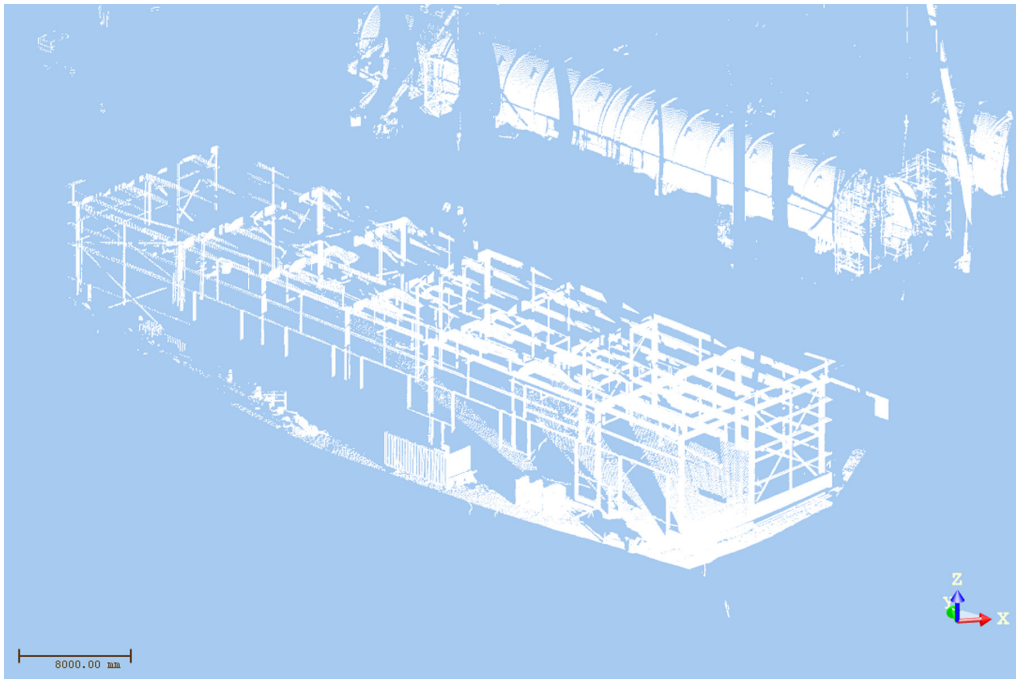

Figure G.2: As-built 3D laser scanned point cloud.

G.2 Recognition Process Results

G.2.1 Step 1 - Convert 3D model

The first step of the recognition process is to convert the 3D CAD model into STL format. Figure G.3 presents the STL-formatted model that contains 19,478 facets — an average of about 32 facets per object. It can be seen that the 3D CAD model is faithfully converted.

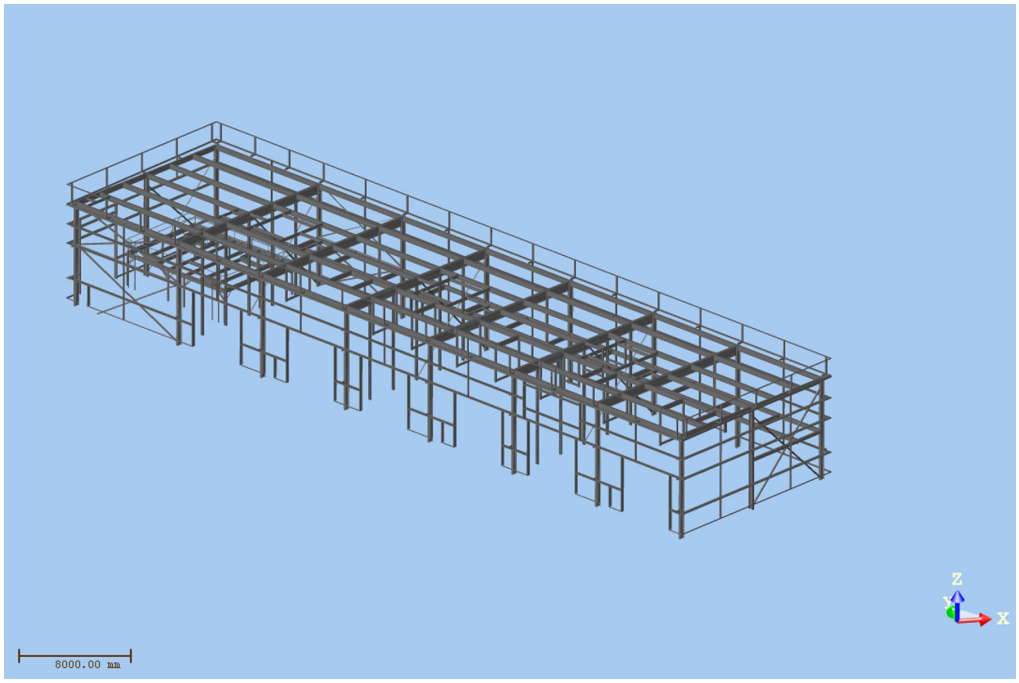

Figure G.3: STL-formatted 3D model.

G.2.2 Step 2 - 3D model Scan-Referencing

The second step of the recognition process uses the 3D model and scan registration information to reference the STL-formatted 3D model in the scan's spherical coordinate frame. Figure G.4 shows the 3D model and *Scan 3* in the scan's spherical coordinate frame.

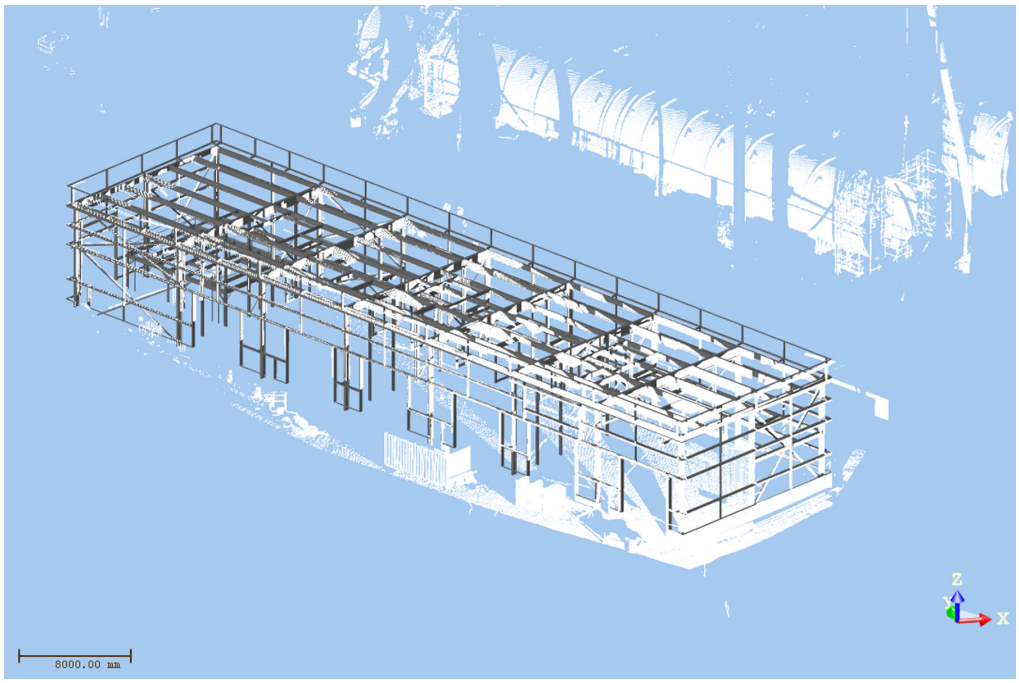

Figure G.4: 3D model referenced in the scan's spherical coordinate frame.

G.2.3 Step 3 - Calculate As-planned Range Point Cloud

The third and main step of the recognition process is the calculation of the as-planned range point cloud. Figure G.5 presents the calculated as-planned point cloud corresponding to *Scan 3*.

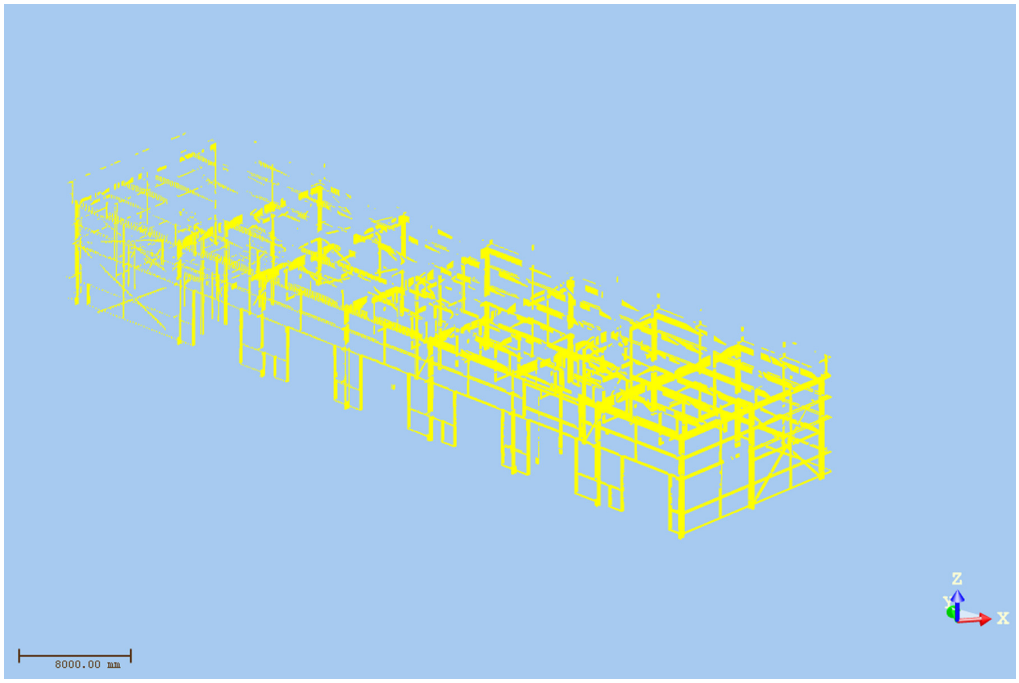

Figure G.5: As-planned range point cloud corresponding to *Scan 3*.

G.2.4 Step 4 - Recognize Points

The fourth step of the process is the recognition of the range points by comparing each pair of as-built and as-planned points. For this, the automatically calculated $\Delta\rho_{max}$ threshold is used. In the case of this scan, $\Delta\rho_{max}$ is automatically calculated as equal to 79.57 mm. Figure G.6 displays the as-planned points from Figure G.5 that are recognized. Note that a large portion of them is recognized.

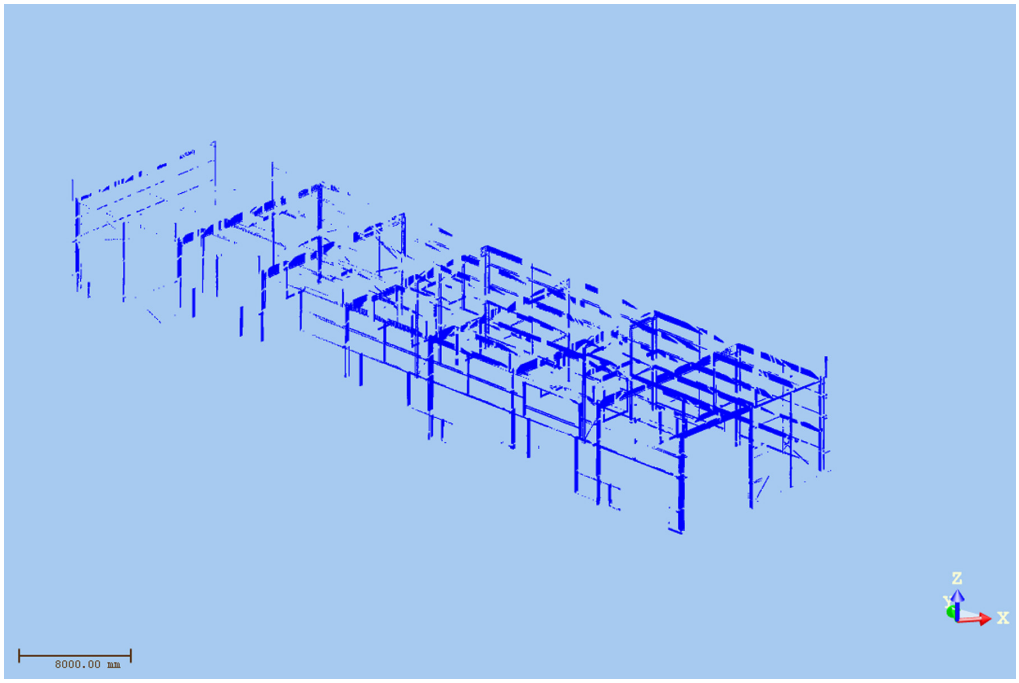

Figure G.6: Points recognized in Scan 3.

G.2.5 Step 5 - Recognize Objects

The fifth and last step of the process is the recognition of the model objects by comparing, for each object, the covered surface of its recognized as-planned points with the automatically calculated threshold $Surf_{min}$. Here, $Surf_{min}$ is automatically calculated as equal to $0.0109\,m^2$. Figure G.7 displays the objects from the 3D model that are recognized in the scan. The colors used in Figure G.7 have the following meaning:

Gray: The object is not expected (planned) to be recognized in this scan — because the covered surface of its as-planned points does not exceed $Surf_{min}$.

Green: The object is expected to be recognized and is recognized in the scan.

Red: The object is expected to be recognized but is not recognized in the scan. This must, however, not lead to the conclusion that the object is not built. Several situations must in fact be distinguished.

The object is in the scan. It is then colored in red because it is built, but at the wrong location.

The object is not in the scan. This may occur in three different situations:

- The construction is behind schedule.
- Inadequate 3D model: the search 3D model does not adequately represent the project in the state it is expected to be found.
- External occlusions: the object is occluded by another object that is not part of the 3D model (*e.g.* piece of equipment).

Since, an object colored in red may mean different things, it must be interpreted as a *warning* saying that this particular object requires further analysis. Note that, the last two of the four situations identified above can be somewhat avoided using good practice. First, an adequate *as-planned 3D model* can be used for the object recognition by using a project 4D model instead of the 3D model (see Section 5.2.3). Then, external occlusions (occlusions to non-model objects) can be avoided by cleaning the scanned scene prior to conduct any scan as well as locating the scanner so that external occlusions that cannot be removed are minimized (see Section 5.2.3). If these best practices are implemented, an object colored in red will then indicate either that it is built at the wrong location, or that construction is behind schedule, the first case being easily identifiable by investigating the scan manually.

It can be seen in Figure G.7 that most of the 3D model objects (exactly 466 objects) are expected to be recognized in the investigated scan. Out of these, a majority of them (exactly 280 objects) is actually recognized in the scan. While it can be noted that the main structural elements are well recognized, 186 elements still are not recognized (colored in red). As mentioned above, these objects may not be recognized for several reasons. For instance, the 131 objects constituting the small inner structure at the back of the building (see Figure G.1) should not have been included in the 3D model considering the current level of progress.

Then, the small elements around two of the door frames in the front long wall are not recognized because they were occluded by other non-model objects such as a set of portable toilets (external occlusions).

Next, the three door frames colored in red in the front long side (6 objects) are not recognized but are in the scan (see Figure G.2). It can thus be concluded that they are likely built at the wrong location, or design change orders have not been reported to the 3D model.

Finally, many of the objects the furthest from the scanner are not recognized although they are present in the scan. These objects include 5 fairly large beams and the column in the middle of the back side of the building. An important reason why they are not recognized is that, from the scanner's location, they are highly occluded by other model objects, so that only small parts of their total surfaces were actually expected to be recognized in the scan, and their recognized surfaces often simply fell short of the $Surf_{min}$ threshold. It is also likely that poor registration quality negatively impacted their recognition.

Detailed statistics about the recognition of each 3D model object are provided in the next section.

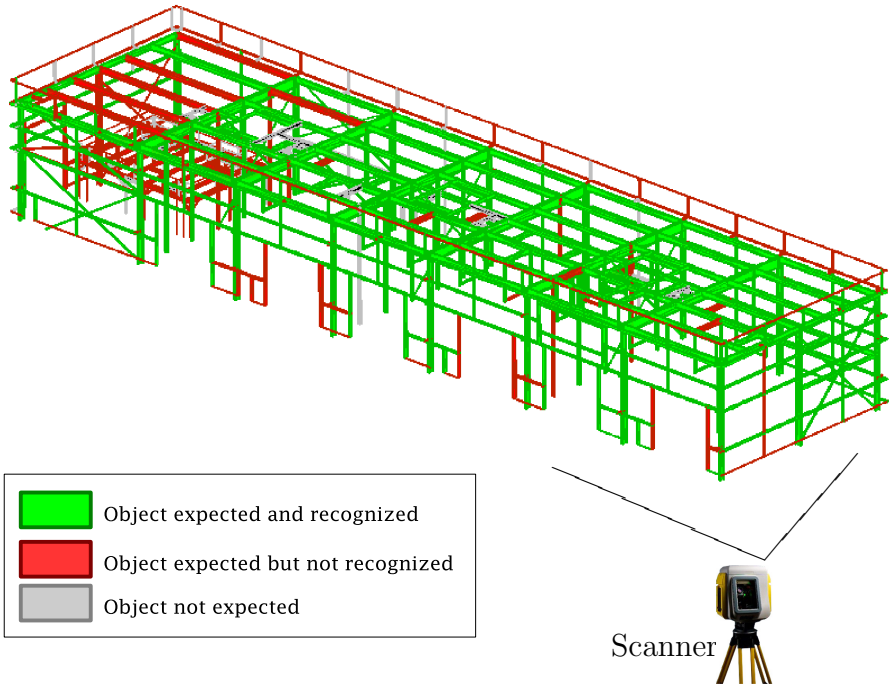

Figure G.7: The 3D model object recognition results obtained with *Scan 3*.

G.2.6 Recognition Statistics

Table G.1 summarizes the recognition statistics obtained for each of the 612 objects composing the original 3D CAD model. In this table, the column values are:

Column 1: *ID* of the object.

Column 2: Number of points in the object's as-planned range point cloud.

Column 3: Number of points in the object's as-planned range point cloud that are recognized.

Column 4: Covered Surface of the points in the object's as-planned range point cloud.

Column 5: Covered Surface of the points in the object's as-planned range point cloud that are recognized.

Column 6: Whether the object is considered *planned* (1) or not (0). It is considered planned if the covered Surface of the points in the object's as-planned range point cloud (column 4) is larger than $Surf_{min}$.

Column 7: Whether the object is recognized (1) or not (0). Note that an object can be recognized only if it is planned (the covered surface of the recognized as-planned range points cannot exceed the covered surface of all the as-planned range points).

Column 8: Whether the object is manually visually identified (1) or not (0) in the scan.

Table G.1: Recognition Statistics for Scan 3.

Object ID	Planned Points	Recog. Points	Planned Surface (m^2)	Recog. Surface (m^2)	Planned	Recog.	Actual
1	5071	281	1.31	0.06	1	1	1
2	2240	514	1.89	0.3	1	1	1
3	4477	60	1.23	0.02	1	1	1
4	4868	29	1.35	0.01	1	0	1
5	4324	0	1.09	0	1	0	1
6	6456	48	1.21	0.01	1	0	1
7	1737	1401	0.49	0.39	1	1	1
8	1765	1314	0.52	0.36	1	1	1
9	215	33	0.1	0.02	1	1	0
10	500	498	0.12	0.12	1	1	1
11	457	40	0.1	0.01	1	0	1
12	67	6	0.02	0	1	0	1
13	260	42	0.04	0.01	1	0	1
14	81	7	0.04	0.01	1	0	1
15	28	2	0.02	0	1	0	0
16	41	0	0.04	0	1	0	0
17	12	0	0.01	0	1	0	0
18	8	2	0.01	0	1	0	0
19	6	2	0.01	0	1	0	0
20	2411	12	1.35	0.01	1	0	1
21	1940	0	1.19	0	1	0	1
22	1657	1022	1.21	0.7	1	1	1
23	1484	797	1.47	0.65	1	1	1
24	1199	0	1.15	0	1	0	1
25	1091	0	1.21	0	1	0	1
26	739	506	0.56	0.31	1	1	1
27	717	575	0.61	0.46	1	1	1
28	298	0	0.37	0	1	0	0
29	329	0	0.36	0	1	0	0
30	109	38	0.21	0.07	1	1	1
31	218	80	0.8	0.15	1	1	1
32	5	0	0.07	0	1	0	0
33	860	420	1.62	0.86	1	1	1
34	768	356	1.09	0.5	1	1	1
35	88	0	0.91	0	1	0	0
36	31	0	0.2	0	1	0	0
37	54	4	0.11	0.01	1	0	0
38	61	0	0.23	0	1	0	0
39	19	0	0.1	0	1	0	0
40	80	0	0.19	0	1	0	0
41	192	0	0.23	0	1	0	0
42	326	30	0.2	0.02	1	1	0
43	53	0	0.2	0	1	0	0
44	161	6	0.19	0.01	1	0	1

Continued on next page...

Table G.1 – continued from previous page

Object ID	Planned Points	Recog. Points	Planned Surface (m^2)	Recog. Surface (m^2)	Planned	Recog.	Actual
45	723	146	0.3	0.07	1	1	1
46	167	45	0.29	0.1	1	1	1
47	60	0	0.28	0	1	0	0
48	6245	2587	3.87	1.58	1	1	1
49	78	2	0.65	0.02	1	1	1
50	51	8	0.03	0	1	0	0
51	32	4	0.02	0	1	0	0
52	47	6	0.03	0	1	0	1
53	4	0	0	0	0	0	0
54	25	7	0.03	0.01	1	0	1
55	1	0	0	0	0	0	0
56	19	4	0.04	0.01	1	1	0
57	0	0	0	0	0	0	0
58	207	138	0.03	0.02	1	1	1
59	202	102	0.03	0.02	1	1	1
60	133	88	0.03	0.02	1	1	1
61	116	56	0.03	0.02	1	1	1
62	71	41	0.03	0.02	1	1	1
63	78	25	0.03	0.01	1	1	1
64	57	34	0.03	0.02	1	1	1
65	50	12	0.03	0.01	1	0	1
66	41	22	0.03	0.02	1	1	1
67	38	7	0.03	0.01	1	0	1
68	29	13	0.03	0.01	1	1	1
69	29	3	0.03	0	1	0	1
70	24	10	0.03	0.02	1	1	1
71	5	5	0.01	0.01	0	0	0
72	25	0	0.03	0	1	0	1
73	10	0	0.01	0	1	0	0
74	0	0	0	0	0	0	0
75	68	0	0.03	0	1	0	0
76	66	0	0.04	0	1	0	0
77	62	0	0.04	0	1	0	0
78	58	0	0.04	0	1	0	0
79	44	0	0.03	0	1	0	0
80	0	0	0	0	0	0	0
81	28	0	0.03	0	1	0	0
82	30	0	0.04	0	1	0	0
83	0	0	0	0	0	0	0
84	18	0	0.03	0	1	0	0
85	0	0	0	0	0	0	0
86	10	0	0.02	0	1	0	0
87	0	0	0	0	0	0	0
88	0	0	0	0	0	0	0
89	0	0	0	0	0	0	0
90	0	0	0	0	0	0	0
91	2	0	0.01	0	0	0	0
92	0	0	0	0	0	0	0
93	0	0	0	0	0	0	0
94	0	0	0	0	0	0	0
95	168	60	0.02	0.01	1	1	1
96	92	0	0.03	0	1	0	1
97	107	9	0.03	0	1	0	0
98	101	70	0.02	0.02	1	1	1
99	151	56	0.03	0.01	1	0	0
100	15	0	0.03	0	1	0	0
101	546	0	0.18	0	1	0	0

Continued on next page...

Table G.1 – continued from previous page

Object ID	Planned Points	Recog. Points	Planned Surface (m^2)	Recog. Surface (m^2)	Planned	Recog.	Actual
102	528	255	0.24	0.11	1	1	1
103	448	254	0.22	0.11	1	1	1
104	0	0	0	0	0	0	0
105	7	0	0.03	0	1	0	0
106	3	0	0.01	0	0	0	0
107	17	0	0.03	0	1	0	0
108	0	0	0	0	0	0	0
109	0	0	0	0	0	0	0
110	0	0	0	0	0	0	0
111	37	0	0.06	0	1	0	0
112	0	0	0	0	0	0	0
113	42	0	0.04	0	1	0	0
114	132	0	0.11	0	1	0	0
115	63	0	0.05	0	1	0	0
116	172	0	0.11	0	1	0	0
117	212	0	0.12	0	1	0	0
118	0	0	0	0	0	0	0
119	49	0	0.07	0	1	0	0
120	6678	3081	1.75	0.78	1	1	1
121	6644	175	8.86	0.17	1	1	1
122	101	0	0.2	0	1	0	0
123	95	0	0.04	0	1	0	1
124	192	0	0.06	0	1	0	1
125	688	0	0.46	0	1	0	1
126	36	20	0.11	0.04	1	1	1
127	2	0	0	0	0	0	0
128	0	0	0	0	0	0	0
129	38	29	0.07	0.06	1	1	1
130	64	4	0.12	0.01	1	0	0
131	46	7	0.21	0.02	1	1	0
132	91	67	0.14	0.1	1	1	1
133	43	8	0.13	0.01	1	0	0
134	110	75	0.2	0.09	1	1	1
135	55	9	0.11	0.01	1	1	0
136	192	160	0.21	0.16	1	1	1
137	75	16	0.09	0.03	1	1	0
138	245	204	0.19	0.14	1	1	1
139	110	26	0.08	0.02	1	1	0
140	419	345	0.24	0.2	1	1	1
141	182	28	0.09	0.02	1	1	0
142	723	502	0.29	0.19	1	1	1
143	279	50	0.08	0.02	1	1	0
144	1290	1007	0.27	0.21	1	1	1
145	1345	942	0.27	0.18	1	1	1
146	817	727	0.25	0.22	1	1	1
147	1	0	0	0	0	0	0
148	0	0	0	0	0	0	0
149	93	32	0.04	0.01	1	1	0
150	171	72	0.04	0.02	1	1	0
151	207	145	0.05	0.04	1	1	1
152	342	219	0.04	0.03	1	1	1
153	124	83	0.05	0.03	1	1	1
154	78	51	0.05	0.03	1	1	1
155	45	33	0.04	0.03	1	1	1
156	30	19	0.04	0.02	1	1	1
157	29	10	0.04	0.01	1	1	1
158	5	5	0.01	0.01	0	0	0

Continued on next page...

Table G.1 – continued from previous page

Object ID	Planned Points	Recog. Points	Planned Surface (m^2)	Recog. Surface (m^2)	Planned	Recog.	Actual
159	31	14	0.02	0.01	1	0	0
160	35	10	0.02	0	1	0	0
161	27	10	0.02	0.01	1	0	0
162	9	0	0.01	0	0	0	0
163	12	4	0.01	0	1	0	0
164	6	2	0.01	0	0	0	0
165	12	3	0.02	0	1	0	0
166	0	0	0	0	0	0	0
167	7396	335	1.75	0.06	1	1	1
168	162	72	0.03	0.01	1	1	0
169	301	142	0.03	0.02	1	1	0
170	91	21	0.03	0.01	1	0	0
171	65	17	0.03	0.01	1	0	0
172	44	7	0.03	0	1	0	0
173	33	5	0.03	0.01	1	0	0
174	12	1	0.02	0	1	0	0
175	2	1	0	0	0	0	0
176	43	20	0.02	0.01	1	0	0
177	46	15	0.01	0	1	0	0
178	32	12	0.02	0.01	1	0	0
179	5	0	0	0	0	0	0
180	20	9	0.02	0.01	1	0	0
181	5	4	0.01	0.01	0	0	0
182	14	4	0.02	0.01	1	0	0
183	0	0	0	0	0	0	0
184	174	95	0.36	0.2	1	1	1
185	8165	817	2.6	0.08	1	1	1
186	1907	276	1.43	0.2	1	1	1
187	1715	1421	2.33	2.1	1	1	1
188	933	889	2.21	2.1	1	1	1
189	554	107	2.1	0.14	1	1	1
190	352	8	1.96	0.05	1	1	1
191	274	18	2.32	0.21	1	1	1
192	5353	4055	2.25	1.8	1	1	1
193	2532	2142	1.82	1.64	1	1	1
194	811	533	0.91	0.63	1	1	1
195	834	811	1.45	1.41	1	1	1
196	225	119	0.58	0.32	1	1	1
197	135	73	0.48	0.29	1	1	1
198	93	4	0.4	0.01	1	0	1
199	3297	2382	1.41	1.03	1	1	1
200	1753	1241	1.23	0.9	1	1	1
201	368	204	0.38	0.2	1	1	1
202	521	472	0.9	0.83	1	1	1
203	55	38	0.14	0.1	1	1	1
204	0	0	0	0	0	0	1
205	11254	8752	2.32	1.93	1	1	1
206	6666	481	2.45	0.09	1	1	1
207	414	305	0.83	0.61	1	1	1
208	343	124	0.74	0.26	1	1	1
209	21820	16715	4.23	3.14	1	1	1
210	10453	7216	3.83	2.12	1	1	1
211	4466	2918	2.88	1.91	1	1	1
212	3669	3214	3.54	3.11	1	1	1
213	1802	1070	2.82	1.7	1	1	1
214	1410	957	2.32	1.33	1	1	1
215	1083	647	2.65	1.74	1	1	1

Continued on next page...

Table G.1 – continued from previous page

Object ID	Planned Points	Recog. Points	Planned Surface (m^2)	Recog. Surface (m^2)	Planned	Recog.	Actual
216	1037	671	2.77	1.54	1	1	1
217	87	3	0.19	0.01	1	0	1
218	372	90	1.15	0.27	1	1	1
219	1451	1014	3.42	2.46	1	1	1
220	1480	531	2.69	1.1	1	1	1
221	2607	932	3.84	1.78	1	1	1
222	3254	556	3.69	0.81	1	1	1
223	4433	2031	3.67	1.85	1	1	1
224	14000	7013	4.1	1.94	1	1	1
225	18918	11754	6.7	4.12	1	1	1
226	8723	6692	4.17	3.34	1	1	1
227	5283	4525	3.56	3.01	1	1	1
228	3816	3176	3.49	2.89	1	1	1
229	3535	2972	4.22	3.55	1	1	1
230	2768	2248	4.25	3.47	1	1	1
231	5043	4368	2.09	1.86	1	1	1
232	3640	3328	2.48	2.32	1	1	1
233	1408	1036	1.7	1.33	1	1	1
234	1048	858	1.76	1.48	1	1	1
235	296	138	0.83	0.37	1	1	1
236	604	45	2.3	0.11	1	1	1
237	95	78	0.16	0.13	1	1	1
238	45	9	0.06	0.01	1	1	1
239	86	3	0.09	0	1	0	1
240	296	55	0.25	0.05	1	1	1
241	371	145	0.24	0.09	1	1	1
242	474	88	0.24	0.04	1	1	1
243	3213	112	1.15	0.05	1	1	1
244	143	0	0.22	0	1	0	1
245	0	0	0	0	0	0	0
246	216	51	0.2	0.05	1	1	1
247	19	0	0.01	0	1	0	1
248	479	0	0.28	0	1	0	1
249	573	50	0.28	0.02	1	1	1
250	1920	986	1.06	0.55	1	1	1
251	440	5	0.46	0.01	1	0	1
252	425	185	0.89	0.28	1	1	1
253	446	2	0.72	0	1	0	1
254	798	325	1.36	0.55	1	1	1
255	7	0	0.02	0	1	0	0
256	953	47	1.49	0.07	1	1	0
257	827	317	1.26	0.48	1	1	1
258	2625	115	0.75	0.05	1	1	1
259	2701	266	0.87	0.07	1	1	1
260	70	2	0.15	0	1	0	1
261	88	2	0.19	0	1	0	1
262	1441	1095	1.47	1.08	1	1	1
263	1369	977	1.42	1.01	1	1	1
264	664	435	0.77	0.5	1	1	1
265	193	35	0.2	0.03	1	1	1
266	0	0	0	0	0	0	0
267	3246	2569	1.86	1.44	1	1	1
268	61	0	0.04	0	1	0	1
269	2030	1550	1.44	1.09	1	1	1
270	2866	59	1.48	0.03	1	1	0
271	526	5	0.25	0	1	0	0
272	7424	6048	2.49	2.2	1	1	1

Continued on next page...

Table G.1 – continued from previous page

Object ID	Planned Points	Recog. Points	Planned Surface (m^2)	Recog. Surface (m^2)	Planned	Recog.	Actual
273	788	680	1.02	0.87	1	1	1
274	137	18	0.48	0.06	1	1	1
275	0	0	0	0	0	0	0
276	65	52	0.26	0.21	1	1	1
277	34	26	0.16	0.12	1	1	1
278	213	0	1.54	0	1	0	1
279	5706	3610	1.74	1.26	1	1	1
280	1983	1136	1.26	0.9	1	1	1
281	493	342	0.49	0.35	1	1	1
282	255	146	0.47	0.35	1	1	1
283	280	105	0.84	0.16	1	1	1
284	301	141	1.37	0.46	1	1	1
285	212	9	1.5	0	1	0	1
286	6230	672	1.92	0.23	1	1	1
287	1237	388	0.93	0.29	1	1	1
288	1069	802	1.27	1.16	1	1	1
289	301	278	0.77	0.71	1	1	1
290	176	81	0.71	0.28	1	1	1
291	116	41	0.72	0.28	1	1	1
292	91	0	0.87	0	1	0	1
293	6453	5034	2.36	1.99	1	1	1
294	1236	954	0.76	0.64	1	1	1
295	1362	1096	1.55	1.36	1	1	1
296	521	493	0.93	0.88	1	1	1
297	367	77	1	0.18	1	1	1
298	101	32	0.43	0.11	1	1	1
299	77	2	0.38	0	1	0	1
300	6305	4937	2.48	2.06	1	1	1
301	2578	2197	1.76	1.59	1	1	1
302	1175	841	1.35	1.03	1	1	1
303	644	587	1.11	1.07	1	1	1
304	278	69	0.74	0.18	1	1	1
305	189	6	0.72	0.01	1	0	1
306	126	6	0.73	0.04	1	1	1
307	0	0	0	0	0	0	0
308	119	0	0.23	0	1	0	0
309	6	0	0.04	0	1	0	0
310	0	0	0	0	0	0	0
311	0	0	0	0	0	0	0
312	0	0	0	0	0	0	0
313	0	0	0	0	0	0	0
314	0	0	0	0	0	0	0
315	0	0	0	0	0	0	0
316	0	0	0	0	0	0	0
317	0	0	0	0	0	0	0
318	0	0	0	0	0	0	0
319	0	0	0	0	0	0	0
320	0	0	0	0	0	0	0
321	68	0	0.24	0	1	0	1
322	219	4	0.85	0.01	1	1	1
323	98	8	0.4	0.02	1	1	1
324	117	11	0.43	0.01	1	0	1
325	219	13	0.86	0.04	1	1	1
326	157	65	0.57	0.22	1	1	1
327	129	59	0.21	0.03	1	1	1
328	116	9	0.21	0.02	1	1	1
329	263	91	0.59	0.09	1	1	1

Continued on next page...

Table G.1 – continued from previous page

Object ID	Planned Points	Recog. Points	Planned Surface (m^2)	Recog. Surface (m^2)	Planned	Recog.	Actual
330	697	93	0.37	0.05	1	1	1
331	1251	48	0.75	0.03	1	1	1
332	234	148	0.35	0.23	1	1	1
333	0	0	0	0	0	0	0
334	44	11	0.2	0.02	1	1	1
335	0	0	0	0	0	0	0
336	111	89	0.2	0.16	1	1	1
337	98	78	0.21	0.17	1	1	1
338	478	320	0.43	0.3	1	1	1
339	155	115	0.11	0.08	1	1	1
340	159	109	0.32	0.24	1	1	1
341	181	153	0.11	0.1	1	1	1
342	98	59	0.07	0.05	1	1	1
343	338	294	0.28	0.27	1	1	1
344	989	628	0.48	0.32	1	1	1
345	1438	1191	0.6	0.5	1	1	1
346	686	577	0.47	0.41	1	1	1
347	294	45	0.29	0.04	1	1	1
348	395	20	0.41	0.02	1	1	1
349	218	7	0.35	0.01	1	1	1
350	287	14	0.49	0.02	1	1	1
351	8001	4539	3.46	1.73	1	1	1
352	5952	3228	3.55	1.89	1	1	1
353	165	0	1.46	0	1	0	1
354	141	42	0.28	0.08	1	1	1
355	57	0	0.3	0	1	0	0
356	18	0	0.04	0	1	0	1
357	2008	1310	4.9	2.09	1	1	1
358	4407	404	1.22	0.1	1	1	1
359	1000	526	0.66	0.43	1	1	1
360	1	0	0	0	0	0	0
361	0	0	0	0	0	0	0
362	0	0	0	0	0	0	0
363	0	0	0	0	0	0	0
364	0	0	0	0	0	0	0
365	0	0	0	0	0	0	0
366	118	100	0.2	0.17	1	1	1
367	114	98	0.25	0.17	1	1	1
368	181	149	0.44	0.26	1	1	1
369	109	18	0.19	0.03	1	1	1
370	157	147	0.21	0.19	1	1	1
371	128	123	0.17	0.16	1	1	1
372	225	180	0.4	0.35	1	1	1
373	226	221	0.4	0.4	1	1	1
374	316	316	0.23	0.23	1	1	1
375	324	321	0.3	0.3	1	1	1
376	439	438	0.37	0.37	1	1	1
377	455	453	0.39	0.39	1	1	1
378	1204	59	0.32	0.02	1	1	0
379	1202	93	0.31	0.03	1	1	0
380	1299	0	0.3	0	1	0	0
381	838	0	0.19	0	1	0	0
382	1316	0	0.3	0	1	0	0
383	826	658	0.29	0.23	1	1	1
384	1486	1093	0.52	0.36	1	1	1
385	945	574	0.33	0.19	1	1	1
386	1194	2	0.28	0	1	0	0

Continued on next page...

Table G.1 – continued from previous page

Object ID	Planned Points	Recog. Points	Planned Surface (m^2)	Recog. Surface (m^2)	Planned	Recog.	Actual
387	897	559	0.32	0.19	1	1	1
388	2073	994	2.44	1.12	1	1	1
389	2640	1310	3	1.5	1	1	1
390	377	82	0.22	0.04	1	1	1
391	349	50	0.2	0.02	1	1	1
392	434	60	0.24	0.03	1	1	1
393	571	164	0.32	0.09	1	1	1
394	325	75	0.23	0.06	1	1	1
395	384	105	0.27	0.07	1	1	1
396	467	79	0.32	0.05	1	1	1
397	420	104	0.29	0.07	1	1	1
398	0	0	0	0	0	0	0
399	0	0	0	0	0	0	0
400	0	0	0	0	0	0	0
401	0	0	0	0	0	0	0
402	164	42	0.17	0.04	1	1	1
403	205	49	0.22	0.05	1	1	1
404	277	62	0.3	0.06	1	1	1
405	234	88	0.26	0.09	1	1	1
406	0	0	0	0	0	0	1
407	0	0	0	0	0	0	1
408	0	0	0	0	0	0	1
409	0	0	0	0	0	0	1
410	0	0	0	0	0	0	0
411	0	0	0	0	0	0	0
412	0	0	0	0	0	0	0
413	0	0	0	0	0	0	0
414	59	44	0.12	0.09	1	1	1
415	66	63	0.14	0.13	1	1	1
416	109	83	0.24	0.17	1	1	1
417	122	0	0.35	0	1	0	1
418	806	72	0.52	0.05	1	1	1
419	0	0	0	0	0	0	0
420	1009	460	0.47	0.22	1	1	1
421	0	0	0	0	0	0	1
422	0	0	0	0	0	0	0
423	161	47	0.74	0.19	1	1	1
424	419	253	0.44	0.25	1	1	1
425	0	0	0	0	0	0	0
426	1027	796	0.92	0.73	1	1	1
427	299	214	0.59	0.41	1	1	1
428	11	2	0.02	0	1	0	0
429	149	0	0.32	0	1	0	0
430	2	0	0	0	0	0	0
431	105	0	0.23	0	1	0	0
432	14	0	0.03	0	1	0	0
433	243	166	0.44	0.2	1	1	1
434	21	0	0.03	0	1	0	0
435	149	149	0.18	0.18	1	1	1
436	200	189	0.2	0.19	1	1	1
437	0	0	0	0	0	0	0
438	160	114	0.14	0.1	1	1	1
439	223	198	0.29	0.24	1	1	1
440	192	169	0.17	0.15	1	1	1
441	464	399	0.55	0.42	1	1	1
442	341	270	0.38	0.29	1	1	1
443	203	150	0.15	0.12	1	1	1

Continued on next page...

Table G.1 – continued from previous page

Object ID	Planned Points	Recog. Points	Planned Surface (m^2)	Recog. Surface (m^2)	Planned	Recog.	Actual
444	539	508	0.58	0.55	1	1	1
445	552	498	0.51	0.43	1	1	1
446	323	255	0.2	0.17	1	1	1
447	729	31	0.61	0.02	1	1	0
448	713	39	0.57	0.03	1	1	0
449	471	0	0.24	0	1	0	0
450	186	155	0.09	0.07	1	1	1
451	617	346	0.48	0.23	1	1	1
452	522	344	0.22	0.16	1	1	1
453	1353	760	0.6	0.29	1	1	1
454	1293	729	0.61	0.3	1	1	1
455	949	839	0.29	0.29	1	1	1
456	2050	1454	0.63	0.43	1	1	1
457	1840	1629	0.61	0.55	1	1	1
458	946	857	0.22	0.22	1	1	1
459	2914	2425	0.62	0.56	1	1	1
460	1463	1269	0.5	0.47	1	1	1
461	1175	998	0.43	0.39	1	1	1
462	168	120	0.34	0.25	1	1	1
463	14	0	0.03	0	1	0	0
464	0	0	0	0	0	0	0
465	107	0	0.19	0	1	0	0
466	196	0	0.4	0	1	0	0
467	138	0	0.55	0	1	0	0
468	0	0	0	0	0	0	0
469	13	0	0.04	0	1	0	0
470	175	0	0.49	0	1	0	0
471	135	0	0.51	0	1	0	0
472	1	0	0	0	0	0	0
473	52	0	0.31	0	1	0	0
474	147	0	0.46	0	1	0	0
475	184	0	0.29	0	1	0	0
476	203	0	0.4	0	1	0	0
477	90	0	0.18	0	1	0	0
478	145	0	0.29	0	1	0	0
479	14	0	0.03	0	1	0	0
480	8	0	0.02	0	1	0	0
481	3	0	0.02	0	1	0	0
482	2	0	0	0	0	0	0
483	3	0	0.01	0	1	0	0
484	16	0	0.03	0	1	0	0
485	28	0	0.05	0	1	0	0
486	13	0	0.02	0	1	0	0
487	16	0	0.03	0	1	0	0
488	252	0	0.4	0	1	0	0
489	233	0	0.39	0	1	0	0
490	2	0	0.01	0	0	0	0
491	7	0	0.02	0	1	0	0
492	44	0	0.36	0	1	0	0
493	86	0	0.58	0	1	0	0
494	22	0	0.04	0	1	0	0
495	14	0	0.02	0	1	0	0
496	2	0	0	0	0	0	0
497	5	0	0.03	0	1	0	0
498	13	0	0.02	0	1	0	0
499	15	0	0.03	0	1	0	0
500	35	0	0.06	0	1	0	0

Continued on next page...

Table G.1 – continued from previous page

Object ID	Planned Points	Recog. Points	Planned Surface (m^2)	Recog. Surface (m^2)	Planned	Recog.	Actual
501	15	0	0.02	0	1	0	0
502	7	0	0.03	0	1	0	0
503	3	0	0.01	0	0	0	0
504	11	0	0.02	0	1	0	0
505	20	0	0.03	0	1	0	0
506	0	0	0	0	0	0	0
507	0	0	0	0	0	0	0
508	0	0	0	0	0	0	0
509	4	0	0.01	0	1	0	0
510	0	0	0	0	0	0	0
511	0	0	0	0	0	0	0
512	19	0	0.04	0	1	0	0
513	29	0	0.06	0	1	0	0
514	21	0	0.08	0	1	0	0
515	20	0	0.07	0	1	0	0
516	5	0	0.01	0	0	0	0
517	34	0	0.06	0	1	0	0
518	21	0	0.03	0	1	0	0
519	0	0	0	0	0	0	0
520	11	0	0.03	0	1	0	0
521	0	0	0	0	0	0	0
522	0	0	0	0	0	0	0
523	32	0	0.1	0	1	0	0
524	30	0	0.11	0	1	0	0
525	0	0	0	0	0	0	0
526	0	0	0	0	0	0	0
527	14	0	0.04	0	1	0	0
528	0	0	0	0	0	0	0
529	40	0	0.06	0	1	0	0
530	22	0	0.03	0	1	0	0
531	6	0	0.01	0	1	0	0
532	0	0	0	0	0	0	0
533	0	0	0	0	0	0	0
534	0	0	0	0	0	0	0
535	49	0	0.06	0	1	0	0
536	38	0	0.05	0	1	0	0
537	174	0	0.28	0	1	0	0
538	0	0	0	0	0	0	0
539	3	0	0.01	0	0	0	0
540	0	0	0	0	0	0	0
541	0	0	0	0	0	0	0
542	5	0	0.02	0	1	0	0
543	4	0	0.02	0	1	0	0
544	1	0	0	0	0	0	0
545	2	0	0.01	0	0	0	0
546	0	0	0	0	0	0	0
547	0	0	0	0	0	0	0
548	5	0	0.01	0	0	0	0
549	4	0	0.01	0	0	0	0
550	0	0	0	0	0	0	0
551	0	0	0	0	0	0	0
552	3	0	0.01	0	0	0	0
553	0	0	0	0	0	0	0
554	0	0	0	0	0	0	0
555	2	0	0	0	0	0	0
556	6	0	0.01	0	0	0	0
557	0	0	0	0	0	0	0

Continued on next page...

Table G.1 – continued from previous page

Object ID	Planned Points	Recog. Points	Planned Surface (m^2)	Recog. Surface (m^2)	Planned	Recog.	Actual
558	3	0	0.01	0	0	0	0
559	0	0	0	0	0	0	0
560	0	0	0	0	0	0	0
561	12	0	0.07	0	1	0	0
562	6	0	0.01	0	0	0	0
563	3	0	0	0	0	0	0
564	2	0	0	0	0	0	0
565	5	0	0.01	0	0	0	0
566	0	0	0	0	0	0	0
567	0	0	0	0	0	0	0
568	2	0	0.01	0	0	0	0
569	1	0	0	0	0	0	0
570	3	0	0	0	0	0	0
571	3	0	0	0	0	0	0
572	1	0	0	0	0	0	0
573	0	0	0	0	0	0	0
574	0	0	0	0	0	0	0
575	2	0	0.01	0	1	0	0
576	1	0	0	0	0	0	0
577	32	0	0.1	0	1	0	0
578	23	0	0.04	0	1	0	0
579	0	0	0	0	0	0	0
580	9	0	0.04	0	1	0	0
581	1	0	0	0	0	0	0
582	0	0	0	0	0	0	0
583	0	0	0	0	0	0	0
584	34	0	0.26	0	1	0	0
585	10	0	0.03	0	1	0	0
586	16	0	0.06	0	1	0	0
587	0	0	0	0	0	0	0
588	0	0	0	0	0	0	0
589	0	0	0	0	0	0	0
590	0	0	0	0	0	0	0
591	0	0	0	0	0	0	0
592	3	0	0.01	0	0	0	0
593	0	0	0	0	0	0	0
594	3124	2063	1.37	0.84	1	1	1
595	2685	2274	0.99	0.84	1	1	1
596	1925	1662	0.86	0.68	1	1	1
597	3925	3857	1.43	1.41	1	1	1
598	1246	275	0.41	0.18	1	1	1
599	559	33	0.48	0.02	1	1	0
600	345	0	0.25	0	1	0	0
601	637	69	0.4	0.04	1	1	0
602	858	52	0.45	0.03	1	1	0
603	769	34	0.33	0.01	1	0	0
604	17	0	0.02	0	1	0	0
605	799	52	0.48	0.04	1	1	0
606	96	0	0.07	0	1	0	0
607	362	38	0.28	0.03	1	1	0
608	301	27	0.22	0.02	1	1	0
609	0	0	0	0	0	0	0
610	726	68	0.46	0.04	1	1	0
611	452	41	0.3	0.03	1	1	0
612	918	51	0.21	0.01	1	0	0

Appendix H

Notation

This appendix presents the mathematical notations and variables used in this thesis. They are listed Tables H.1 and H.2, respectively.

Table H.1: Mathematical notations.

Notation	Description
$\angle x$	Angle x (note: if the angle is noted with a Greek letter, the notation $\angle$ is discarded).
$x \leftarrow y$	Assignment of the value of y to x.
$x\,y$	x multiplied by y.
$\frac{x}{y}$ or x/y	x divided by y.
$\sqrt{x}$	Square root of x.
x^n	x to the power of n.
$x.y$	Property y of x.
$\{x\}$	Set of elements of type x.
$n\left(\{x\}\right)$	Cardinality of the set of elements of type x.
$(a, b, \ldots, z)$	Set of elements of different types.
$[a, b, \ldots, z]$	Coordinate vector
$[x, y, z]$	Cartesian 3D coordinates $[x, y, z] = \begin{bmatrix} x \\ y \\ z \end{bmatrix}$
$[\varphi, \theta, \rho]$	Spherical coordinates (φ:pan, θ:tilt and ρ:range) as defined in Appendix B.
$\overrightarrow{x}$	Vector x.
$\overrightarrow{x} \cdot \overrightarrow{y}$	Scalar product of vectors $\overrightarrow{x}$ and $\overrightarrow{y}$.
$\overrightarrow{x} \times \overrightarrow{y}$	Cross product of vectors $\overrightarrow{x}$ and $\overrightarrow{y}$.

Continued on next page...

Table H.1 – continued from previous page

Notation	Description
$\|\overrightarrow{x}\|$	Euclidean distance (norm) of vector $\overrightarrow{x}$.
$\|x\|$	Absolute value of x.
$\mathcal{T}_x(x)$	Translation along the x axis of amount x: $\mathcal{T}_x(x) = \begin{bmatrix} x \\ 0 \\ 0 \end{bmatrix}$
$\mathcal{T}_y(y)$	Translation along the y axis of amount y: $\mathcal{T}_y(y) = \begin{bmatrix} 0 \\ y \\ 0 \end{bmatrix}$
$\mathcal{T}_z(z)$	Translation along the z axis of amount z: $\mathcal{T}_z(z) = \begin{bmatrix} 0 \\ 0 \\ z \end{bmatrix}$
$\mathcal{R}_x(\angle x)$	Rotation around the x axis of angle $\angle x$: $\mathcal{R}_x(\angle x) = \begin{bmatrix} 1 & 0 & 0 \\ 0 & \cos(\angle x) & \sin(\angle x) \\ 0 & -\sin(\angle x) & \cos(\angle x) \end{bmatrix}$
$\mathcal{R}_y(\angle y)$	Rotation around the y axis of angle $\angle y$: $\mathcal{R}_y(\angle y) = \begin{bmatrix} \cos(\angle y) & 0 & -\sin(\angle y) \\ 0 & 1 & 0 \\ \sin(\angle y) & 0 & \cos(\angle y) \end{bmatrix}$
$\mathcal{R}_z(\angle z)$	Rotation around the z axis of angle $\angle z$: $\mathcal{R}_z(\angle z) = \begin{bmatrix} \cos(\angle z) & \sin(\angle z) & 0 \\ -\sin(\angle z) & \cos(\angle z) & 0 \\ 0 & 0 & 1 \end{bmatrix}$

Table H.2: Notations of the variables used in the algorithms.

Variable	Description
Data	Data.
Representation	A data representation.
Feature	A data feature.
Mesh	A mesh of data points.
SpinImage	A spin image as described in [64].

Continued on next page...

Table H.2 – continued from previous page

Variable	Description
$Model$	The project 3D model.
$Object$	A STL object contained in the project 3D model.
ID	A unique identifier.
$IDobj$	An identifier specifying the ID of a STL object.
$Facet$	A facet of a STL object.
$Edge$	An edge of a STL facet.
$Vertex$ (or V)	A vertex of a STL facet (or any other type of mesh).
$Scan$	The investigated as-built range point cloud.
$(Res_\varphi, Res_\theta)$	The pan and tilt resolutions of a scan.
$Frustum$	Viewing frustum of a scan, defined as the minimum spherical angular bounding volume of the scan's range points.
P_B	An as-built range point.
P_P	An as-planned range point.
$Tree$	The hierarchical tree of extents of the project 3D model (extents being here minimum spherical angular bounding volumes).
$MSABV$	A minimum spherical angular bounding volume (MSABV).
$\varphi_{min}, \varphi_{max}$	Minimum and maximum bounding pan angles of a minimum spherical angular bounding volume.
$\theta_{min}, \theta_{max}$	Minimum and maximum bounding tilt angles of a minimum spherical angular bounding volume.
$Above$	Property whether a STL entity (facet of object) is above the scanner.
$Below$	Property whether a STL entity (facet of object) is below the scanner.
$Inverted$	Property whether a STL entity (facet of object) has inverted bounding pan angles.
α	Reflection angle of an as-planned range point scanning direction with an intersected STL facet.
$(\alpha_\varphi, \alpha_\theta)$	Decomposition of the reflection angle, α, in its pan and tilt components.
$\Delta\rho$	Difference between the range of an as-planned point and its the the range of its corresponding as-built point: $(P_P.\rho - P_B.\rho)$.
$\Delta\rho_{max}$	Point recognition threshold.

Continued on next page...

Table H.2 – continued from previous page

Variable	Description
$Surf_{unit}$	Surface covered by a point at a range of $1\,m$ perpendicularly to the direction defined by the origin and the point (scanning direction).
$Surf$	Covered surface of a as-planned range point.
$Surf_R$	Covered surface of the recognized points of a STL object's as-planned range point cloud.
$Surf_{min}$	Object surface recognition threshold.
$IsFrontFacing$	Property of a STL facet specifying whether it is front-facing with respect to the scanner's location.
$IsInFrustum$	Property of a STL entity specifying whether it intersects the frustum of a scan.
$IsRecognized$	Property of a point or STL object specifying whether it is recognized in a scan.

References

[1] *ASCE Construction Research Congress (CRC)*, San Diego, CA, USA, April 5-7 2005. 150, 152

[2] *EG-ICE: 13th EG-ICE Workshop - Intelligent Computing in Engineering and Architecture*, Ascona, Switzerland, June 25-30 2006. 149, 155

[3] *ASCE Construction Research Congress (CRC) "A Global Community"*, Grand Bahama Island, The Bahamas, May 6-8 2007. 149, 155

[4] 3D Systems Inc. Stereolithography interface specification. Technical Report 50065-S01-00, 3D Systems Inc., 1989. 85

[5] P. K. Agarwal and J. Matousek. Ray shooting and parametric search. *SIAM Journal on Computing*, 22(4):794–806, 1993. 27

[6] T. Akenine-Möller, E. Haines, and N. Hoffman. *Real-Time Rendering, 2nd edition*. A.K. Peters Ltd., 2002. 31

[7] B. Akinci. Using sensor systems and standard project models to capture and model project history for building commissioning and facility management. In *Proceeding of the Facility Area Network Workshop*, University of Illinois, Urbana-Champaign, IL, USA, February 26-27 2004. 8

[8] B. Akinci, F. Boukamp, C. Gordon, D. Huber, C. Lyons, and K. Park. A formalism for utilization of sensor systems and integrated project models for active construction quality control. *Automation in Construction*, 15(2):124–138, 2006. 6, 7

[9] B. Akinci, E. Ergen, C. T. Haas, C. H. Caldas, J. Song, C.R. Wood, and J. Wadephul. Field trials of RFID technology for tracking fabricated pipe. Fiatech smart chips report, FIATECH, Austin, TX, 2004. 2

[10] B. Akinci, S. Kiziltas, E. Ergen, I. Z. Karaesmen, and F. Keceli. Modeling and analyzing the impact of technology on data capture and transfer processes at construction sites: A case study. *Journal of Construction Engineering and Management*, 132(11):1148–1157, 2006. 6

[11] J. Amanatides. Ray tracing with cones. *Computer Graphics (SIGGRAPH 04)*, 18(3):129–135, 1984. 28

[12] F. Arman and J. K. Aggarwal. Object recognition in dense range images using a CAD system as a model base. In *Proceedings of the IEEE International Conference on Robotics and Automation (ICRA)*, volume 3, pages 1858–1863, Cincinnati, OH, USA, 13-18 May 1990. 13

[13] F. Arman and J.K. Aggarwal. Model-based object recognition in dense-range images: a review. *Computing Surveys (CSUR)*, 25(1):5–43, 1993. 12, 48

[14] K. S. Arun, T. S. Huang, and S. D. Blostein. Least-squares fitting of two 3-d point sets. *IEEE Transactions on Pattern Analysis and Machine Intelligence*, 9(5):698–700, 1987. 24

[15] J. Arvo and D. Kirk. Fast ray tracing by ray classification. *Computer Graphics*, 21(4):55–64, 1987. 28

[16] U. Assarsson and T. Möller. Optimized view frustum culling algorithms for bounding boxes. *Journal of Graphics Tools*, 5:9–22, 2000. 28

[17] A. H. Behzadan and V. R. Kamat. Georeferenced registration of construction graphics in mobile outdoor augmented reality. *Journal of Computing in Civil Engineering*, 21(4):247–258, 2007. 26

[18] P. J. Besl and N. D. McKay. A method for registration of 3-D shapes. *IEEE Transactions on Pattern Analysis and Machine Intelligence*, 14(2):239–256, 1992. 13

[19] F. Bosche, J. Teizer, C. T. Haas, and C. H. Caldas. Integrating data from 3D CAD and 3D cameras for real-time modeling. In *Proceeding of the ISCCBE/ASCE Joint International Conference on Computing and Decision Making in Civil and Building Engineering*, pages 37–46, Montreal, QC, Canada, July 12-15 2006. 8

[20] F. Boukamp and B. Akinci. Automated reasoning about construction specifications to support inspection and quality control. *Automation in Construction*, 17(1):90–106, 2007. 75

[21] I. K. Brilakis and L. Soibelman. Multimodal image retrieval from construction databases and model-based systems. *Journal of Construction Engineering and Management*, 132(7):777–785, July 2006. 7, 11

[22] I. K. Brilakis and L. Soibelman. Shape-based retrieval of construction site photographs. *Journal of Computing in Civil Engineering*, 22(1):14–20, 2008. 7, 11

[23] H. Brönnimann and M. Glisse. Octrees with near optimal cost for ray-shooting. *Computational Geometry*, 34(3):182–194, 2006. 30

[24] B. A. Brucker and S. D. Nachtigall. Initiating the building information model from owner and operator criteria and requirements. In *Proceeding of the ASCE International Conference on Computing in Civil Engineering*, Cancun, Mexico, July 12-15 2005. 2

[25] R. Buick. RTK base station networks driving adoption of GPS +/- 1 inch automated steering among crop growers. Trimble Navigation Ltd., 2006. 18

[26] C. Caldas, D. Grau, and L. Soibelman. Using global positioning systems to improve materials locating processes on industrial projects. *Journal of Construction Engineering and Management*, 132(7):741–749, 2006. 2, 7, 18

[27] R. J. Campbell and P. J. Flynn. A survey of free-form object representation and recognition techniques. *Computer Vision and Image Understanding*, 81(2):166–210, 2001. 12, 13

[28] F. Caron, S. Razavi, J. Song, P. Vanheeghe, E. Duflos, C. H. Caldas, and C. T. Haas. Locating sensor nodes on construction projects. *Autonomous Robots*, 22(3):255–263, April 2007. 7

[29] P. C. Chang, A. Flatau, and S. C. Liu. Review paper: Health monitoring of civil infrastructure. *Structural Health Monitoring*, 2(3):257–267, 2003. 6

[30] G. S. Cheok and W. C. Stone. Non-intrusive scanning technology for construction management. In *Proceedings of the* 16^{th} *International Symposium on Automation and Robotics in Construction (ISARC)*, pages 645–650, Universidad Carlos III de Madrid, Madrid, Spain, September 22-24 1999. 2, 6, 7

[31] G. S. Cheok, W. C. Stone, R. R. Lipman, and C. Witzgall. LADARs for construction assessment and update. *Automation in Construction*, 9(5):463–477, 2000. 8

[32] C. S. Chua and R. Jarvis. Point signatures: A new representation for 3D object recognition. *International Journal of Computer Vision*, 25(1):63–85, 1997. 13

[33] D. Cline, K. Steele, and P. Egbert. Lightweight bounding volumes for ray tracing. *Journal of graphics tools*, 11(4):61–71, 2006. 31

[34] L. D. Cohen. Deformable surfaces and parametric models to fit and track 3D data. In *IEEE International Conference on Systems, Man, and Cybernetics*, volume 4, pages 2451–2456, Beijing, China, 14-17 October 1996. 76

[35] G. S. Coleman and J. W. Jun. Interoperability and the construction process: A white paper for building owners and project decision-makers. Technical report, American Institute of Steel Construction, Inc., 2004. 1

[36] V. A. Collins. *Evaluation and Comparison of Commercially Available Maturity Measurement Systems*. PhD thesis, Carnegie Mellon Department of Civil and Environmental Engineering, Pittsburgh, PA, USA, 2004. 2

[37] M. de Berg, D. Halperin, M. H. Overmars, J. Snoeyink, and M. J. van Kreveld. Efficient ray shooting and hidden surface removal. *Algorithmica*, 12(1):30–53, 1994. 31

[38] C. Dorai and A. K. Jain. COSMOS - a representation scheme for 3D free-form objects. *IEEE Transactions on Pattern Analysis and Machine Intelligence*, 19(10):1115–1130, 1997. 13

[39] C. Eastman. New opportunities for IT research in construction. In *Proceeding of the 13th EG-ICE Workshop - Intelligent Computing in Engineering and Architecture* [2], pages 163–174. 2

[40] C. Eastman, F. Wang, S.-J. You, and D. Yang. Deployment of an AEC industry sector product model. *Computer-Aided Design*, 37(12):1214–1228, 2005. 2

[41] M. G. Fard and F. Peña-Mora. Semi-automated visualization of construction progress monitoring. In *Proceeding of the ASCE Construction Research Congress (CRC) "A Global Community"* [3]. 2, 9

[42] H. Freeman, editor. *Machine Vision for Three-Dimensional Scenes*, chapter The free-form surface matching problem (by P. J. Besl), pages 25–71. Academic Press, 1990. 13, 15

[43] M. P. Gallaher, A. C. O'Connor, J. L. Jr. Dettbarn, and L. T. Gilday. Cost analysis of inadequate interoperability in the U.S. capital facilities industry. Technical report, National Institute of Standards and Technology (NIST), 2004. 1

[44] J. H. Jr Garrett, B. Akinci, and S. Matthews. Sensor data driven proactive management of infrastructure systems. In *Proceeding of the 13th EG-ICE Workshop - Intelligent Computing in Engineering and Architecture* [2], pages 262–284. 8

[45] A. S. Glassner, editor. *An Introduction to Ray Tracing*, chapter A Survey of Ray tracing Acceleration Techniques (by J. Arvo and D. Kirk), pages 201–262. Academic Press Ltd., 1989. 27, 29

[46] A. S. Glassner, editor. *Graphics Gems*, chapter An efficient bounding sphere (by J. Ritter), pages 301–303. Academic Press Professional, Inc., San Diego, CA, USA, 1990. 62

[47] J. Goldsmith and J. J. Salmon. Automatic creation of object hierarchies for ray tracing. *IEEE Computer Graphics and Applications*, 7(5):14–20, 1987. 30, 31

[48] J. E. Goodman and J. O'Rourke, editors. *Handbook of discrete and computational geometry*, chapter Ray shooting and lines in space (by M. Pellegrini), pages 599–614. CRC Press, Inc., Boca Raton, FL, USA, 1997. 27

[49] M. T. Goodrich. A polygonal approach to hidden-line and hidden-surface elimination. *CVGIP: Graph Models Image Process*, 54(1):1–12, 1992. 31

[50] C. Gordon and B. Akinci. Technology and process assessment of using LADAR and embedded sensing for construction quality control. In *Proceeding of the ASCE Construction Research Congress (CRC)* [1], pages 557–561. 2, 6

[51] C. Gordon, B. Akinci, and J. H. Jr. Garrett. Formalism for construction inspection planning: Requirements and process concept. *Journal of Computing in Civil Engineering*, 21(1):29–38, January/February 2007. 6, 78

[52] C. Gordon, F. Boukamp, D. Huber, E. Latimer, K. Park, and B. Akinci. Combining reality capture technologies for construction defect detection: a case study. In *Proceeding of the 9th EuropIA International Conference(EIA9): E-Activities and Intelligent Support in Design and the Built Environment*, pages 99–108, Istanbul, Turkey, October 8-10 2003. 7

[53] T. Greaves and B. Jenkins. 3D laser scanning market red hot: 2006 industry revenues $253 million, 43% growth. *SparView*, 5(7), 2007. xii, 9

[54] V. Havran and J. R. Bittner. On improving kd-trees for ray shooting. In *The 10$^{\sharp}$h International Conference in Central Europe on Computer Graphics, Visualization and Computer Vision (WSCG)*, pages 209–216, University of West Bohemia, Campus Bory, Plzen-Bory, Czech Republic, February 4-8 2002. 30

[55] M. Hebert, K. Ikeuchi, and H. Delingette. A spherical representation for recognition of free-form surfaces. *IEEE Transactions on Pattern Analysis and Machine Intelligence*, 17(7):681–690, 1995. 13

[56] P. S. Heckbert and P. Hanrahan. Beam tracing polygonal objects. *Computer Graphics*, 18(3):119–127, 1984. 28

[57] B. Hofmann-Wellenhof, H. Lichtenegger, and E. Wasle. *GNSS Global Navigation Satellite Systems: GPS, GLONASS, Galileo, and more*. Springer, 2007. 18

[58] B. K. P. Horn. Closed-form solution of absolute orientation using orthonormal matrices. *Journal of the Optical Society of America - A*, 5(7):1127–1135, 1987. 24

[59] B. K. P. Horn. Closed form solution of absolute orientation using unit quaternions. *Journal of the Optical Society of America - A*, 4(4):629–642, 1987. 24

[60] G. A. Howell. What is lean construction? In *Proceedings of the 7th Annual Conference of the International Group for Lean Construction, IGLC-7*, pages 1–10, University of California, Berkeley, CA, USA, July 26-28 1999. 1, 5

[61] T. S. Huang, S. D. Blostein, and E. A. Margerum. Least-squares estimation of motion parameters from 3-D point correspondences. In *IEEE Conference on Computer Vision and Pattern Recognition*, pages 24–26, Miami Beach, FL, USA, 1986. 24

[62] S. Ilic and P. Fua. Using Dirichlet free form deformation to fit deformable models to noisy 3-D data. *Computer Vision - ECCV 2002 (Lecture Notes in Computer Science)*, 2351:831–832, 2002. 76

[63] G. Jacobs. 3D scanning: Using multiple laser scanners on projects. *Professional Surveyor Magazine*, 28(4), 2008. 8

[64] A. E. Johnson and M. Hebert. Using spin images for efficient object recognition in cluttered 3D scenes. *IEEE Transactions on Pattern Analysis and Machine Intelligence*, 21(5):433–449, 1999. 13, 14, 15, 20, 143

[65] P.-E. Josephson, B. Larsson, and H. Li. Illustrative benchmarking rework and rework costs in Swedish construction industry. *Journal of Management in Engineering*, 18(2):76–83, April 2002. 7

[66] T. L. Kay and J. T. Kajiya. Ray tracing complex scenes. *Computer Graphics*, 20(4):269–278, 1986. 28

[67] T. Keeler, J. Fedorkiw, and S. Ghali. The spherical visibility map. *Computer-Aided Design*, 39(1):17–26, January 2007. 30, 31, 44, 64

[68] H. Kim and N. Kano. Comparison of construction photograph and VR image in construction progress. *Automation in Construction*, 17(2):137–143, 2008. 2, 7, 9

[69] S. Kim, S. Pakzad, D. Culler, J. Demmel, G. Fenves, S. Glaser, and M. Turon. Health monitoring of civil infrastructures using wireless sensor networks. In *6^{th} International Symposium on Information Processing in Sensor Networks*, pages 254–263, Cambridge, MA, USA, 25-27 April 2003. 2

[70] N. Kitsios and A. Tsakalidis. Space reduction and an extension for a hidden line elimination algorithm. *Computational Geometry*, 6:397–404, 1996. 31

[71] S. Kiziltas and B. Akinci. The need for prompt schedule update by utilizing reality capture technologies: a case study. In *Proceeding of the ASCE Construction Research Congress (CRC)* [1], pages 163–167. 7

[72] I. Knoll, A. andWald, S. G. Parker, and C. D. Hansen. Interactive isosurface ray tracing of large octree volumes. In *IEEE Symposium on Interactive Ray Tracing*, pages 115–124, Salt Lake City, UT, USA, 18-20 September 2006. 30

[73] V. Krishnamurthy and M. Levoy. Fitting smooth surfaces to dense polygon meshes. In *23^{rd} International Conference on Computer Graphics and Interactive Techniques (SIGGRAPH)*, pages 313–324, New Orleans, Louisiana, USA, 4-9 August 1996. 12

[74] S.-W. Kwon, F. Bosche, C. Kim, C. T. Haas, and K. A. Liapi. Fitting range data to primitives for rapid local 3D modeling using sparse point range clouds. *Automation in Construction*, 13(1):67–81, 2004. 75

[75] S. Lee and F. Peña-Mora. Visualisation of construction progress monitoring. In *Proceeding of the ASCE Construction Research Congress (CRC)* [1], pages 2527–2533. 2, 9

[76] Leica Geosystems. *Leica HDS6000 - Datasheet*. Leica Geosystems, 2008. 64

[77] Leica Geosystems AG. *Leica CloudWorx 3.3 for AutoCAD*. Leica Geosystems AG, 2007. 2, 9

[78] M. Lu, W. Chen, X. Shen, H.-C. Lam, and J. Liu. Positioning and tracking construction vehicles in highly dense urban areas and building construction sites. *Automation in Construction*, 16(5):647–656, 2008. 7

[79] J. P. Lynch, A. Partridge, K. H. Law, T. W. Kenny, A. S. Kiremidjian, and E. Carryer. Design of piezoresistive MEMS-based accelerometer for integration with wireless sensing unit for structural monitoring. *Journal of Aerospace Engineering*, 16(3):108–114, 2003. 2

[80] B. McCullouch. Automating field data collection in construction organizations. In *ASCE Construction Congress V*, pages 957–963, Minneapolis, MN, USA, October 5-7 1997. 1, 2

[81] A. S. Mian, M. Bennamoun, and R. Owens. Three-dimensional model-based object recognition and segmentation in cluttered scenes. *IEEE Transactions on Pattern Analysis and Machine Intelligence*, 28(10):1584–1601, 2006. 13, 14, 15, 16, 20, 60, 65

[82] A. S. Mian, M. Bennamoun, and R.A. Owens. A novel representation and feature matching algorithm for automatic pairwise registration of range images. *International Journal of Computer Vision*, 66(1):19–40, 2006. 14, 20, 60, 65

[83] K. Mulmuley. An efficient algorithm for hidden surface removal. *Computer Graphics (SIGGRAPH'89)*, 23(3):379–88, 1989. 31

[84] R. Navon. Automated project performance control of construction projects. *Automation in Construction*, 14(4):467–476, 2005. 7

[85] R. Navon. Research in automated measurement of project performance indicators. *Automation in Construction*, 16(2):176–188, 2007. 1, 2, 6, 7

[86] R. Navon and E. Goldschmidt. Monitoring labor inputs: automated-data-collection model and enabling technologies. *Automation in Construction*, 12(2):185–199, 2002. 68, 75

[87] R. Navon and R. Sacks. Assessing research issues in automated project performance. *Automation in Construction*, 16(4):474–484, 2007. 1, 2, 5, 10

[88] R. Nevatia and T. O. Binford. Description and recognition of curved objects. *Artificial Intelligence*, 8:69–76, 1977. 13

[89] P. Ning and J. Bloomenthal. An evaluation of implicit surface tilers. *Computer Graphics and Applications*, 13(6):33–41, 1993. 12

[90] M. Ohta and M. Maekawa. Ray-bound tracing for perfect and efficient anti-aliasing. *The Visual Computer: International Journal of Computer Graphic*, 6(3):125–133, 1990. 28

[91] H. S. Park, H. M. Lee, H. Adeli, and I. Lee. A new approach for health monitoring of structures: terrestrial laser scanning. *Computer-Aided Civil and Infrastructure Engineering*, 22(1):19–30, 2007. 6

[92] F. Peyret, D. Bétaille, and G. Hintzy. High-precision application of GPS in the field of real-time equipment positioning. *Automation in Construction*, 9(3):299–314, 2000. 18

[93] F. Pipitone and W. Adams. Rapid recognition of freeform objects in noisy range images using tripod operators. In *IEEE International Conference on Computer Vision and Pattern Recognition*, pages 715–716, New York, NY, USA, 15-17 June 1993. 13

[94] N. S. Raja and A. K. Jain. Recognizing geons from superquadrics fitted to range data. *Image Vision Comput.*, 10(3):179–190, 1992. 13

[95] S. N. Razavi, D. Young, H. Nasir, C. T. Haas, C. H. Caldas, P. Goodrum, and P. Murray. Field trial of automated material tracking in construction. In *CSCE Annual Conference*, Québec, QC, Canada, 10-13 June 2008. 7, 18

[96] I. D. Reid and J. M. Brady. Recognition of object classes from range data. *Artificial Intelligence Journal*, 78(1-2):289–326, 1995. 13

[97] J. Reinhardt, B. Akinci, and J. H. Jr. Garrett. Navigational models for computer supported project management tasks on construction sites. *Journal of Computing in Civil Engineering*, 18(4):281–290, 2004. 7

[98] A. Reshetov, A. Soupikov, and J. Hurley. Multi-level ray tracing algorithm. *ACM Transactions on Graphics*, 24(3):1176–1185, 2005. 28, 30

[99] C. Rizos. Network RTK research and implementation - a geodetic perspective. *Journal of Global Positioning Systems*, 1(2):144–150, 2002. 18

[100] R. Sacks, R. Navon, I. Brodetskaia, and A. Shapira. Feasibility of automated monitoring of lifting equipment in support of project control. *Journal of Construction Engineering and Management*, 131(5):604–614, 2005. 2, 7

[101] R. Sacks, R. Navon, A. Shapira, and I. Brodetsky. Monitoring construction equipment for automated project performance control. In *Proceedings of the* 19^{th} *International Symposium on Automation and Robotics in Construction (ISARC)*, pages 161–166, National Institute of Standards and Technology (NIST), Gaithersburg, MD, USA, September 23-25 2002. 68, 75

[102] K. Saidi, A. Lytle, and C. W. Stone. Report of the NIST workshop on data exchange standards at the construction job site. In *Proceedings of the* 20^{th} *International Symposium on Automation and Robotics in Construction (ISARC)*, pages 612–622, Eidhoven, The Netherlands, September 21-25 2003. 1, 2, 7

[103] I. K. Scherson and E. Caspary. Data structures and the time complexity of ray tracing. *The Visual Computer*, 3(4):201–213, 1987. 29

[104] L. M. Sheppard. Virtual building for construction projects. *Computer Graphics and Applications*, 24(1):6–12, 2004. 26

[105] M. Shinnya, T. Takahashi, and S. Naito. Principles and applications of pencil tracing. *Computer Graphics (Proceedings of ACM SIGGRAPH 87)*, 21(4):45–54, 1987. 28

[106] R. Siegwart and I. R. Nourbakhsh. *Introduction to Autonomous Mobile Robots*. The MIT Press, 2004. 17, 18

[107] O. Skrinjar. Point-based registration with known correspondence: Closed form optimal solutions and properties. *Lecture Notes in Computer Science (Biomedical Image Registration)*, 4057:315–321, 2006. 24

[108] L. Soibelman, J. Wu, C. H. Caldas, I. K. Brilakis, and K.-Y. Lin. Data analysis on complicated construction data sources: Vision, research, and recent developments. In *Proceeding of the 13th EG-ICE Workshop - Intelligent Computing in Engineering and Architecture* [2], pages 637–652. 2

[109] J. Song, C. T. Haas, and C. H. Caldas. Tracking the location of materials on construction job sites. *Journal of Construction Engineering and Management*, 132(9):911–918, 2006. 2, 7

[110] L. Song. Project progress measurement using CAD-based vision system. In *Proceeding of the ASCE Construction Research Congress (CRC) "A Global Community"* [3]. 2, 9

[111] Statistics Canada CANSIM. Bankruptcies, by industry, by province and territory - Table 177-0006, 2007. 7

[112] S. Staub-French and M. Fischer. Industrial case study of electronic design, cost and schedule integration. Technical report, Center for Integrated Facility Engineering (CIFE), Stanford University, 2001. 2

[113] S. Staub-French and A. Khanzode. 3D and 4D modeling for design and construction coordination: issues and lessons learned. *Journal of Information Technology in Construction (ITCon)*, 12:381–407, 2007. 2

[114] F. Stein and G. Medioni. Structural indexing: Efficient 3-D object recognition. *IEEE Transactions on Pattern Analysis and Machine Intelligence*, 14(2):125–145, 1992. 13

[115] M. Stevens. Overhead costing. `http://www.contractorsblog.com/archives/2006/01/dual_overhead_r.html#more`, 2006. 7

[116] N. A. Tanner, J. R. Wait, C. R. Farrar, and H. Sohn. Structural health monitoring using modular wireless sensors. *Journal of Intelligent Materials Systems and Structures*, 14(1):43–56, 2003. 2

[117] The National 3D-4D-BIM Program. *GSA Building Information Modeling Guide Series: 03 - GSA BIM Guide for 3D Imaging*. General Service Administration (GSA), May 2007. 52

[118] J.-P. Thirion. The extremal mesh and the understanding of 3D surfaces. *International Journal of Computer Vision*, 19(2):115–128, 1996. 13

[119] Trimble. *Realworks Survey 6.1 - Technical Notes*. Trimble. 2, 9

[120] S. Umeyama. Least-squares estimation of transformation parameters between two point patterns. *IEEE Transactions on Pattern Analysis and Machine Intelligence*, 13(4):376–380, 1991. 24

[121] G. Van den Bergen. Efficient collision detection of complex deformable models using AABB trees. *Journal of Graphics Tools*, 2(4):1–13, 1997. 30, 31

[122] W. H. Wah. Introduction to STL format. `http://rpdrc.ic.polyu.edu.hk/content/stl/stl_introduction.htm#specs`, 2006. xiii, 86

[123] I. Wald, P. Slusallek, C. Benthin, and M Wagner. Interactive rendering with coherent ray tracing. *Computer Graphics Forum*, 20(3):153–165, 2001. 30

[124] L.-C. Wang. Enhancing construction quality inspection and management using RFID technology. *Automation in Construction*, 17(4):467–479, 2008. 7, 68, 75

[125] H. Weghorst, G. Hooper, and D. Donald Greenberg. Improved computational methods for ray tracing. *ACM Transactions on Graphics*, 3(1):52–69, 1984. 28, 30, 31

[126] D. Zhang and M. Hebert. Harmonic shape images: a representation for 3D free-form surfaces based on energy minimization. *Lecture Notes in Computer Science (EMMCVPR'99)*, 1654:30–43, 1999. 13, 14, 20